



Università degli Studi di Napoli *Federico II*



Università di Camerino



Consiglio Nazionale
delle Ricerche

DOTTORATO DI RICERCA IN QUANTUM TECHNOLOGIES

Ciclo XXXIV

Coordinatore: prof. Francesco Tafuri

Realizing quantum protocols with an
atom-chip for quantum embedding and
reversed quantum dynamics

Settore Scientifico Disciplinare FIS/03

Dottoranda
Ivana Mastroserio

Tutore
Prof. Francesco Saverio Cataliotti

Anni 2018/2021

*To Leonardo
and my family*



C. M. Schultz

*This is the tune of our catch, played by the picture of Nobody.
[Shakespeare, "The Tempest", Act III, scene II]*

Acknowledgments

When I arrived at LENS, despite the ultra-cold temperatures reached in their laboratories, the welcome in the *Quantum Gases* group was anything but cold! I immediately felt at home when **Nicole Fabbri** welcomed me. I have been very privileged to join this group and discover such an amazing field of research. It is for this reason that I will always be grateful to my PhD coordinator Prof. **Francesco Tafuri** for giving me this opportunity.

But first and foremost I should thank my supervisor Prof. **Francesco Cataliotti**, the work presented in this thesis would not have been possible without his support and motivation. Despite his uncountable commitments, he has been always attentive and present anytime I needed his advice. I feel profoundly lucky to be trained directly from him, in the unfortunate moment when I was alone in facing the hardships of laboratory life in a completely new field. I have learned invaluable lessons from him, his passion for science and positive attitude, always on the side of students, is unique.

I would also like to thank all the people I had the privilege to work with. In particular, the projects I have carried on have been mainly performed in collaboration with Prof. **Filippo Caruso**. I am deeply thankful to him for conceiving the theory behind them and for the fruitful collaboration.

I am grateful to **Natalia Bruno** for the careful read and suggestions on this manuscript, for the many discussions and help in the preparation of the experiments I realized, but above all for the motivation and support. I am deeply grateful to **Pietro Lombardi** too, who taught me how to deal with laboratory life with his many technical advices (and laughs!). Many thanks also to **Stefano Gherardini** and his invaluable help on the understanding and preparation of our last research article as well as being a dear friend. However, I couldn't have asked for better when our new (now not so new anymore!) PhD student arrived: **Ludovica Donati**. She's the best PhD one can wish for as well as a dear friend too. I wish to deeply thank the Sr-Lab44 members at LENS: **Leonardo Salvi**, **Enlong Wang**, **Gunjan Verma** and **Joep Assendelft** for all the times you were there to help and support me with the kindness that characterizes you all. Following the

building of your experiment from (almost) scratch gave me the opportunity to see what does it mean to deal with all the difficulties of a cold-atoms experiment and make me grow fast. In particular Leonardo, I thank you for the insightful discussions and the enormous encouragement you gave me during the darkest moments. Your enthusiasm and desire to share your knowledge manifests the incredibly loving and gentle heart you have as a scientist and as a person.

During my journey I had the great fortune to cross my path with other two amazing people: **Ilaria Vagniluca** and **Maja Colautti**. You two hold a special place in my heart and my experience here in Florence wouldn't have been the same without you. I hope our friendship will continue as it is now.

I also wish to thank many other friends that I have met here and that in these three years shared with me uncountable lunches and coffee breaks, funny moments and laughs. They are: Valentin Gebhart, Elham Faraji, Giovanni Gangale, Paolo Vezio, Jonathan Tinsley, Nicola Biagi, Nicola Dalla Pozza, Tecla Gabbrielli, Giuseppe Vinelli, Nicola Salvi, Riccardo Tani.

Special thanks goes to **Guido Celentano**, an indispensable help in deciphering the complicated PhD bureaucratic steps. His support and cheering can be felt from afar, making me miss the family atmosphere typical of the Neapolitan Physics' department.

Among all I reserve a special place for friends and family who have always been there for a long time. To my parents *Margherita* and *Paolo* and my beautiful sister *Giuliana*, being away from home made me realize even more how important you are to me and how much we have shared till now. It's hard to quantify how lucky I feel to have you in my life. In this regard I owe a lot to my Florentine family who immediately made me feel at home and partially filled your lack: *Paola*, *Margherita*, *Sergio*, *Paola*, *Nicola* and *Edoardo*. All of you are amazing and inspiring people and you make me feel even more fortunate.

It is hard to list my numerous cousins and relatives both from mom's and dad's side, also known as "*parenti serpenti*", that paradoxically the pandemic has made closer even if far away. I love you all!

Instead, they are a few but the best, my dearest friends *Alessandro*, *Rossella* and *Antonella*. I thank you because you are as you are: sincere and unique people, the ones I know that I will always bring with me wherever the future decides to relocate us.

Again I want to thank you, *Leonardo*, not only because you are the best scientist, electrician, travel companion, pianist and lyrical singer under the shower, walker of the night, cat, Fox Mulder, thriller/noir movies addict, but because most of all you chose to be my *companion in life* and this makes me the happiest person.

Abstract

A *quantum protocol* is a set of rules or procedures, that exploit Quantum Mechanics, to realize a specific task. In this thesis, I explore two different quantum protocols realized by the coherent manipulation of the internal dynamics of a Bose-Einstein condensate (BEC) of ^{87}Rb produced on an atom-chip.

In the first quantum protocol I experimentally investigate the possibility to successfully implement quantum embedding of a large amount of classical data, to be classified, into the evolution parameters of the BEC quantum state. A quantum embedding is, indeed, the mapping of a set of data input into new data clusters in a larger Hilbert space where their subsequent classification can be more feasible by well-trained artificial neural networks. The high degree of control and isolation of the atomic system from the external environment makes it the ideal candidate, among the other explored platforms, for implementing such algorithms, as further confirmed by the high fidelities achieved exceeding 97%. The potential advantages of representing classical data on quantum systems include not only the possibility to simplify a classification problem as experimentally demonstrated in this work, but also the ability to speed up any processing of classical data, such as quantum parallelism to search through a database exploitation, feature extraction, image segmentation and edge detection.

The second quantum protocol I report concerns the experimental realization of a time-inversion evolution of our BEC dynamics. In the context of gate-based quantum computers applications, this procedure allows one to time-reverse the last performed operation on a quantum computer so as to perfectly restore a condition in which an arbitrary new operation can be realized. In this regard, our work explores several time-reversal experiments letting the BEC evolve through different paths in the Hilbert space. I detail how the optimal backward evolution is achieved by means of a radio-frequency pulse modulation designed with a dressed Chopped Random Basis (dCRAB) algorithm. I show how this technique successfully works in bringing the system back to its initial conditions with an average accuracy of 92%. Furthermore, I demonstrate how the proposed procedure can be interpreted, from a thermodynamic point of view, as an entropy rectification method. The final results can be applied for the practical realization

of a quantum *undo* operation encoded in a sub-part of a quantum processor. The *undo* command is indeed a logical operation reverse, which in some platforms, like the gate-based one presented in this thesis, can be related to the time-reversal of the last performed operation. All the presented experiments of time-inversion constitute the proof-of-principle of a wide class of quantum *undo* operations to be implemented in several quantum technology contexts.

Contents

Acknowledgments	i
Abstract	iii
Contents	v
Introduction	1
1 Cooling and trapping neutral atoms	5
1.1 Cooling neutral atoms	6
1.1.1 Scattering force	6
1.1.2 Optical Molasses	8
1.1.3 Doppler cooling limit	11
1.1.4 Below the Doppler cooling limit	13
1.2 Trapping neutral atoms	14
1.2.1 Interaction with a static magnetic field	15
1.2.2 Magnetic trapping	18
1.2.3 Magneto-Optical Trap	18
1.2.4 Quadrupole and Ioffe-Pritchard traps	22
1.3 Bose-Einstein condensation	24
1.3.1 Evaporative cooling	26
1.3.2 Coherence of a Bose-Einstein condensate	28
2 Experimental apparatus: a BEC on an atom-chip	29
2.1 Cooling and trapping on an atom-chip	30
2.1.1 Wire traps principles	31
2.1.2 Quadrupole U-trap	33
2.1.3 Ioffe-Pritchard Z-trap	34
2.2 The experimental setup	35
2.2.1 The atom-chip layout	35
2.2.2 Apparatus and Mirror-MOT	38

2.2.3	Laser system	41
2.2.4	Steps towards BEC on the atom-chip	44
2.2.5	Imaging system	49
2.3	Manipulating the BEC internal states	51
2.3.1	Microwave manipulation	51
2.3.2	Radio-Frequency manipulation	52
3	State manipulation and control for Quantum Machine Learning	55
3.1	Types of learning algorithms	57
3.2	Quantum embedding kernels	58
3.3	Training Quantum Embedding	62
3.4	Theoretical background for the atomic platform	65
3.4.1	The Bloch sphere representation	66
3.4.2	Unitary evolution on the Bloch sphere	67
3.4.3	Rotations around x-axis: controlled evolution	71
3.4.4	Rotations around z-axis: free evolution	72
3.4.5	Ramsey sequence	73
3.5	Experimental implementation on the atomic platform	76
3.5.1	Experimental limits of the atomic platform	82
3.5.2	Rotations around non-orthogonal axes	85
3.6	Superconducting and photonic platforms results	87
3.7	Discussion & conclusions	90
4	Reversing time with ultra-cold atoms for quantum <i>undo</i> operations	93
4.1	<i>Undo</i> operations on a quantum computer	95
4.2	Physical system and optimization protocol	97
4.2.1	Radio-frequency modulation with dCRAB	99
4.3	Time reversal experiments	102
4.3.1	First set of experiments	103
4.3.2	Second set of experiments	105
4.3.3	Third set of experiments	109
4.4	Discussion & conclusions	110
	Final remarks	112
	Appendices	115
A	Rubidium 87	116
B	C-SWAP Test	118

List of abbreviations	120
List of figures	123
List of tables	124
Bibliography	125

Introduction

On August 12th 1981, what would become the most popular computer design standard in the world was released on the market: the first IBM Personal Computer, also known as the “*IBM PC*”. During those years, the availability of more and more powerful computers has revolutionized many areas of science, inevitably affecting also the field of quantum physics. But it was more surprising to discover that the revolution could also go in the opposite direction, i.e. that the fields of information and computation may benefit from quantum physics in a new and profound way [1, 2]. Indeed, a few months earlier in that same year, 1981, the idea of Quantum Computing was already coming to life from a keynote speech by Richard Feynman about *Simulating Physics with Computers* [3]. He pointed out that the best way to simulate a real-world scenario governed by quantum-mechanical laws, like chemical reactions or semiconductor’s properties, was with a machine that itself follows quantum-mechanical rules. This deduction could be seen as stemming from observing that information itself has a physical nature and hence it is “*inevitably tied to a physical representation*” [4]. As a consequence, also the laws of information transmission are subject to the same natural laws of physics, in particular those of quantum physics.

A quantum computer represents a fundamental departure from the current way we process information in classical computers. It is based on quantum bits, “*qubits*”, which are the quantum information carriers. They allow the storage and processing of quantum mechanically coherent superpositions of data bits. In this context, the algorithms necessary to implement a typical computation on a quantum computer have to be regarded as a set of physical operations, which is actually true also for a classical computer, whereas its registers are made by states of a quantum system. The data initialization, for a program to run, is realized by the preparation of an initial quantum state and the program itself is carried out by the appropriate time evolution operators that realize the desired output state. The readout of the latter will consequently be a quantum measurement, thus probabilistic. The algorithms designed to run on a quantum computer can perform computational tasks that are impractical on conventional machines. Indeed, such a computer would benefit from the many advantages coming from

Quantum Mechanics laws. For instance, it would aim to make a virtue of the correlations arising from the phenomenon of *entanglement*, unique to quantum systems. The latter is an essential feature that makes the information carried by a quantum computer completely different from the one processed by ordinary digital computers. In quantum networks, for instance, entanglement is a key resource in transmitting data between different nodes by taking advantage of the correlations shared by different particles at different locations. Furthermore its investigation can benefit quantum complexity and quantum error correction [83]. In this new light, computation in the realm of Quantum Mechanics can be exponentially faster than its classical counterpart, for certain algorithms. To build a quantum computer multiple platforms are being explored, from superconducting and photonic circuits to topological systems and trapped ions. Many of these approaches are backed by companies such as IBM¹, Google², Microsoft³, Honeywell⁴. Ultra-cold neutral atoms, that offer the possibility to work from thousands to tens of millions of fermionic or bosonic particles, can be the newest kind of quantum computing modalities, owing to their greatest ultimate promise for scalability. Indeed, a great advantage of qubits based on atoms is that the cooling and trapping potentials, used to confine them, can collect million of qubits in a volume that is millimeters on a side, thus providing a reduced overall size of the quantum computer core. Moreover, the dimensions of a single atom are much smaller than the ones of qubits created via superconducting experiments, in addition to the fact that they do not have manufacturing defects. Sources like lasers and radio-frequency or microwave pulses can be used to arrange them in a way to create the gates. Furthermore, laser cooling and trapping techniques allow to reach sub-microkelvin temperatures without the need of large dilution refrigerators using liquid helium as in superconductive platforms. The extremely fragile atomic qubits are thus kept cold and isolated by ultra-high-vacuum cells protecting them from noise and decoherence.

A scalable cold atom based quantum computing hardware and software platform is already advancing. A 100-qubit computer of this kind, for instance, will be soon delivered and available on a cloud service in 2022 named Hilbert realized by the ColdQuanta company in Boulder, Colorado⁵. Thinking about what the quantum computing companies are trying to do, it will be just a matter of time, expertise and, of course, capital to get from here to a practical scalable quantum computer. The work I present here, divided into two separate quantum protocols, develops around the *control engineering* level of the quantum computer stack [5]. I report

¹<https://www.ibm.com/quantum-computing/>

²<https://quantumai.google/>

³<https://azure.microsoft.com/it-it/solutions/quantum-computing/>

⁴<https://www.honeywell.com/us/en/company/quantum/quantum-computer>

⁵<https://coldquanta.com/>

different experimental implementations of high degree of control on the evolution of a single qubit performed by a Bose-Einstein condensate (BEC) made of approximately 10^5 atoms of ^{87}Rb , realized in our laboratory with an atom-chip. The latter is a very promising platform possessing several properties that a realistic quantum processor should have. For instance scalability, optimal control on the coherent evolution of qubits and the integrability of cold atoms with nanostructures which guarantee an higher degree of coupling between the system and the manipulation fields.

The first quantum protocol I describe is an extensive experimental study of Quantum Embedding which develops in the context of classification algorithms for Quantum Metric Learning used in Machine Learning. It consists in an algorithm that maps a large amount of complex classical data into a larger Hilbert space in which the classification can be easily performed via a linear quantum classifier. The embedding protocol is subsequently tested on three different experimental platforms by tailoring it to ultra-cold atoms, photonics and via-cloud available NISQ computers. In this regard, I will be mainly concerned in the atomic experiment I carried out. Starting from a single prescription, that is the same for each platform, the aim of this work is demonstrating the success of quantum embedding protocols at different experimental levels, exploring how different sources of noise and imperfections impact their realization.

The second quantum protocol I report, concerns the proposal of an entropy rectification method that makes use of optimal control strategies [129] to carry out time-reversal transformations in our Bose-Einstein condensate. The dynamical evolution of the BEC's quantum state is driven forth and back in time through several paths in the Hilbert space. The driving field is an optimally designed radio-frequency pulse with amplitude modulated according to the dCRAB algorithm [122–126]. The versatility of the algorithm makes it possible to implement it in a generic experimental platform. All the proposed time-reversal experiments can be seen as the proof-of-principle of a wide class of *undo* operations to be implemented in the next future in several quantum technology contexts, ranging from quantum computing to quantum communications.

Thesis outline.

This thesis is organized and presented as follows.

- In chapter 1, I review the basic concepts of laser cooling and magnetic trapping of neutral atoms. These techniques are fundamental in reaching the desired spatial compression and temperature reduction to a consequent increase in the phase-space density that leads to quantum degeneracy and thus to Bose-Einstein condensation. Concluding the chapter, I detail the evaporative cooling technique that most BEC experiments exploit in their

final stage.

- In chapter 2, I show how the techniques, presented in the previous chapter, can be applied in the context of microtraps realized with atom-chips. I subsequently provide a description of the architecture and the typical experimental sequence that we adopt for the realization of a BEC on our atom-chip-based apparatus. Finally I dedicate a first analysis on how I experimentally manipulate the BEC focusing on the necessary control fields. A more detailed description for each control field will be provided in the next chapters in the context of their specific use.
- In chapter 3, I provide a first overview of the typical Machine Learning algorithms to describe the framework for the quantum embedding protocol, proposed in this work. The latter falls in the category of classification algorithms, thus I will describe the Quantum Embedding Kernels on which the training of our algorithm is based. In this chapter I also develop the theory necessary to understand the experimental implementation of such algorithm on the atomic platform. I then report and comment on the atomic experimental findings together with the ones achieved on the superconductive and photonic platforms.
- In chapter 4, I report the time-reversal experiments realized with our BEC to be intended as an operation of quantum *undo* on a quantum computer. After an introduction on the *undo* operations on quantum computers, I present the quantum system Hamiltonian and the proposed optimization protocol used to time-reverse the BEC dynamics. I will then detail how the driving field is optimally prepared by means of the dCRAB algorithm. The three sets of experiments realized to test the protocol are subsequently presented with their results. I conclude the chapter providing a thermodynamic interpretation of the experimental findings.
- Final remarks conclude the thesis.

1 | Cooling and trapping neutral atoms

The quantum protocols presented in this thesis work share a common atomic platform represented by a Bose-Einstein condensate made of ^{87}Rb atoms. In this chapter, following the history of laser cooling and trapping, I evidence how the combination and the development of these two techniques led to the achievement of sufficiently low temperatures and high densities of an atomic gas to collapse in a Bose-Einstein condensate, a state of matter that can be described by a single quantum state in which the atoms that constitute it behave as a unique macroscopic matter wave. In these conditions, the quantum nature of atomic wavefunction becomes observable and can be investigated.

Following the guideline that can be found in numerous textbooks [6, 7], I report the fundamental concepts behind these techniques. In Sec. 1.1 I describe how the mechanical effect of light, due to the transfer of momentum when an atom absorbs a photon (Subsec. 1.1.1), slows down the atomic motion. In a particular arrangement of laser beams and combined with the physical principle of Doppler effect, I detail in Subsec. 1.1.2 the use of such optical forces to cool an atomic cloud in three dimensions: the optical molasses. In Subsec. 1.1.3 I report the limitations of this technique and in Subsec. 1.1.4 I explain how understanding the reasons for the strong disagreement between the Doppler theory and experimental evidence opened the door to the overcoming of such limits and the experimental realization of new sub-Doppler laser cooling techniques. In Sec. 1.2 the working principles of magnetic trapping are explained, starting from the foundations of the interaction of an atom with a static magnetic field (Subsec. 1.2.1). A description of the first magnetic traps is given in Subsec. 1.2.4, according to which the Magneto-Optical Trap technique was developed subsequently (Subsec. 1.2.3). The cooling and trapping mechanisms are fundamental tools to reach the desired spatial compression and consequent increase in phase-space density required for the phase transition into a Bose-Einstein condensate described in Sec. 1.3. These stages are, indeed, necessary in providing the optimal conditions for the final evaporation stage explained in Subsec. 1.3.1, to cool the atoms to

quantum degeneracy and condense.

1.1 Cooling neutral atoms

In 1871, in his *Theory of Heat* [8], Maxwell explained in clear and simple words the common experience that we have with the idea of temperature. “*The distinction between hot bodies and cold ones is familiar to all, and is associated in our minds with the difference of the sensations which we experience in touching various substances, according as they are hot or cold*”. Indeed, the thermodynamic definition of temperature of a system requires thermal contact between the system and its surrounding environment. Not only, according to the “zeroth law” of thermodynamics, the system has to be in thermal equilibrium with it.

However, this is not the case when dealing with an isolated atomic ensemble. Despite it may be in a very well identified steady state, a sample of atoms is not necessarily in thermal equilibrium. In laser cooling experiments, indeed, atoms interact with light and constantly absorb and scatter it. Moreover, even though light is a form of energy, it cannot be considered as heat and definitely there is no heat exchange. Therefore, to describe the temperature of a one-dimensional atomic ensemble that has a Maxwell-Boltzmann velocity distribution, it is more convenient to use an average kinetic energy $\langle E_k \rangle$ which relates to temperature as $\langle E_k \rangle = k_B T / 2$, k_B being Boltzmann’s constant.

The exchange of momentum between atoms and an optical field, nearly resonant with an atomic frequency, is the foundation on which the idea of laser cooling has been built. The force resulting from this momentum exchange, the *scattering force*, is well known and has been quantitatively explained by Maxwell’s theory of electromagnetism. But only later on, in 1975, in Ref. [9] Hänsch and Schawlow [10], and then in the same year Wineland and Dehmelt [11], proposed, in independent papers, the idea of exploiting the mechanical effects of light to damp the atomic motion. Effects that have been for the first time experimentally demonstrated a few years later in 1978 [12, 13].

1.1.1 Scattering force

Consider the Heisenberg equation of motion for a two level system represented by a 2×2 hermitian density matrix ρ , whose diagonal real terms ρ_{gg} and ρ_{ee} represent the populations of the ground and excited states respectively, while the off-line complex terms $\rho_{ge} = \rho_{eg}^*$ are related to the phase coherence of the system wave functions. Solving it for an atom plus laser light, taking into account the spontaneous decay rate Γ , one obtains the *Maxwell-Bloch equations* also called

optical Bloch equations (OBE):

$$\begin{aligned}
\frac{d\rho_{gg}}{dt} &= +\Gamma\rho_{ee} + \frac{i}{2} (\Omega^* \tilde{\rho}_{eg} - \Omega \tilde{\rho}_{ge}), \\
\frac{d\rho_{ee}}{dt} &= -\Gamma\rho_{ee} + \frac{i}{2} (\Omega \tilde{\rho}_{ge} - \Omega^* \tilde{\rho}_{eg}), \\
\frac{d\tilde{\rho}_{ge}}{dt} &= -\left(\frac{\Gamma}{2} + i\Delta\right) \tilde{\rho}_{ge} + \frac{i}{2} \Omega^* (\rho_{ee} - \rho_{gg}), \\
\frac{d\tilde{\rho}_{eg}}{dt} &= -\left(\frac{\Gamma}{2} - i\Delta\right) \tilde{\rho}_{eg} + \frac{i}{2} \Omega (\rho_{gg} - \rho_{ee}),
\end{aligned} \tag{1.1}$$

where $\Delta = \omega - \omega_0$ is the laser detuning from the atomic resonance ω_0 and we define $\tilde{\rho}_{eg} \equiv \rho_{eg} e^{-i\Delta t}$ and $\tilde{\rho}_{ge} \equiv \rho_{ge} e^{i\Delta t}$ for the coherences. The Rabi frequency Ω , that represents the strength of the coupling between the light and the atomic transition, is defined as:

$$\Omega = \frac{\mathbf{d}_{ge} \cdot \mathbf{E}_0}{\hbar}, \tag{1.2}$$

where \mathbf{d}_{ge} is the electric dipole moment for the $g \rightarrow e$ transition and $\mathbf{E}_0 = \hat{e}E_0$ is the vector electric field amplitude.

If the laser light interacts with the atoms for a period longer compared to the natural life-time of the excited state $\tau = 1/\Gamma$, we can solve equations (1.1) in steady state conditions and get the probability of the excited state to be:

$$\rho_{ee} = \frac{s/2}{1 + s + \frac{4\Delta^2}{\Gamma^2}}, \tag{1.3}$$

where $s = 2|\Omega|^2/\Gamma^2$ is the saturation parameter.

In terms of this solution we can now write the total photon scattering rate that is the number of scattered photons per second $\Gamma_{scatt} = \Gamma\rho_{ee}$. Therefore, the scattering force, resulting from the momentum exchange between light and atoms, equals the rate at which each absorbed photon transfers momentum to the atoms $\mathbf{F}_{scatt} = d\mathbf{p}/dt = \hbar\mathbf{k}\Gamma_{scatt}$. So that:

$$\mathbf{F}_{scatt} = \hbar\mathbf{k} \frac{\Gamma}{2} \frac{I/I_{sat}}{1 + \frac{I}{I_{sat}} + \frac{4\Delta^2}{\Gamma^2}}, \tag{1.4}$$

note that the Rabi frequency and saturation intensity I_{sat} are related by $I/I_{sat} = 2|\Omega|^2/\Gamma^2$ and this is another way of expressing the saturation parameter s . Therefore, when the laser intensity I is high compared to the saturation intensity I_{sat} ($I \gg I_{sat}$) the spontaneous emission rate tends to $\Gamma/2$ and the maximum value of the scattering force to $\mathbf{F}_{scatt}^{max} = \hbar\mathbf{k}\Gamma/2$. In these conditions the maximum acceleration imparted to an atom of mass M is $\mathbf{a}_{max} = \mathbf{F}_{scatt}^{max}/M = \mathbf{v}_r/2\tau$, where $\mathbf{v}_r = \hbar\mathbf{k}/M$

is the recoil velocity. To get a quantitative idea, for a rubidium atom (see Appendix A) $v_r = 5.88 \text{ mm s}^{-1}$ and $a_{max} = 1.1 \times 10^5 \text{ m s}^{-2}$, approximately 10^4 times the gravitational acceleration. Moreover, for an atom moving towards the laser with constant deceleration, we can derive its stopping distance as $L_0 = v_0^2/a_{max}$, where v_0 is the initial velocity of the atoms. This treatment, valid for a single atom, can be extended to many non-interacting atoms that have the following Maxwell-Boltzmann velocity distribution function:

$$f(\mathbf{v}) \propto e^{-\frac{m|\mathbf{v}|^2}{2k_B T}}. \quad (1.5)$$

In this estimation we assumed the simplified vision of a constant atomic deceleration, but what happens really is that, because of the Doppler effect, only a fraction of atoms with a velocity in the interval Δv perceive the damping force, all the others sense the force as weak and won't be decelerated. It is worth noting, in fact, that the scattering force is a Lorentzian of the type $\propto [(1+s)(1+4\Delta^2/(1+s)\Gamma^2)]^{-1}$ with full width at half maximum $\Delta\omega \simeq \Gamma\sqrt{1+s}$. Being $\Delta\omega = \mathbf{k} \cdot \Delta\mathbf{v}$, we have $\Delta\mathbf{v} \simeq \Gamma/\mathbf{k}$ that for rubidium and a laser resonant with its D2-line is 4.68 m s^{-1} . This result clearly shows that the atoms which experience a strong force belongs to a very narrow interval of velocities around v_0 . Moreover, the small class of atoms that strongly interacts with the scattering force produced by the laser, will be decelerated until their Doppler-shift will bring them out of resonance. In order to maintain the scattering force around its maximum value, it is indeed necessary to compensate the velocity change during the slowing process.

1.1.2 Optical Molasses

The force described in the previous section is the foundation on which the cooling principle of neutral alkali atoms has been built. However, during the slowing process the change in the atoms Doppler-shift is an obstacle hence bringing their frequency out of resonance with the laser and therefore no more decelerated. In this section we will show how a combination of radiation pressure forces produced by three pairs of orthogonal standing waves, coming from the same laser and therefore at the same frequency, can lead to a viscous force on a gas of atoms that overcomes the Doppler-shift problem and even takes advantage of it (Fig. 1.1 a). This technique, indeed, takes the name of *Doppler-molasses* or *Optical Molasses* (OM), because of its viscous nature. The first experimental observation of an OM has been realized by the Bell Labs team [14], led by Steven Chu in 1985. To see the effects of the atom velocity in the Eq. (1.4) of the scattering force, we have to include the Doppler effect in the laser frequency ω seen by an atom moving at velocity \mathbf{v} . The shift on the laser frequency is $\omega' = \omega - \mathbf{k} \cdot \mathbf{v}$

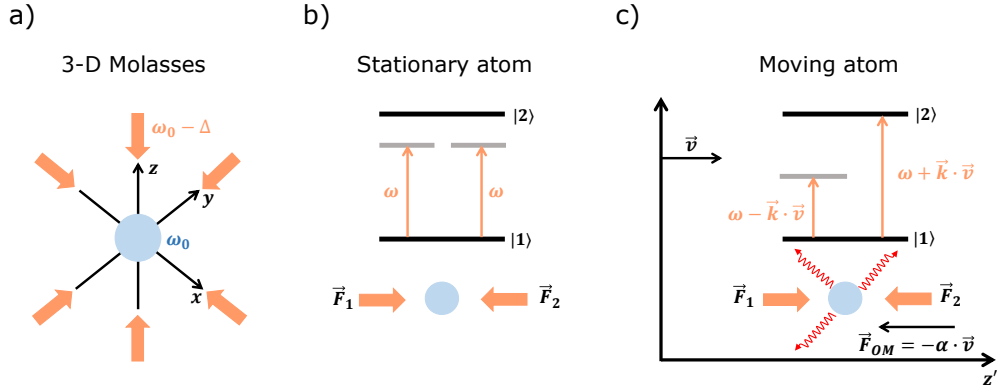


Figure 1.1: *Doppler cooling*. a) Three pairs of counter-propagating orthogonal beams with the same frequency affect an atomic sample as an *Optical Molasses*. b) A stationary atom in two counter-propagating beams with the same frequency slightly detuned below its atomic resonance, experiences zero scattering force. c) For a moving atom, the Doppler-shift brings the light frequency closer to resonance such that the atom experiences the scattering force only coming from the beam propagating opposite to its velocity direction. Image adapted from Ref. [7].

(note that \mathbf{k} , in the opposite direction respect to \mathbf{v} , produces a positive Doppler shift for the atoms). As a consequence, the detuning from resonance becomes $\Delta' = \Delta - \mathbf{k} \cdot \mathbf{v}$ and the scattering force dependent on the atom velocity:

$$\mathbf{F}_{scatt}(\mathbf{v}) = \hbar \mathbf{k} \frac{\Gamma}{2} \frac{I/I_{sat}}{1 + \frac{I}{I_{sat}} + \frac{4(\Delta - \mathbf{k} \cdot \mathbf{v})^2}{\Gamma^2}}. \quad (1.6)$$

For simplicity, we restrict to the one-dimensional problem in which we have $\mathbf{k} \cdot \mathbf{v} = kv$, where lasers propagate along the same direction as the atom. The slowing lasers are just two orthogonal counter-propagating beams with the same frequency ω slightly below the transition frequency of the two atomic levels $|1\rangle$ and $|2\rangle$, as depicted in Fig. 1.1 b and 1.1 c. In the case of a stationary atom (Fig. 1.1 b), the force resulting from the two counter-propagating beams is zero since they balance each other. For a moving atom, instead, (Fig. 1.1 c) the Doppler shift coming from the atom that moves towards one beam and against the other, generates an imbalance in the force that damps the atomic motion. In particular, if the atom moves opposite the direction of the light propagation, the Doppler-shift will lead to more scattering with respect to the other beam. Indeed, the laser frequency, seen from the atom moving towards it, is closer to resonance, while the frequency, seen from the atom moving against the laser, is far. The resultant force can be mathematically expressed as the difference between the force F_1 , directed as the atom's velocity, and F_2 , opposite to the atom's velocity,

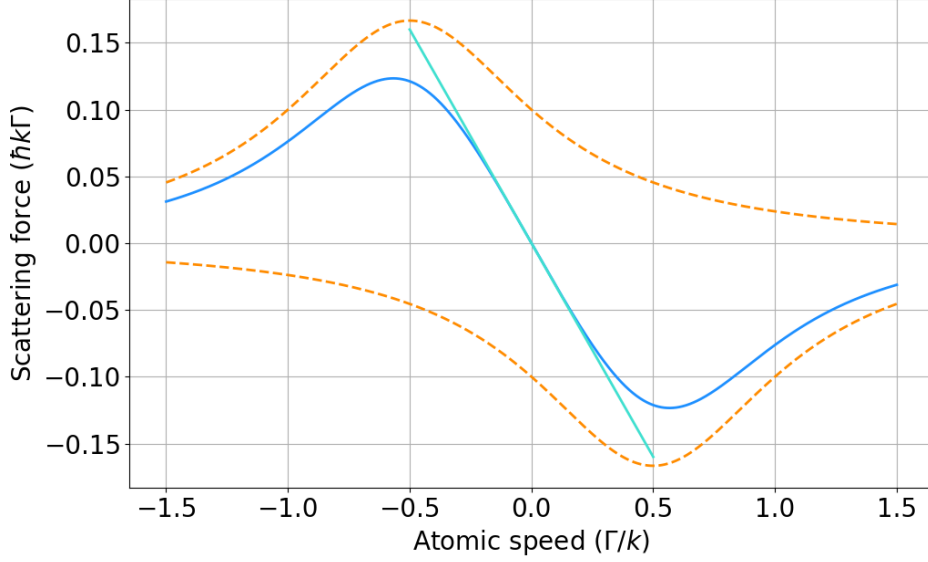


Figure 1.2: *The force in the Optical Molasses technique.* Velocity dependence of the uni-dimensional OM damping force for $\Delta = -\Gamma/2$ and $I = I_{sat}/2$. The solid blue curve represents the total effect of the two counter-propagating beams exerting two opposite radiative forces F_1 and F_2 on the atomic sample. The dotted orange curves, instead, represent each the two forces separately. The straight light-blue line shows the pure damping effect of the OM force over a restricted velocity range that is the velocity capture range (approximately Γ/k).

as follows:

$$F_{OM}(v) = F_1 - F_2 = \hbar k \frac{\Gamma}{2} \left(\frac{I/I_{sat}}{1 + (I/I_{sat}) + \frac{4(\Delta - kv)^2}{\Gamma^2}} - \frac{I/I_{sat}}{1 + (I/I_{sat}) + \frac{4(\Delta + kv)^2}{\Gamma^2}} \right). \quad (1.7)$$

For small velocities $|kv| \ll \Gamma$ we can use the first order approximation $1/(1-x) \simeq (1+x)$ where in our case $x = \frac{8\Delta kv/\Gamma^2}{1+(I/I_{sat})+(4\Delta^2/\Gamma^2)}$ and get:

$$F_{OM}(v) = 4\hbar k^2 \frac{I}{I_{sat}} \frac{2\Delta/\Gamma}{[1 + (2\Delta/\Gamma)^2]^2} v. \quad (1.8)$$

Therefore the force, for small velocities and weak intensities $I/I_{sat} \ll 1$, can be well approximated by a linear expression:

$$\begin{aligned} F(v) &= -\alpha v; \\ \alpha &= 4\hbar k^2 \frac{I}{I_{sat}} \frac{-2\Delta/\Gamma}{[1 + (2\Delta/\Gamma)^2]^2}. \end{aligned} \quad (1.9)$$

Indeed, as depicted in Fig. 1.2, for a positive value of the damping coefficient α the force has a negative gradient $\partial F/\partial v < 0$ at $v = 0$. Moreover, note that only for red frequency detuning $\Delta = \omega - \omega_0 < 0$ this force opposes the velocity, thus resulting in a viscous damping force that slows the atomic motion.

1.1.3 Doppler cooling limit

In an ideal situation in which the atomic motion is unperturbed, the above described cooling techniques would decelerate the atoms to $v = 0$ and reach zero temperature. A result that is clearly not physical. Indeed, the momentum exchange itself, responsible of the scattering force, is source of a heating mechanism. For instance, if we think of an atom that absorbs a photon able to stop its motion, the subsequent spontaneous emission of a new photon will make the atom move again. Conversely, if an atom at rest absorbs a photon, it gains kinetic energy. These two processes contribute to fluctuations in the total force acting on the atoms. For a single laser beam we can express those contributions as:

$$\mathbf{F} = \mathbf{F}_{abs} + \delta\mathbf{F}_{abs} + \mathbf{F}_{spont} + \delta\mathbf{F}_{spont}, \quad (1.10)$$

where, on average, the force arising from absorption is the scattering force we just derived and the force coming from the random kicks of the spontaneous emitted photons is zero. While for an atom that is immersed in two counter-propagating beams those forces tend to cancel out, their respective fluctuations $\delta\mathbf{F}_{abs}$ and $\delta\mathbf{F}_{spont}$, instead, are cumulative. Therefore, to determine a minimum value of the velocity and temperature reachable with the Doppler cooling technique, we have to imagine that the decay produced by a spontaneous emission of a photon or by the absorption of a photon, causes the atom to experience a sort of Brownian motion in the real space. In the momentum space we can interpret it as a random walk with step size $\hbar k$ and step frequency $2\Gamma_{scatt}$, the factor 2 due to the two counter-propagating beams.

In the case of the average fluctuation $\overline{\delta\mathbf{F}_{spont}}$, each spontaneous emission is followed by a change in the atom velocity equal to the recoil velocity v_r . As a consequence, the atom is subject to a random walk of the velocities along the laser beam of step v_r . The mean square displacement is $\overline{v^2} = \Gamma_{scatt} t v_r^2$, where $N = \Gamma_{scatt} t$ is the average number of photons scattered by the atom over time t . Projecting the mean square displacement along the z axis direction, it becomes:

$$\left(\overline{v_z^2}\right)_{spont} = \eta v_r^2 \Gamma_{scatt} t, \quad (1.11)$$

where $\eta = \langle \cos^2(\vartheta) \rangle$, being $\hbar k \cos(\vartheta)$ the emission direction of the spontaneous emitted photon ($\eta = 1/3$ for isotropic spontaneous emission).

The average fluctuation $\overline{\delta F_{abs}}$, instead, is due to the fact that the absorption of a photon from an atom is a random event. The atom, indeed, does not always absorb the same number of photons over a time period t . Moreover, each absorption is followed by a spontaneous emission of a photon with an average number of events again equal to $N = \Gamma_{scatt}t$. Similarly to the former case, the absorption process induces a random walk but in one dimension since all the absorbed photons have the same direction. The mean square displacement in the space of velocities, therefore, is:

$$\left(\overline{v_z^2}\right)_{abs} = v_r^2 \Gamma_{scatt} t. \quad (1.12)$$

Thereby, the atomic sample is heated and the force acting on it results in a competition between the two phenomena of heating and damping. As a consequence, the steady state of the system has a nonzero kinetic energy.

Taking into account the fluctuations discussed above for the scattering force, Newton's second law gives:

$$\begin{aligned} \frac{d}{dt} \left(\frac{1}{2} M \overline{v_z^2} \right) &= \frac{1}{2} M \frac{d}{dt} \underbrace{(\eta v_r^2 2\Gamma_{scatt} t + v_r^2 2\Gamma_{scatt} t)}_{\text{Heating}} \underbrace{- \alpha \overline{v_z^2}}_{\text{Cooling}} \\ &= \frac{1}{2} M (1 + \eta) v_r^2 2\Gamma_{scatt} - \alpha \overline{v_z^2} \\ &= 2E_r 2\Gamma_{scatt} - \alpha \overline{v_z^2} \end{aligned} \quad (1.13)$$

where the factor 2 before Γ_{scatt} accounts for the two beams, while $E_r = mv_r^2/2$ is the recoil energy and $1 + \eta$, for the case in three dimensions, becomes $1 + 3\eta = 2$. From this equation, we can clearly see this competitive behavior of heating and cooling. In particular, at equilibrium the rates of heating and cooling, underlined in Eq. (1.13), are equal. Therefore, we can equal to zero the time derivative and, rewriting the damping coefficient α in terms of Γ_{scatt} , we get the mean square velocity in the six beams molasses configuration along the z direction (similarly for x and y directions):

$$\overline{v_z^2} = \frac{\hbar \Gamma}{M} \frac{1 + \left(\frac{2\Delta}{\Gamma}\right)^2}{4 \left(\frac{-2\Delta}{\Gamma}\right)}. \quad (1.14)$$

According to the equipartition theorem, the z -component of the kinetic energy of motion is related to temperature by the equation $\frac{1}{2} M \overline{v_z^2} = \frac{1}{2} k_B T$. This leads to the equation:

$$k_B T = \frac{\hbar \Gamma}{4} \frac{1 + \left(\frac{2\Delta}{\Gamma}\right)^2}{\left(\frac{-2\Delta}{\Gamma}\right)}. \quad (1.15)$$

Minimizing the latter as a function of $(-2\Delta/\Gamma)$, we obtain a minimum detuning value of $\Delta = -\Gamma/2$ that leads to a minimum velocity reachable with Doppler

cooling as:

$$\left(\overline{v_z^2}\right)_{min} = \frac{\hbar\Gamma}{2M}. \quad (1.16)$$

The minimum temperature found in these conditions is:

$$T_D = \frac{\hbar\Gamma}{2k_B}, \quad (1.17)$$

called the *Doppler temperature* or *Doppler cooling limit*. This remarkable result shows that the final temperature of atoms in an Optical Molasses is proportional only to the natural line-width Γ of the excited state, and is independent of the optical wavelength, atomic mass, laser intensity. For ^{87}Rb it is $T_D = 146 \mu\text{K}$ much bigger than the recoil temperature due to the energy transferred by a single photon that for rubidium is $T_r = 362 \text{ nK}$. The correspondent most probable velocity at Doppler temperature is $v_D = 16 \text{ cm s}^{-1}$, much bigger than the recoil velocity $v_r = 5.88 \text{ mm s}^{-1}$ but smaller than the molasses velocity capture range $v_c = 4.68 \text{ m s}^{-1}$.

1.1.4 Below the Doppler cooling limit

From an experiment conducted in 1988 [15] to measure the temperature of a gas of sodium atoms released from an OM, it emerged that the measured Doppler temperature ($T_D^{exp} = 43 \pm 20 \mu\text{K}$) was surprisingly lower than the one calculated from theory ($T_D^{theo} = 240 \mu\text{K}$) as illustrated in the previous section. Results confirmed by other subsequent experiments [16]. Since then, a new picture of OM needed to be developed in response to this evidence. Two groups in 1989 [17, 18] advanced the idea that the multiplicity of sub-levels of the atomic state (Zeeman states and hyperfine structure) must be included in the picture, the simple two level scheme for the atomic structure was inadequate to describe a 3-D OM. Furthermore, optical pumping among these sub-levels needed to be considered too [19]. Polarized light, indeed, interacts with the hyperfine structure and can be exploited to reach ultra-low temperatures. See Fig. A.1 in Appendix A for the Rubidium internal atomic structure exploited in this thesis.

The essential feature of these models is the non-adiabatic following of moving atoms into a light field that varies in space. This sub-Doppler cooling technique takes the name *polarization gradient cooling* or *Sisyphus cooling*. This cooling process, indeed, recalls the Greek myth of Sisyphus condemned for eternity to roll a giant stone up a hill only to loose it every time he reaches the proximity of the top, thus repeating the climb forever.

It is possible to realize a light field polarization that varies in space, for instance, considering two counter-propagating laser beams that have linear orthogonal polarizations (lin \perp lin). The superposition of these two beams realizes a field

that has a polarization that varies on the wavelength scale along the laser beams direction. The atoms that move in this polarization gradient, because of their multilevel structure, will be coupled to the light field differently at different positions depending on the light polarization. Furthermore, the nearly resonant light that drives the transition will also shift the atomic energy levels. These processes cause a selective absorption of the photons from one or the other beams, thus enhancing the cooling efficiency. Like Sisyphus climbing a hill, the atoms moving through the light field must increase their potential energy because of the change in the light polarization. After traveling a distance corresponding to the hill top of the potential, the atoms are closer to resonance and optically pumped to a lower energy level forced to climb the potential again. In the climbing stage the kinetic energy is converted in potential energy that is subsequently radiated away by spontaneous emission. Therefore “*An atom sees itself walking in a swamp of molasses, with each planted foot sinking down into a lower energy state. The next step requires energy to lift the other foot up and out of the swamp, and with each sinking step, energy is drained from the atom*” [20]. As a result they are doomed to be always climbing hills, losing energy in the process and hence cooled. Even if also this sub-Doppler cooling process is limited over a range of atomic velocities, its damping constant α is much larger than for the Doppler cooling. The correction to the prediction based on the classical molasses theory, brings to a minimum achievable temperature proportional to $I/|\Delta|$, for $\Delta \gg \Gamma$. In this case, where the temperature reachable depends only on the laser intensity and the detuning, the only limiting quantity is the photon recoil momentum $\hbar\mathbf{k}$. The randomness of this event, in fact, puts a lower limit for the velocities $v_{min} \sim v_r$. However, the temperature and density limits of laser cooling can be surpassed by the technique of *evaporative cooling* of trapped atoms that does not require laser cooling and that will be treated subsequently in this chapter.

1.2 Trapping neutral atoms

The atoms moving in a molasses spend in it a time of the order of few milliseconds, a lifetime not long enough to reach the right number of atoms necessary for the final goal of a degenerate quantum gas as the case of a Bose-Einstein condensate for our experiment. To reach condensation, indeed, a phase-space density¹ of $\rho_\phi \geq 2.612$ is required and it is reached in several seconds of experimental cycle, as we will discuss in detail in the next section. A new idea for holding more atoms is needed such that, combined with the strong cooling mechanism of the OM, ensures the accumulation of big sources of cold atoms.

¹ $\rho_\phi = n\lambda_{dB}^3$, where λ_{dB} is the de Broglie wavelength and n the numerical density of atoms.

During the 1980s many efforts have been done in the community of coolers and trappers towards the goal of trapping atoms via optical forces, as described by Steven Chu in his Nobel Lecture in 1998 [20]. However, traps strictly based on the scattering force seemed to be not sufficient because of a no-trapping theorem referred to as the *Optical Earnshaw theorem* [21,22]. As we discussed above, even if the combination of six beams exerts a radiation pressure on atoms forcing them to be in the small portion of space where they cross, the latter can escape from it. Indeed, the scattering force acting on the atoms does not imply any confining mechanisms that would push them to the center of the trap. The Earnshaw theorem for electrostatics simply states that a scattering force-based trap is impossible provided F_{scatt} is proportional to the laser intensity I ; there cannot be a region in space where all force lines of F_{scatt} point inward to a stable trapping point. Indeed, since $\nabla \cdot F_{scatt} = 0$ any region in empty space must have the net intensity flux inward equal to the flux outward [20]. In 1986 Pritchard, Carl Wieman, and their colleagues observed that “*the Optical Earnshaw theorem does not always apply to atoms and that it is possible to confine atoms by spontaneous light forces produced by static laser beams*”, advancing the hypothesis that “*the atomic transition rate cannot depend only on the light intensity*” [23]. But it was only in 1987, when they asked Steven Chu [24] to join the team, that the first *Magneto Optical Trap* (MOT) was experimentally built [25] and working! The basic idea for the trap was due to Jean Dalibard [20], stimulated by a talk given by Dave Pritchard on how the Earnshaw theorem could be circumvented. Simply inserting a pair of magnetic-field coils into the apparatus for the 3-D molasses, one can realize an hybrid trap for neutral atoms employing both optical and magnetic field gradients. The development of the MOT was an exciting moment in the large international community that was working on it and it paved the way to many subsequent experiments in the field of laser-cooled atoms like Bose-Einstein condensation.

1.2.1 Interaction with a static magnetic field

A brief understanding of the interaction between a static magnetic field and a neutral atom is necessary before introducing the Magneto-Optical Trap theory. The discovery of the mechanical action of magnetic fields on neutral atoms having a magnetic dipole moment μ dates back to 1924 with the Stern and Gerlach experiment. The interaction between the momentum μ and an external magnetic field \mathbf{B} produces a force $\mathbf{F} = \nabla(\mu \cdot \mathbf{B})$, given that $E = -\mu \cdot \mathbf{B}$ is the energy that the classical momentum μ , immersed in the magnetic field \mathbf{B} , perceives. The magnetic moment of an atom, owing to its composite structure, is made by the contribution of the orbital angular momentum of its electrons \mathbf{L} , of the electronic spin \mathbf{S} and of the nuclear spin \mathbf{I} . Assuming the simple case of an alkaline atom, as

the case of Rubidium (for more details, see Fig. A.1 in Appendix A for the Rubidium internal atomic structure exploited in this thesis), a single external electron will determine the value of \mathbf{L} and \mathbf{S} . The coupling between nuclear spin \mathbf{I} and the total electron angular momentum $\mathbf{J} = \mathbf{L} + \mathbf{S}$ induces an hyperfine structure of the atomic ground level described by the *hyperfine Hamiltonian*:

$$H_{hfs} = A_{hfs} \mathbf{J} \cdot \mathbf{I}, \quad (1.18)$$

where A_{hfs} is the magnetic dipole constant. The unperturbed hyperfine Hamiltonian H_{hfs} is diagonal in the representation of the state base $|F, m_F\rangle$, where \mathbf{F} is the total angular momentum $\mathbf{F} = \mathbf{I} + \mathbf{J}$ and m_F is its component along the \hat{z} axis. In absence of any external field, each F sub-level is $(2F + 1)$ -fold and degenerate, a degeneracy that is broken when interacting with an external magnetic field \mathbf{B} . This effect of splitting of a spectral line into several components in the presence of a static magnetic field was discovered in 1896 by P. Zeeman and takes his name. The interaction term due to the Zeeman effect that contributes to the total Hamiltonian of the system is:

$$\begin{aligned} H_B &= -\boldsymbol{\mu} \cdot \mathbf{B} \\ &= \frac{\mu_B}{\hbar} (g_S \mathbf{S} + g_L \mathbf{L} + g_I \mathbf{I}) \cdot \mathbf{B} \\ &= \frac{\mu_B}{\hbar} (g_S S_z + g_L L_z + g_I I_z) B_z, \end{aligned} \quad (1.19)$$

where the magnetic field \mathbf{B} is along the atomic quantization axis \hat{z} and $\mu_B = e\hbar/2m_e \approx 9.274 \cdot 10^{-24} \text{ J T}^{-1}$ is the Bohr magneton. The quantities g_S , g_L and g_I are the electron spin, electron orbital, and nuclear Landé *g-factors* respectively. In particular \mathbf{S} couples to \mathbf{B} with a *g-factor* of $g_S \approx 2$, \mathbf{L} couples to \mathbf{B} with a *g-factor* of $g_L = 1$, while g_I couples with \mathbf{B} as experimentally measured in [26]. If the magnetic field is weak, meaning that the hyperfine structure term dominates respect to the Zeeman energies ($H_B \ll H_{hfs}$), we can use the eigenfunction of the hyperfine structure of quantum number F to rewrite the Zeeman Hamiltonian along \hat{z} as:

$$H_B = \frac{\mu_B}{\hbar} g_F F_z B_z. \quad (1.20)$$

Then, we can treat this term perturbatively and use a vector model in which we project \mathbf{J} and \mathbf{I} along \mathbf{F} to formulate the following expression of the Landé g_F factor:

$$\begin{aligned} g_F &= g_J \frac{F(F+1) + J(J+1) - I(I+1)}{2F(F+1)} + g_I \frac{F(F+1) + I(I+1) - J(J+1)}{2F(F+1)} \\ &\simeq g_J \frac{F(F+1) + J(J+1) - I(I+1)}{2F(F+1)}, \end{aligned} \quad (1.21)$$

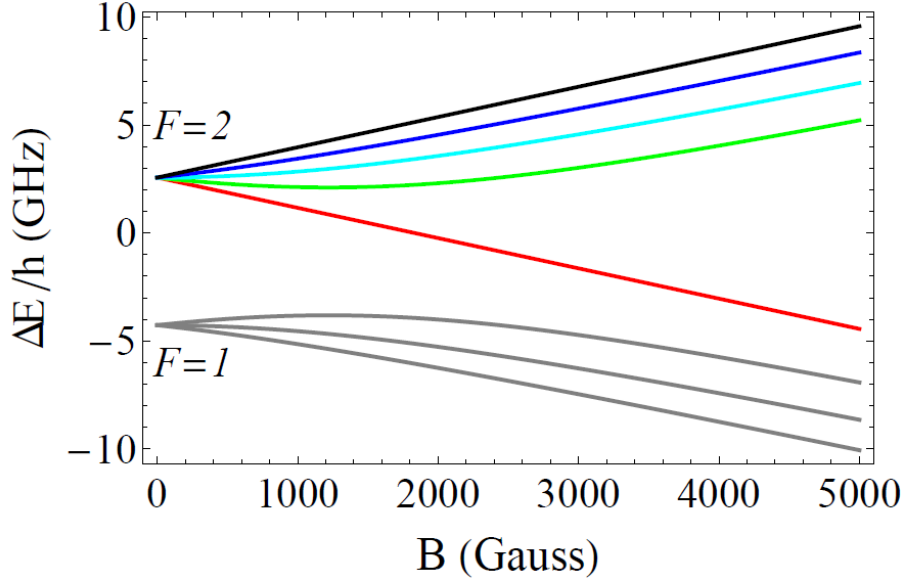


Figure 1.3: *Breit-Rabi diagram*. Ground level hyperfine structure of ^{87}Rb ($5^2S_{1/2}$) in an external magnetic field. The color legend for the Zeeman states of $F = 2$ is: $m_F = 2$ (red), $m_F = 1$ (blue), $m_F = 0$ (light blue), $m_F = -1$ (green) and $m_F = -2$ (black). The eight levels groups according to four sub-levels with spin up and four sub-levels with spin down. Image from Ref. [52].

given that:

$$\begin{aligned} \mathbf{J} &= \frac{\langle \mathbf{J} \cdot \mathbf{F} \rangle}{F(F+1)\hbar^2} \mathbf{F}, \\ \mathbf{I} &= \frac{\langle \mathbf{I} \cdot \mathbf{F} \rangle}{F(F+1)\hbar^2} \mathbf{F}. \end{aligned} \quad (1.22)$$

The second expression in Eq. (1.21) neglects the nuclear term with an approximation of the 0.1%, since g_I is much smaller than g_J . The latter can be similarly computed, in the vector model, projecting \mathbf{L} and \mathbf{S} along \mathbf{J} axis and obtaining:

$$g_J \approx 1 + \frac{J(J+1) + S(S+1) - L(L+1)}{2J(J+1)}, \quad (1.23)$$

where the approximation comes from $g_S \approx 2$ and $g_L = 1$.

Summarizing, the result is that, for weak magnetic fields, the Zeeman Hamiltonian H_B due to the interaction with \mathbf{B} , perturbs the zero-field eigenstates of the hyperfine Hamiltonian H_{hfs} splitting the adjacent magnetic sub-levels of a quantity $\Delta E_{|F, m_F\rangle} = \mu_B g_F m_F B_z$. The splitting in this regime is linear and is called the *anomalous Zeeman effect*. In the case where the magnetic field is dominant ($H_B \gg H_{hfs}$), instead, it is called the *Paschen-Back effect*. Here the Zeeman Hamiltonian has to be diagonalized for eigenfunctions where, this time, J and

I are good quantum numbers and the hyperfine coupling is treated in perturbation theory. A general solution valid for both weak and strong field cases can be derived by an exact diagonalization of the total Hamiltonian and leading to the *Breit-Rabi formula* [27], whose diagram is depicted in Fig. 1.3. The energy levels evolve as a function of the magnetic field passing from the low-field anomalous Zeeman effect to the high-field Paschen-Back effect. We can see that for low magnetic fields the Zeeman shift is to a very good approximation linear.

1.2.2 Magnetic trapping

Exploiting the force that arises from the atomic interaction with an inhomogeneous magnetic field, several magnetic traps with different geometries can be realized. Note that the direction of the force $\mathbf{F} = \nabla(\boldsymbol{\mu} \cdot \mathbf{B})$ depends on the magnetic moment $\boldsymbol{\mu}$ orientation respect to the magnetic field \mathbf{B} direction. In particular, assuming the magnetic moment orientation is preserved during the atomic motion in the field, one can build a trap such that the resultant force is a restoring force. Therefore, in presence of a minimum of $|\mathbf{B}|$ and provided that $\boldsymbol{\mu} \cdot \mathbf{B} < 0$, the atoms that move in the magnetic field resent a restoring force that tends to confine them in the minimum region. Fig. 1.3, for instance, shows that ^{87}Rb atoms can be trapped in the states $|F = 1, m_F = -1\rangle$ and $|F = 2, m_F = 1, 2\rangle$, thus called *low field seeking states*; while the others for which $\boldsymbol{\mu} \cdot \mathbf{B} > 0$ are repelled from the trap and called the *high field seeking states*. In this regard, it is worth noting that a full control of the *spin-flips* investigated by E. Majorana [28] is necessary in building a magnetic trap. The probability of spin-flip transitions for polarized atoms in the presence of a rapidly varying magnetic field is, indeed, crucial in order to preserve the adiabatic following between the magnetic momentum and magnetic field orientations, otherwise the atoms may be ejected instead of confined by the fields of the trap. This spin-flip problem becomes critical when the atoms are in proximity of the trap center where the field is zero. In this region, in fact, the atoms temperature is lower and their precession becomes too small compared to the rate of change of the field orientation. The transition from a spin orientation to the other is here non-adiabatic and the atoms are no more in the low field seeking states and expelled from the trap. In particular, the condition for adiabatic motion can be written as $\omega_Z \gg |dB/dt|/B$, where $\omega_Z = \mu B/\hbar$ is the Larmor precession rate in the field.

1.2.3 Magneto-Optical Trap

A *Magneto-Optical Trap* consists in the combination of six orthogonal and counter-propagating laser beams, like in the Optical Molasses, that cross in the center of a magnetic quadrupole trap made by a pair of coils in anti-Helmholtz configura-

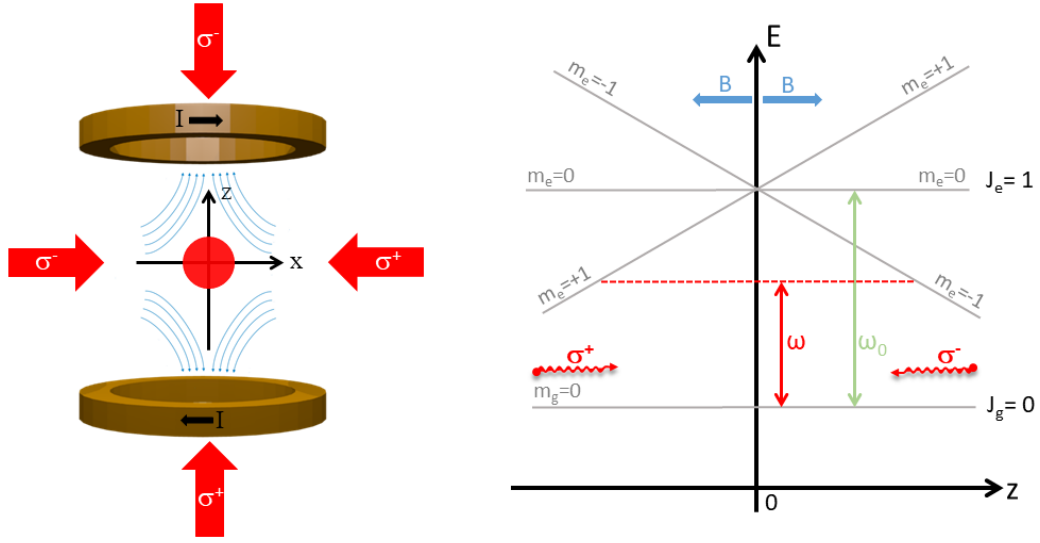


Figure 1.4: *MOT scheme*. Left-hand side: The combination of six orthogonal and counter-propagating beams crossing in the center of a quadrupole magnetic field generated by a pair of anti-Helmholtz coils, realizes a MOT. For it to work, is necessary that the laser beams have the shown circular polarization. The beam pair directed along \hat{y} is orthogonal to the page and its polarization is oriented as well as for the beam directed along \hat{x} . Right-hand side: Schematic of the MOT working principle for an atom with a transition $J_g \rightarrow J_e$. The Zeeman splitting induced by the presence of the magnetic field B , depends on the atom's position z . A couple of counter-propagating and orthogonal beams circularly polarized as shown, interact with the atom. The selection rules for transitions between the different m_e lead to an imbalance in the radiation pressure provided by the beams thus resulting in a confinement effect of the atoms towards the center of the trap. Image adapted from Ref. [7].

tion. The laser beams need to be prepared in such a way that their polarization is circular and opposite for each counter-propagating couple of beams as depicted in the left-hand side of Fig. 1.4. This scheme provides cooling and trapping depending on both inhomogeneous magnetic field and radiative selection rules to exploit both optical pumping and strong scattering force. The MOT working principle can be better understood if we refer to the simple case in one dimension depicted in the right-hand side of Fig. 1.4. Here we consider atoms that have two levels, a ground state and an excited state with angular momentum $J_g = 0$ and $J_e = 1$ respectively. The atoms slowly move in a linearly inhomogeneous magnetic field $B = B(z)$ such as that generated by a magnetic quadrupole field that is zero at the center of the quadrupole coils ($z = 0$). Owing to the Zeeman effect, the magnetic field induces a splitting of the magnetic sub-levels $m_e = \{-1, 0, +1\}$ of $J_e = 1$, their energies linearly varying with the atoms position along z . Two counter-propagating laser beams of opposite circular polarization, each detuned below the zero-field atomic resonance $J_g \rightarrow J_e$ by Δ , are incident on the atoms

as shown in figure. The Zeeman effect shifts up the excited state $m_e = +1$ for $B > 0$, whereas $m_e = -1$ is shifted down. As a consequence, depending on light polarization, we will have the following cases occurring:

- for atoms in $z > 0$: photon-absorption from the beam with polarization σ^- , indeed, makes the atoms undergo the transition $m_g = 0 \rightarrow m_e = -1$ that is closer to resonance rather than $m_g = 0 \rightarrow m_e = +1$ that is further out of it; therefore the more light is scattered from the σ^- beam than from σ^+ , thus pushing the atoms towards $z = 0$;
- for atoms in $z < 0$: for the $m_e = \pm 1$ states the situation is reversed and more light is scattered from the σ^+ beam, again pushing the atoms towards the trap center $z = 0$.

We can compute the force experienced by the atoms in a MOT as the sum of the scattering forces exerted by each of the two laser beams. The resulting expression is similar to the force induced on the atoms moving in an Optical Molasses as previously shown in Subsec. 1.1.2. However, given that in the MOT case the Zeeman effect shifts the atomic resonance, we need to include the Zeeman shift $\mu_B B_z (g_e m_e - g_g m_g)$ in the laser detuning Δ . For small distances from the trap center we can consider the magnetic field linearly varying with it $B(z) = B_0 z$. Assuming for simplicity that $(g_e m_e - g_g m_g) \sim 1$, the Zeeman shift of the atomic levels at displacement z can be written as $\mu_B B_0 z = \beta z$. Moreover, assuming a small Zeeman shift $\beta z \ll \Gamma$ and small velocities $k v \ll \Gamma$, we have:

$$\begin{aligned} F_{MOT} &= F_{scatt}^{\sigma^+}(\omega - kv - (\omega_0 + \beta z)) - F_{scatt}^{\sigma^-}(\omega + kv - (\omega_0 - \beta z)) \\ &\simeq -2 \frac{\partial F}{\partial \omega} kv + 2 \frac{\partial F}{\partial \omega_0} \beta z. \end{aligned} \quad (1.24)$$

Since the force depends on the frequency detuning $\Delta = \omega - \omega_0$, we have $\partial F / \partial \omega_0 = -\partial F / \partial \omega$ such that:

$$\begin{aligned} F_{MOT} &= -2 \frac{\partial F}{\partial \omega} (kv + \beta z) \\ &= -\alpha v - \frac{\alpha \beta}{k} z. \end{aligned} \quad (1.25)$$

The Zeeman effect produces an imbalance in the scattering force that, similarly to damping in the molasses, induces a restoring force of spring constant $\alpha \beta / k$. The atoms subject to this force experience a damped harmonic motion $\ddot{z} + \gamma \dot{z} + \omega_{trap}^2 z = 0$, where the damping coefficient γ and the trap frequency ω_{trap} can be retrieved from Eq. (1.25). As a result, the combined employing of a quadrupole magnetic field together with the action of radiation pressure slows the atoms as in an Optical Molasses and pushes them towards the center of the

trap by means of a force that depends on displacement. Hence the effect here operates both in velocity (Doppler effect) and position (Zeeman effect) space, and not only in the velocity space as for molasses.

The scheme discussed so far can be easily extended to two and three dimensions, the latter by using six laser beams. In a more general way the scheme can work for any transition of the kind $J_g \rightarrow J_e = J_g + 1$.

A MOT has much higher capture velocities than Optical Molasses, it is for this reason that a typical experiment of Bose-Einstein condensation first exploits a MOT to quickly collect a large number of atoms and only after this, switching off the magnetic field, laser-cools the atoms in an Optical Molasses. As we will see in the description of our experimental setup, this sequence allows one to accumulate more atoms hence reaching much higher atomic densities with respect to molasses itself. For instance, to have a quantitative idea, we can compute the capture velocity of a MOT and compare it to the OM capture velocity computed in Subsec. 1.1.1. Considering a Rubidium MOT whose beams diameter is 10 mm long, equal to the stopping distance L_0 , the corresponding capture velocity is $v_c(\text{Rb-MOT}) = \sqrt{d v_r \Gamma} = 23 \text{ m s}^{-1}$. Therefore, any atom with a speed equal or lower than 23 m s^{-1} entering the trap volume will be trapped and cooled in the MOT. While much slower atoms are captured in an OM that have capture velocity of 4.68 m s^{-1} . An estimate of the number of atoms trapped in a MOT can be retrieved by its loading dynamics [31]. Let us consider the rate equation that describes the temporal trend of the number of trapped atoms in the MOT:

$$\frac{dN}{dt} = R - \gamma N - B \int n_{\text{MOT}}^2(r, t) dV, \quad (1.26)$$

where the first term describes the loading rate R of atoms from the background vapor, while the next two terms describe the loss of atoms from the MOT due to collisions with the hot background gases and due to two body intra-trap collisions, respectively. γ is the loss rate due to collisions between hot background particles and cold trapped ones, B is the loss rate coefficient of the intra-trap term and n_{MOT} is the MOT atom density. In the case of loading atoms from a vapor, we can neglect the last term and the equilibrium number of atoms in a MOT is $N_{eq} = R/\gamma$. Under normal operating conditions where v_c is very small compared to the average thermal speed of the background particles, we can calculate the loading rate R obtaining:

$$R = \frac{2A v_c^4 n}{\pi^2 v_{th}^3}, \quad (1.27)$$

where $v_{th} = \sqrt{8k_B T / (\pi m)}$ is the mean thermal velocity of the background particles, A is the cross-sectional area of the trapping region and n is the atomic density in the vapor. Given that the capture velocity is $v_c = \sqrt{d v_r \Gamma}$ and that the

trapping area of the beams is $A = d^2$, together with Eq. (1.27) we have that the loading rate R is proportional to the fourth-power of the beam diameter d . As a consequence, also the number N_{eq} of trapped atoms is proportional to d^4 :

$$N_{eq} = \frac{2v_r^2 \Gamma^2 n}{\pi^2 \gamma v_{th}^3} d^4. \quad (1.28)$$

In the case of a Rubidium MOT made by cooling beams with a diameter of 1 cm, a number of 10^8 - 10^9 atoms can be trapped reaching temperatures of about $100 \mu\text{K}$. Depending on the dimension of the beams and on the different experimental configurations, a MOT can reach a volume ranging from several (or a fraction of) mm^3 to cm^3 . Moreover due to the trapped atoms fluorescence, it is possible to see a MOT with naked eye shining with different bright colors depending on the atomic species.

1.2.4 Quadrupole and Ioffe-Pritchard traps

The simplest trap that realizes magnetic confinement of the atoms is the *quadrupole trap* [29] originally suggested by W. Paul. It is made by two identical coils carrying opposite currents as depicted in Fig. 1.5. This configuration is called anti-Helmholtz and generates a spherical quadrupolar field that is zero at the center of the trap. It increases linearly from the center as:

$$\mathbf{B}(\mathbf{r}) = B'_x x \hat{\mathbf{e}}_x + B'_y y \hat{\mathbf{e}}_y + B'_z z \hat{\mathbf{e}}_z, \quad (1.29)$$

being $B'_x + B'_y + B'_z = 0$, in order to satisfy Maxwell's equations. The cartesian coordinate vectors $\hat{\mathbf{e}}_i$ are along the quadrupole main axes. Therefore, the trapping potential providing linear confinement around $\mathbf{r} = 0$, is:

$$\Delta E_{|F, m_F\rangle} = \mu_B g_F m_F \sqrt{(B'_x x)^2 + (B'_y y)^2 + (B'_z z)^2}. \quad (1.30)$$

From an experimental point of view, this trap is very easy to make and powerful. Needing only a pair of coils, its construction and optical access is very simple. Furthermore, the confinement that it is capable of reaching is the strongest with respect to other geometries that we will describe later and that have a parabolic potential. For this reason the quadrupole trap was widely used in the first experiments of neutral atom trapping. However, the Majorana spin-flips mentioned in Subsec. 1.2.2, constitute an obstacle for its trapping success. Indeed, moving nearby the position of zero-field, the atoms experience an abrupt change in the magnetic field direction thus undergoing a spin flip process which expels them from the trap. To overcome the spin-flip problem, many schemes have been used

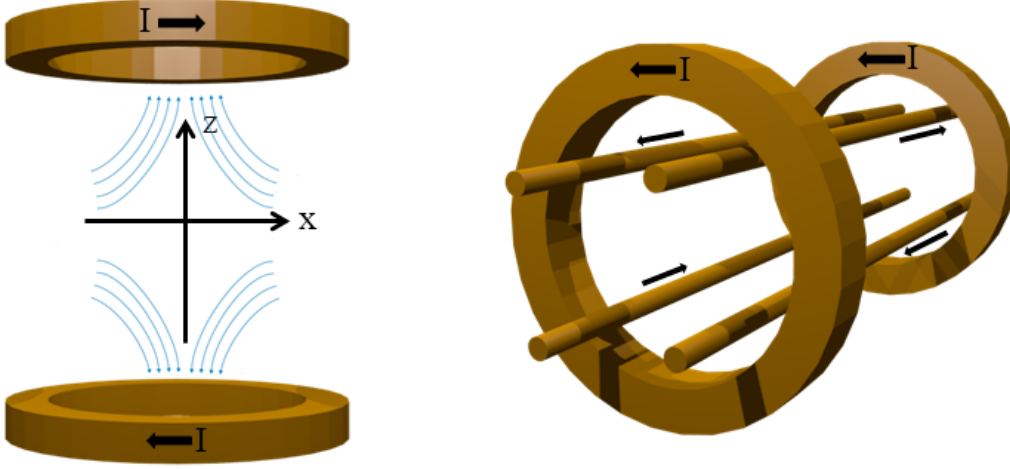


Figure 1.5: *Quadrupole and Ioffe-Pritchard traps*. Left-hand side: Two coils configuration to generate a three-dimensional quadrupole trap that is zero at the center of the trap. Right-hand side: The Ioffe-Pritchard trap configuration is obtained with four bars of opposite currents providing the transverse confinement and a pair of pinch coils providing the axial confinement.

and they can essentially be grouped in three types. When Bose-Einstein condensation was first observed, for instance, a *TOP-trap* (time-averaged orbiting potential) was developed. It consists in adding to the quadrupole configuration, a weak magnetic field fast rotating in the horizontal plane. In this way the instantaneous potential that arises is parabolic, like a moving cup in which the atoms are confined. The second solution that was developed is an *optical-plug trap*. In this case the center of the quadrupole trap, where the field vanishes, is a hole from which the atoms can escape. The idea was to optically plug this hole with the repulsive force produced by a laser beam passing through the hole and having an higher frequency respect to the atomic resonance. In this way the atoms are turned away from this region and the hole is closed. The third solution is a widely used scheme and is called *Ioffe-Pritchard trap* [30]. It is made by the combination of a linear magnetic quadrupole produced by four straight conductors, in which the current flows as depicted in Fig. 1.5, and an axial bias magnetic field provided by two co-axial ending coils carrying currents that flow in the same direction (*pinch coils*). In the case of axial symmetry, the trapping field close to the trap center is given by:

$$\mathbf{B}(\mathbf{r}) = B_0 \begin{pmatrix} 1 \\ 0 \\ 0 \end{pmatrix} + B' \begin{pmatrix} 0 \\ -y \\ z \end{pmatrix} + \frac{B''}{2} \begin{pmatrix} x^2 - (y^2 + z^2)/2 \\ -xy \\ -xz \end{pmatrix}. \quad (1.31)$$

B' is the gradient of the two-dimensional quadrupole field in the yz -plane, B_0 is the constant term coming from the bias homogeneous field and B'' is the curva-

ture along x . The magnetic field modulus, approximated to the second order in r , is:

$$\mathbf{B}(\mathbf{r}) \approx B_0 + \frac{B''}{2}x^2 + \frac{1}{2} \left(\frac{B'^2}{B_0} - \frac{B''}{2} \right) (y^2 + z^2), \quad (1.32)$$

it provides a harmonic confinement of atoms, of mass m and magnetic moment $\mu = \mu_B g_F m_F$, with trap frequencies:

$$\omega_{axial} = \sqrt{\frac{\mu}{m} B''} \quad \text{and} \quad \omega_{radial} = \sqrt{\frac{\mu}{m} \left(\frac{B'^2}{B_0} - \frac{B''}{2} \right)}. \quad (1.33)$$

The Ioffe-Pritchard trap has several variants as long as its field geometry is preserved. In this regard, for instance, a Ioffe-Pritchard trap, but also a quadrupole trap, can be implemented on a chip by means of a planar current distribution, as we will see in detail in the section describing our atom-chip layout. This new generation of traps, called *microtraps*, has many advantages ranging from their superior confinement potential to a large variety of solutions that make the manipulation of neutral atoms easier.

1.3 Bose-Einstein condensation

The Bose-Einstein condensate (BEC) is a state of matter predicted in 1924 by Albert Einstein. He generalized the ideas proposed by the Indian physicist Satyendra Nath Bose who derived, in his pioneering paper on quantum statistics, the Planck law for black-body radiation by treating the photons as a gas made of identical particles. Einstein extended this theory to an ideal gas of identical atoms with integer spin (bosons) and predicted that, at sufficiently low temperatures, the particles of the gas undergoes a phase transition such that all of them occupies together the lowest quantum state of the system. As the gas is cooled near the zero temperature, the particles are closer such that the matter waves of each individual atom start “overlapping” causing the atoms to be indistinguishable one from another. A unique “*giant matter wave*” is taking form, made by a whole synchronous oscillation: the Bose-Einstein condensate. This is how a single macroscopic wave-function arises, with a well defined amplitude and phase, as well as for a classical field. It is a new form of matter that, thanks to its macroscopic properties, makes quantum mechanics macroscopic thus allowing us to investigate it.

For a more quantitative picture, we can say that the condition for condensation to occur is when the number density $n = N/V$ (N the number of atoms and V the occupied volume) reaches the value [7]:

$$n = 2.612/\lambda_{dB}^3, \quad (1.34)$$

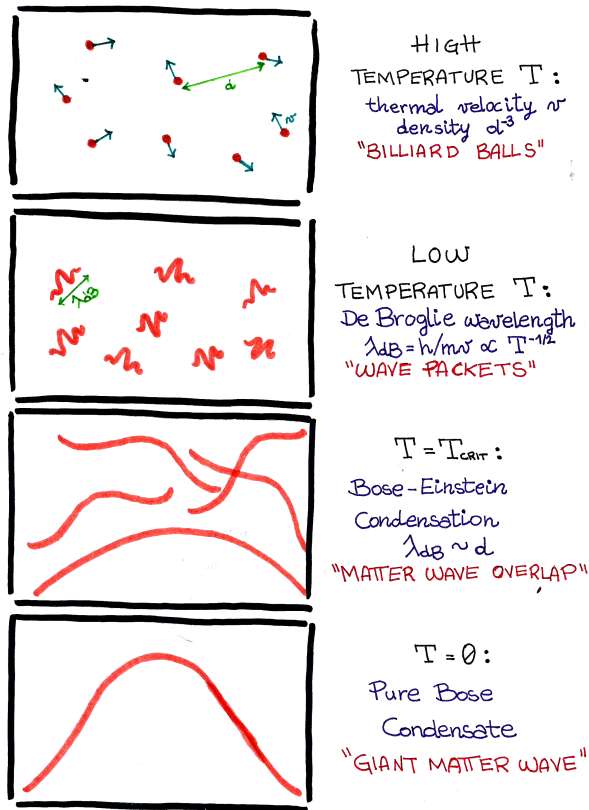


Figure 1.6: Bose-Einstein condensation. At high temperatures T , the weakly interacting gas, with velocity v and density d^{-3} , behaves as a system of “billiard balls”. At low temperatures we can describe the atoms as “wave packets” with an extension of λ_{dB} , their de Broglie wavelength. At $T = T_{crit}$ the BEC transition occurs, λ_{dB} is comparable with the interatomic distance d and “matter wave overlap”. When the temperature approaches zero, the thermal cloud disappears and a unique “giant matter wave” forms. Image and caption adapted from Wolfgang Ketterle’s Nobel Lecture [34].

where λ_{dB} is the thermal *de Broglie wavelength* defined as $\lambda_{dB} = h/\sqrt{2\pi mk_B T}$ or, in an analogous way, $\lambda_{dB} = h/(mv)$ being v the characteristic speed of the gas. The de Broglie wavelength is a measure of the delocalization of an atom, i.e. the dimension of the region in which an atom could be found if we measure it. At very low temperatures, we can now understand that quantum effects become important when λ_{dB} is comparable to the inter-atomic spacing (see Fig. 1.6). At the same time the atoms have much lower average energies (temperature) thus occupying a smaller volume near the bottom of the trap potential in which they are confined. As a consequence also the *phase-space density* $\rho(\mathbf{r}, \mathbf{p}, t)$ increases. It represents the probability that a single particle is in a region $d\mathbf{r}$ around \mathbf{r} , with momentum $d\mathbf{p}$ around \mathbf{p} at time t . The elementary volume for a gas of cold atoms is chosen to be \hbar^3 , so that the phase-space density becomes the dimensionless quantity $\rho_\phi = n\lambda_{dB}^3$. The order of magnitude of the reachable temperatures in a BEC for trapped atomic gases is $\lesssim 100$ nK.

Bose-Einstein condensation of dilute atomic gases was observed for the first time in 1995 by Eric Cornell and Carl Wieman in the laboratory of NIST-JILA University of Colorado at Boulder [32]. The condensate appeared in a cloud of ^{87}Rb at a

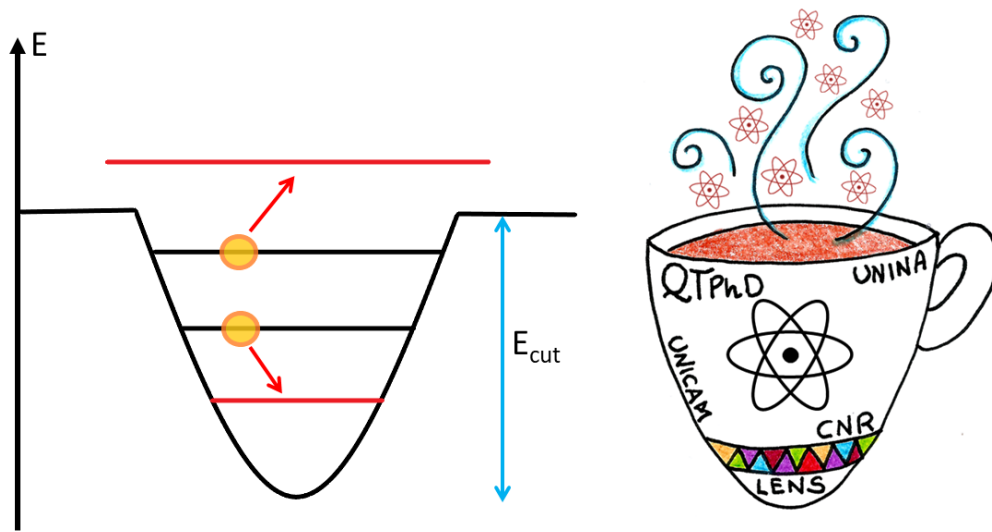


Figure 1.7: *Evaporative cooling*. Atoms are trapped in a potential well of finite depth and undergo elastic collisions. The hottest atoms escape from the trap, they are evaporated similarly to a hot cup of tea that cools down for the evaporation of surface particles. The remaining atoms have much lower energies. It is at this stage that after several collisions a new equilibrium is reached via rethermalization. The temperature of the remaining trapped gas decreases and its phase-space density increases. Figure adapted from Ref. [36].

temperature near 170 nK. Shortly after, also Wolfgang Ketterle at Massachusetts Institute of Technology (MIT) observed Bose-Einstein condensation of sodium atoms [33]. Before 1995, the challenges to reach BEC, from an experimental side, were several. Trapping conditions were necessary together with an ultra-high vacuum surrounding in order to reduce collisions with hot atoms. Moreover, very dilute gases were needed to prevent the atoms from condensing into a solid or a liquid. After all, the required ultra-low temperatures encouraged the development of new cooling techniques. Indeed, at that time the Doppler and sub-Doppler cooling techniques discussed previously were routinely achieved, nevertheless, because of the recoil limit, they allowed to reach only micro-kelvin temperatures. A process similar to evaporation that occurs in nature and inherently different from the others already discussed, was applied to atom cooling for the first time in 1988 [35]. It takes the name *evaporative cooling* and most BEC experiments exploit it in their final stage.

1.3.1 Evaporative cooling

A simple model can be used to understand the basics of evaporative cooling technique. Similarly to a cup of tea that cools down due to the evaporation of surface particles, a “cup” of atoms, made by a harmonic potential, can be cooled allowing

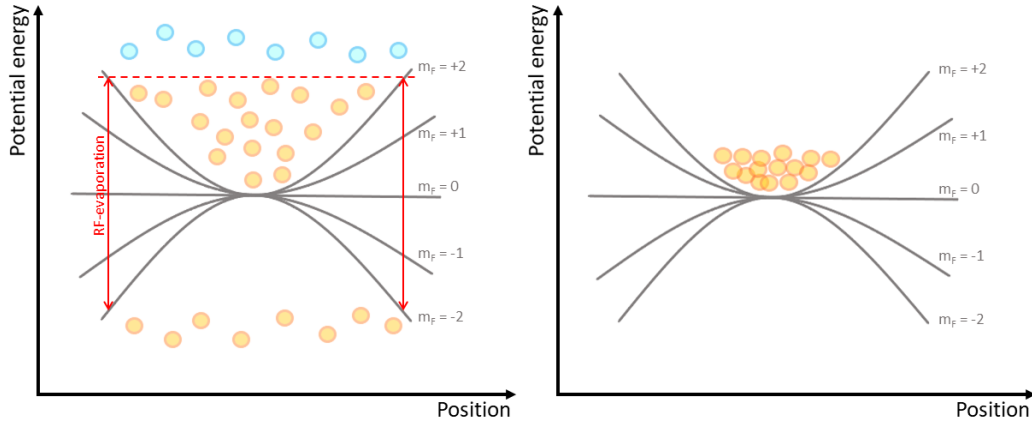


Figure 1.8: *Radio-frequency evaporative cooling*. Left-hand side: parabolic profile of energy levels in a magnetic trap. Red arrows are the RF-field that induces a transition, only for the most energetic atoms depicted in light-blue, from trapped to untrapped levels. Right-hand side: the remaining atoms thermalize at lower temperatures.

the high-energy atoms to escape from the trap thus lowering the overall temperature of the system (as pictorially shown in Fig. 1.7). We can consider evaporation as a sequence of steps following the evolution of the energy distribution described below.

- *Step 1.* The atoms have an initial Boltzmann distribution of energy $N(E) = N_0 e^{-E/k_B T_1}$ characterized by temperature T_1 ;
- *Step 2.* A cutoff energy $E_{cut} = \eta k_B T_1$ is applied (typically $\eta = 3 - 6$), such that all the hot atoms having $E > E_{cut}$ are allowed to escape from the trap;
- *Step 3.* After some time, collisions between the remaining atoms redistribute the energy among them and thermal equilibrium is re-established at a lower temperature $T_2 < T_1$ characteristic of a new Boltzmann distribution.

The Boltzmann distribution extends to infinity, therefore, at least in principle, a lower cutoff can always be found thus, iterating these steps, reaching a lower temperature is always possible. Besides the simplicity of the scheme just described, evaporative cooling is experimentally realized in a different way. As a matter of fact, the magnetic potential in which the atoms are trapped, does not change. It is the interaction with an external applied RF-field that expels the atoms from the trap. Indeed, the field flips the magnetic moments of the atoms $\Delta m_F = \pm 1$ such that the forces acting on them are anti-trapping. Moreover, the frequency of the field ω_{RF} is adjusted such that $g_F \mu_B b' r = \hbar \omega_{RF}$ and only the hotter atoms at a certain distance r from the trap center are affected (see

Fig. 1.8). After this radio-frequency cutoff, the atoms collide in search of a new thermal equilibrium stabilizing at a final lower temperature. It is important that the process of continuously lowering the RF signal is accurately tuned on the particular experimental atomic sample. The velocity of thermalization, indeed, is proportional to the elastic collisional rate $\gamma = n\sigma\bar{v}$, n being the atom density, σ the elastic scattering cross section and $\bar{v} \simeq \sqrt{k_B T/m}$ the mean velocity [6]. The evaporation process is more efficient if γ remains constant whilst \bar{v} decreases and n increases. Therefore, the evaporation time will be properly chosen according to the thermalization speed of the sample. It is worth noting that these techniques can be applied to atoms trapped with the optical dipole force as well [37].

1.3.2 Coherence of a Bose-Einstein condensate

Interesting properties arise from the description of a Bose-Einstein condensate as a collection of atoms sharing the same wavefunction. The one we want to mention in this thesis is the coherence property of a BEC. It was observed for the first time in a remarkable experiment performed at MIT carried out by the group of Wolfgang Ketterle in 1997 [38]. The experiment demonstrated the interference between two free expanding sodium condensates separated by $\sim 40 \mu\text{m}$ and created in a double-well potential formed by magnetic and optical forces. An initially elongated condensate was cut into two parts by means of the interaction with a blue-detuned laser beam. After switching off the trapping potential, such two separated condensates fall under gravity and expand for 40 ms. The absorption image, taken right after the expansion time, clearly showed an interference pattern in the overlapping zone of the two condensates. Such an experiment demonstrated that matter waves interfere like electromagnetic waves. However, a fundamental difference with optics experiments of interference, was that in the MIT experiment there was no fixed relation between the phases of the two condensates. A property that directly reflects the coherence of a Bose-Einstein condensate is, indeed, its phase. However, the phase is not an observable, being the argument of a complex number that is the macroscopic wavefunction. The observation of high-contrast interference between the two atomic BECs constituted a clear evidence for coherence in such systems. An interesting treatment that gives the tools necessary to understand and analyze the coherence and statistical properties of macroscopic matter waves associated with condensates is given in Ref. [36]. It is further shown how a relative phase between two initially independent condensates can emerge as a result of a succession of detection processes. The coherence properties demonstrated in this experiment showed that it is possible to couple out a coherent beam of matter waves from a Bose-Einstein condensate, which constitutes the definition of an *atom laser* with the same well-defined phase and wavelength like the light from a laser.

2 | Experimental apparatus: a BEC on an atom-chip

Bose-Einstein condensate-based experiments are often very elaborate. The condensate itself is a very fragile object and the efforts in reaching it and preserve its coherence are the result of several focused and balanced steps. However, the achievement of such an exotic state of matter attracted a great interest in the scientific community. In particular it stimulated the development of new extremely versatile tools for a practical improvement in realizing and manipulating such coherent atomic matter waves. In this regard, the atom-chip exploited in our experiment constitutes an example. Indeed, the use of microtraps, replacing the customary magnetic coils used to confine the atoms in standard BEC experiments, considerably simplified the overall apparatus. Additionally, the strong confinement potential reached via chip-traps allowed to gain a remarkable acceleration in the condensate time production, from minutes to a few seconds, thus benefiting the atomic physics research field. Moreover, the high degree of exquisite control that the atom-chip enables is a powerful tool too in the manipulation of the BEC internal state dynamics. The latter is fundamental in the development of the quantum protocols I want to present in this thesis work, whose success relies in the high degree of control reachable in the ultimate stages of our experimental sequence.

The experimental apparatus and a typical sequence for the preparation and manipulation of our BEC on the atom-chip is the subject of this chapter. The cooling and trapping techniques that make use of an atom-chip are described in detail in Sec. 2.1. After explaining the basic wire traps principles in Subsec. 2.1.1, I put the emphasis on the on-chip realization of a wire equivalent of the Quadrupole (Subsec. 2.1.2) and Ioffe-Pritchard (Subsec. 2.1.3) standard traps.

Our experimental setup is then detailed in Sec. 2.2. Starting from the core of our experiment, the atom-chip layout is described in Subsec. 2.2.1. When the atoms' cooling is achieved near a surface, given by the atom-chip itself, the implementation of a variant of the standard MOT is inevitable. The mirror-MOT is thus explained in Subsec. 2.2.2, together with an overview of the whole experimen-

tal apparatus. The laser system employed to generate the necessary frequencies required by our experiment is shown in Subsec. 2.2.3. A step-by-step analysis of our experimental sequence in reaching BEC is provided in Subsec. 2.2.4 and a description on how we measure it performing standard absorption imaging is reported in Subsec. 2.2.5. Finally a dedicated first analysis on how we experimentally manipulate the produced BEC, is explained in Sec. 2.3, focusing on the necessary fields that we use for this purpose: a microwave field (Subsec. 2.3.1) and a radio-frequency field (Subsec. 2.3.2).

2.1 Cooling and trapping on an atom-chip

Micro-traps can perfectly reproduce the features of standard magnetic traps for ultra-cold neutral atoms, tightly confining them and making their manipulation easier. An *atom-chip* has a completely planar geometry in which the trapping potential is provided by micro-structured current-carrying wires. It was proposed in 1995 by Weinstein and Libbrecht [39] and, after many pioneering experiments [40–42], it was successfully realized in 1999 by Reichel, Hänsel, and Hänsch [43]. The advantages of working with an atom-chip are several. The first that immediately comes to mind is that large magnetic field gradients and curvatures can be generated in close proximity to the chip surface by means of modest electric currents. The power dissipation is also lower respect to that produced by macroscopic coils. Another benefit is that the lithographic techniques, used to fabricate the chip, make it possible to integrate many complex systems all directly on a single chip, like several microscopic traps with different geometries, wave-guides and also other atom-optical devices. Of particular interest to us, is the greatly simplified way that such micro-traps allows in achieving Bose-Einstein condensation. Indeed, micro-structured conductors can be exploited in the last stage of evaporative cooling allowing the formation of a condensate in a time shorter than a factor of 10 compared to typical experiments [44]. The higher atomic densities and thus elastic collisions, reachable in such configurations, indeed, result in a faster thermalization that makes possible to drastically shorten the time of RF evaporative cooling. The tight trap permits fast adiabatic changes of the confining potential, thus yielding an easier magnetic compression of the atomic cloud. Furthermore, despite the pull of gravity, the magnetic tight confinement permits to trap the atoms very close to the magnetic trap center resulting in a rather uniform evaporation. The cooling cycle becomes so fast that the collisions with background gas atoms are less important and the stringent vacuum condition can be also relaxed. The overall experimental cycle in reaching BEC can be as short as a few seconds (typically of the order of 10 s), thus benefiting atomic physics experiments.

Another important aspect of atom-chips is that they make possible a coherent manipulation of the internal states of the confined atoms due to the versatility of the lithographic wire structures. Elaborated potentials, with complex structures, in fact, can be designed and tailored to the specific purpose.

Although the robustness, the simplicity of the setup and the possibilities of chip-based potential, the ultimate limit of an atom-chip is the atom-wire distance. In order to feel the near-field potential, indeed, the atomic cloud must be very close to the chip surface. However, this proximity can trigger atom-surface interactions and thus decoherence [45, 46], principally due to the magnetic noise originating from the surface of the atom-chip. A lower limit is therefore set for the distance d of the atoms from the chip surface and this, in turn, limits the timescale of the fully controlled dynamics. The atoms-wire distance d , indeed, has to be small compared to the desired features of the potential, let's say, of size l . Thus the timescale is also limited being $t \sim h/E \sim ml^2/h$, where $E \sim h^2/ml^2$ is the kinetic energy of atoms of mass m localized on the scale l [47]. Besides, as extensively studied and demonstrated, with a proper choice of surface material and fabrication techniques, it is possible to trap atoms at distances of a few hundreds nanometers [48] as well as preserving quantum coherence [49, 50].

2.1.1 Wire traps principles

A simple straight wire contains all the main concepts necessary to realize an atom-chip. Consider an infinitely straight wire carrying a current I . The magnetic field induced is radial. Assuming that the wire is along the x -axis, the magnetic field magnitude, gradient and curvature at distance z from the wire is:

$$\begin{aligned} B(z) &= \frac{\mu_0 I}{2\pi z}, \\ B'(z) &= -\frac{\mu_0 I}{2\pi z^2}, \\ B''(z) &= \frac{\mu_0 I}{4\pi z^3}, \end{aligned} \tag{2.1}$$

respectively. The field of this single wire is not useful for trapping, since there is no local minimum. However, superimposing a homogeneous magnetic field B_{bias} oriented along the y -axis and perpendicular to the wire, the field cancels, creating a line of zero field parallel to the wire on the z -axis at a distance $z_0 = \mu_0 I / 2\pi B_{bias}$ (see Fig. 2.1). Assuming that the current flows in the negative direction ($I < 0$), we can write the vectorial components of the magnetic field plus the bias field

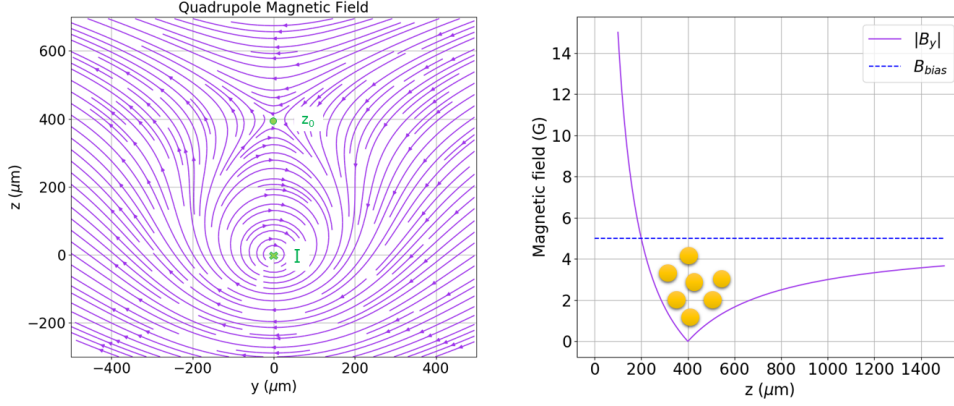


Figure 2.1: *Magnetic guide*. The combination of a wire and an external bias field B_{bias} creates a two-dimensional trapping field called *magnetic guide*. On the left-hand side the resultant magnetic field lines are reported. On the right-hand side the field magnitude $|B_y(z)|$ at $y = 0$. Both figures are realized for a wire current $I = -1$ A and a bias field $B_{bias} = -5$ G. Figure adapted from Ref. [51].

as:

$$\begin{aligned}
 B_x &= 0, \\
 B_y &= B_{bias} - \frac{\mu_0 I}{2\pi} \frac{z}{y^2 + z^2}, \\
 B_z &= \frac{\mu_0 I}{2\pi} \frac{y}{y^2 + z^2}.
 \end{aligned} \tag{2.2}$$

Therefore, the external bias field determines the zero-field point and its magnitude determines the distance between the trap center and the wire.

In the wire proximity ($y = 0$ and $z = z_0$), expression (2.2) can be linearly expanded to see that both requirements $\nabla \cdot \mathbf{B} = 0$ and $\nabla \times \mathbf{B} = 0$ are fulfilled. Moreover, the field behaves as a two-dimensional quadrupole field with constant gradient along any direction from the zero-point $|B'(0, z_0)| = \mu_0 |I| / 2\pi z_0^2$.

Since there is no field dependence on x in Eq. (2.2), the wire-trap is only radial, also called *magnetic guide*, as it confines atoms in the plane perpendicular to the wire and allows their transportation along the wire direction itself. This configuration does not provide axial confinement, necessary for a three-dimensional trap. To confine the atoms in all directions can be easily done by bending the wire ends, *end-caps*, obtaining a wire with a finite length or adding additional crossing wires. Various geometries can be used, but in the following we will describe the ones used in our experiment and obtained by bending the wire ends

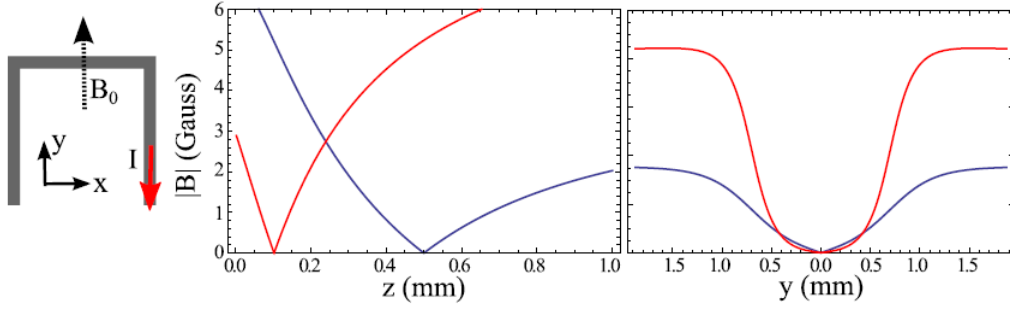


Figure 2.2: *Quadrupole U-trap.* Wire layout in the plane $z = 0$ for a Quadrupole U-trap and magnetic potentials generated for $I = 1$ A. The bias field B_0 along y is set to have a trap at positions $z_0 = 0.5$ mm (red line) or $z_0 = 0.1$ mm (blue line). Note that in order to prevent atom losses due to Majorana spin-flips, described in Subsec. 1.2.2, a longitudinal magnetic field parallel to the wire is added (not shown). The latter, combined with the bias field, effectively rotates the trap axis avoiding Majorana transitions but still leaving the position z_0 as a minimum for the magnetic field. The potentials shown in the figure were obtained by numerical Biot-Savart law integration, taking into account a wire width of $125 \mu\text{m}$. Figure from Ref. [52].

at right angles to form a “U” or a “Z”. In both cases, the central part of the wire combined with the bias field forms a two-dimensional quadrupole for transverse confinement, while the bent wire parts provide the axial confinement.

2.1.2 Quadrupole U-trap

A U-bent wire can be realized by “closing” the guide formed by a straight wire directed along the x -axis and the external bias field $B_{bias} = B_0$ oriented along y , as in Fig. 2.2. This wire configuration induces a 3-D quadrupole trap. Assuming that the contribution of the lateral branches of the wire does not affect the 2-D quadrupole potential provided by the central part of the wire, we will consider the $y = 0$ and $z = z_0$ position of the minimum as fixed. Introducing the parameter $R = z_0/L$, where the central part of the wire along x -axis is of length L , we can calculate the magnetic field produced by each branch. The total field \mathbf{B}^{Ubr} components, linearly approximated around x/L and obtained summing up the two branches contributions, are:

$$\begin{aligned} B_x^{Ubr} &= \frac{\mu_0 I}{4\pi L^2} 4Rx, \\ B_y^{Ubr} &= 0, \\ B_z^{Ubr} &= -\frac{\mu_0 I}{4\pi L^2} (R^2 + 1)L. \end{aligned} \tag{2.3}$$

Note that, since we are moving along the $y = 0$, $z = z_0$ line, the only variable is x . As for the simple wire guide, also here the constant component of the field

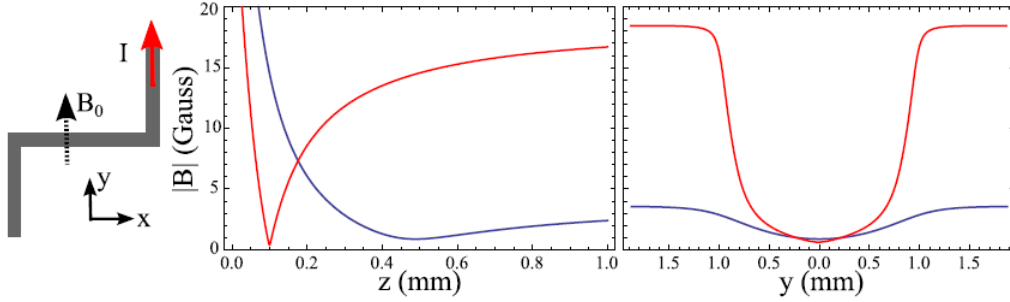


Figure 2.3: *Ioffe-Pritchard Z-trap*. Wire layout in the plane $z = 0$ for a Ioffe-Pritchard Z-trap and magnetic potentials generated for $I = 1$ A. The bias field along y is set to have a trap at positions $z_0 = 0.5$ mm (red line) or $z_0 = 0.1$ mm (blue line). Note that also here, an additional longitudinal magnetic field (not shown) is applied parallel to the wire with the effect of tilting the trap axis, thus avoiding Majorana spin-flips. The potentials shown in the figure were obtained by numerical Biot-Savart law integration, taking into account a wire width of $125 \mu\text{m}$. Figure from Ref. [52].

along z -axis is responsible for a displacement of the trap center along the y -axis. While the total contribution along x -axis is proportional to x and results in a longitudinal field gradient of:

$$|B_x^{Ubr}| = \frac{\mu_0 I}{\pi L^2} R. \quad (2.4)$$

The resulting potential is that of a three-dimensional quadrupole trap, with field zero at $x = 0$, $y > 0$, and $z = z_0$. Therefore, by choosing the correct bias field, the U-trap can substitute the standard quadrupole coil pairs for the production of a MOT [53]. It is noteworthy that the U-quadrupole can be also tilted respect to the planar surface, in order to have the 45° necessary to have a mirror-MOT configuration for the loading of the chip. However it is not the case in our experiment, in which a mirror-MOT configuration is achieved by using traditional tilted coils setup, as we will describe in the following subsections.

2.1.3 Ioffe-Pritchard Z-trap

A U-trap can be transformed into a Z-trap by simply moving a branch of the U-trap to its opposite half-plane, as depicted in Fig. 2.3. Hence, a quadrupole trap on a chip can be easily converted into a Ioffe-Pritchard trap. To calculate the cartesian components field generated by the two branches in a Z configuration, we can follow the same approach used for the U-trap in Subsec. 2.1.2 by simply changing the current direction $I \rightarrow -I$ in one of the two branches. Accordingly, the approximation to the first order of the total field \mathbf{B}^{Zbr} induced by the two

branches is:

$$\begin{aligned} B_x^{Zbr} &= \frac{\mu_0 I}{2\pi L^2} (1 + R^2) LR, \\ B_y^{Zbr} &= 0, \\ B_z^{Zbr} &= \frac{\mu_0 I}{2\pi L^2} (R^2 - 1)x. \end{aligned} \tag{2.5}$$

Now it is the field along the z -axis that has a dependence on x , the displacement along y -axis of the trap center is variable. Whilst the x component of the field is constant. This feature is of great importance in preventing the vanishing of the trap field and thus avoiding the losses due to Majorana spin-flips. Note that the above results are valid only in the restricted range $w < z_0 \ll L$, where w is the wire width. The overall effect is a three-dimensional Ioffe-Pritchard trap whose axial confinement is provided by the curvature $\partial^2 B / \partial x^2$.

The Z-wire trap allows efficient evaporative cooling. It is harmonic near its minimum and has a strong confinement by a nearly linear gradient further away from the wire. This wire geometry is actually used in our experiment to trap the BEC, as explained in the following.

2.2 The experimental setup

In this section we report the path, realized in our laboratory, in reaching always cooler temperatures and higher densities from a Rb vapor as far as the final goal of its condensation in the state $|F = 2, m_F = +2\rangle$ (see Fig. A.1). The latter, indeed, has the strongest interaction with the magnetic field and will be, therefore, the most strongly trapped state.

The section is structured as follows. A first overview on the atom-chip technical details are presented. Then a description of the entire experimental apparatus and the required lasers are discussed. Finally, a step by step analysis of our procedure in realizing a Bose-Einstein condensate together with the imaging technique, used to measure it, are reported. This experiment is the result of the work and efforts of many previous members of the atom-chip group. An extensive and exhaustive dissertation is given in Ref. [52].

2.2.1 The atom-chip layout

The atom-chip is the hearth of our experiment. The BEC forms a few hundred microns in proximity of its surface and the condensate's internal state dynamics manipulation is performed by means of it. It was fabricated by the Quantum Optics group of the University of Vienna by standard micro-fabrication technology. It consists in a silicon surface on top of which is evaporated a gold layer

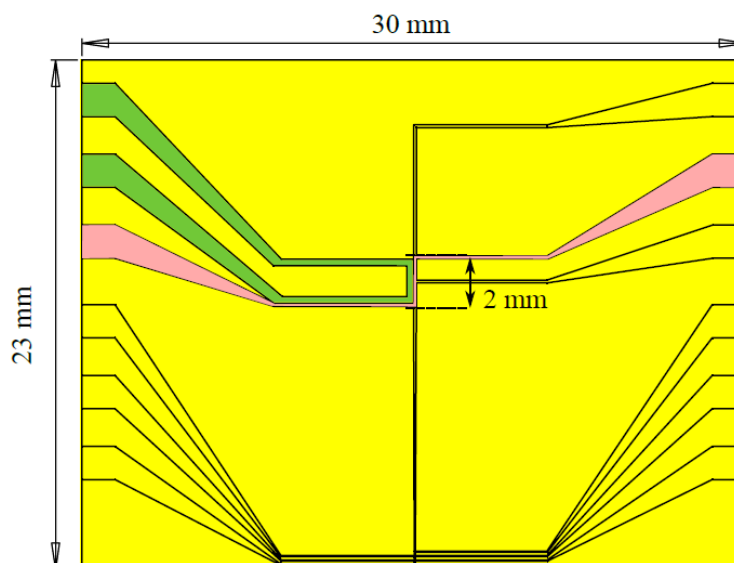


Figure 2.4: *The atom-chip layout.* Dimensions and wires layout of the atom-chip golden frontside used in our experiment. Enhanced in pink is the small- z wire that realizes the Ioffe-Pritchard trap in which the BEC is produced in the final cycle. Enhanced in green, the u-wire used to manipulate the BEC internal atomic states. These are the main structures of the chip, the other ones can be switched on to implement ulterior manipulations depending on the experiment. However, we will not consider them any further because they have not been tested yet.

by photo-lithography. The wires on the surface are obtained by opportunely removing gold portions in such a way to shape the appropriate structures. They are of several widths (50 , 125 and $300\mu\text{m}$), have a height of $2\mu\text{m}$ and are defined by $10\mu\text{m}$ -wide gaps. The overall chip surface is covered by a high-quality gold layer with a substrate smoothness made by grains of a size lower than 50nm . This guarantee the high reflectivity necessary to realize an integrated mirror-MOT, a variant of the standard magneto-optical trap to cool and trap the atoms that will be described in Subsec. 2.2.2. High-quality wires are essential too in order to avoid uncontrolled deviations of the current flow and as a consequence disorder in the trapping potential [54, 55]. A schematic of the chip layout is reported in Fig. 2.4. Placed at the center of the chip, there is a z -wire (enhanced in pink and which we will refer to as *small- z*) that generates the Ioffe-Pritchard potential at the final stage of our experimental cycle in which the BEC is produced. The central part of the small- z is 2mm long while its arms are 6mm long. The width of this wire is $125\mu\text{m}$ and has a resulting resistance of 1.63Ω . For a bias field of 15G , the trap frequencies induced in the center of the Ioffe-Pritchard small- z trap are $\omega_{axial} = 2\pi \times 76\text{Hz}$ and $\omega_{radial} = 2\pi \times 975\text{Hz}$.

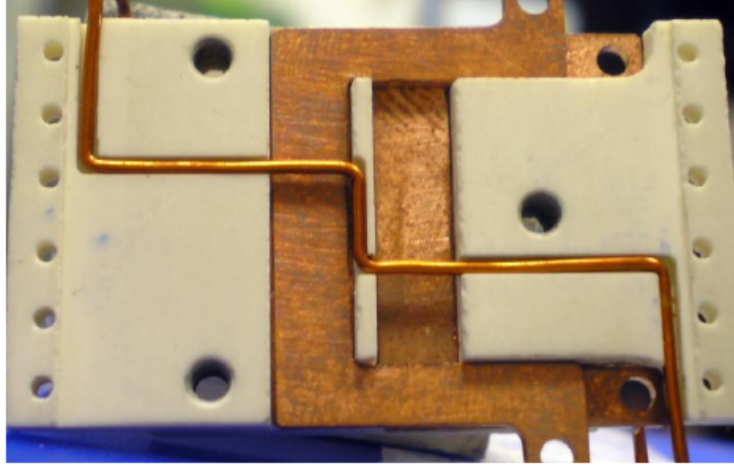


Figure 2.5: *Backside of the atom-chip.* A ceramic white block sustains the macroscopic Z-wire (big-Z) and two U-shaped conductors. The big-Z is used to facilitate the transfer of the atoms into the on-chip small-z trap. While the closest U-conductor to the chip carries the RF signal used for evaporative cooling.

Enhanced in green, is a u-wire exploited to manipulate the BEC internal atomic states (Fig. A.1), as we will clear later in Sec. 2.3. The width of this wire is of $300\ \mu\text{m}$ and it has a resistance $R = 0.8 - 0.9\ \Omega$. Applying to it a voltage signal $V(t) = A \cos(\omega_{RF}t)$, a current $I(t) = RV(t)$ is generated. Since the distance at which the BEC forms, with respect to the chip surface where the u-wire holds, is $d = 190\ \mu\text{m}$ and the signal frequency ω_{RF} of the radio-frequency field produced by it does not exceed a few tenth of MHz, the electromagnetic field induced by $I(t)$ is a near-field. Hence it can be approximated to the field generated by an infinitely long wire and the atoms will be affected by a magnetic field varying in time as:

$$\begin{aligned} B(t) &= \frac{\mu_0 R}{2\pi d} V(t), \\ &= A \frac{\mu_0 R}{2\pi d} \cos(\omega_{RF}t). \end{aligned} \quad (2.6)$$

This field can efficiently couple the internal m_F states of the atomic hyperfine structure, hence providing a suitable tool for state manipulation.

In Fig. 2.5 the backside of the atom-chip is shown. The ceramic white block sustains and isolates other different conductors placed behind the chip. On the rear side of the white block, in turn, a mini-heater and a thermocouple are glued. Indeed, while the experiment is not running, the microchip mount is heated to 40°C to make the rubidium atoms detach from its surface and cleaning it, thus preventing atom-desorbing during the experimental cycle and their consequent detrimental effect on the trap lifetime. Since the atom-chip is placed in a ultra-

high-vacuum (UHV) science cell, both the mini-heater (343-HEATER-2×10, controlled by an external regulator) and the thermocouple placed near to it, have to be UHV compatible.

As shown in Fig. 2.5, the ceramic white block holds two U-shaped conductors and a macroscopic Z-wire (named *big-Z*). The U-shaped conductors are made of copper and have a section of 1.5 mm high and 2 mm wide, while the whole width is 16 mm. They are placed in two different planes. The upper U structure has a length of 9 mm and is just below the mirror, the lower one has a length of 11 mm and lays just below the upper one. We can independently drive them with two remotely controlled power supplies and they are electrically isolated by a 0.125 mm thick kapton foil (KAP10). The U-conductor closer to the mirror is actually used to generate the radio-frequency signal that drives evaporative cooling of our rubidium atomic cloud.

The big-Z wire is made of copper and insulated with kapton, its cross-section is of 0.61 mm and 0.87 mm. The big dimension of the wire allows to work with higher currents providing a Ioffe-Pritchard trap of larger volume. In this case the minimum of the trap, indeed, falls further away from the chip surface. This trap is useful to transfer the atoms, previously cooled in a molasses, to the on-chip magnetic trap made by the small-z. This microscopic trap, in fact, has a small capturing volume respect to the typical dimensions of a molasses that are of $x \times y \times z = 1.5 \times 1.5 \times 3 \text{ mm}^3$. The transfer is realized by keeping the external field constant and decreasing the big-Z current so that the trap position moves closer to the chip surface, until the trapping potential of the small-z on the chip can be turned on.

2.2.2 Apparatus and Mirror-MOT

Any experiment that deals with ultra-cold atoms requires to isolate them from the environment. Indeed, collisions of the trapped atoms with the ones from the residual gas, ultimately limits the magnetic trap lifetime. The latter needs to be of the same order of magnitude of the BEC cycle time, that for an experiment like ours realized with a chip-setup is of a few seconds. In our laboratory the isolation is realized by means of a vacuum system composed by an Ion pump (Varian VacIon Plus StarCell 150, 125 l/s, controlled by a Varian Duel controller) and a Ti-sublimation pump. They provide an Ultra-High-Vacuum (UHV) pressure of 2×10^{-10} mbar in the science cell. All the system is supported by the flange of the ionic pump to which the science cell is attached and suspended 18 cm above the optical table (as you can see in Fig. 2.6). The science chamber is a rectangular glass made of Vycor, 100 mm long, 40 mm wide and 40 mm deep. Its transparent feature allows full optical access. The chip is placed in the middle of the cell, with the gold side facing down as shown in the picture. Its support, electrical connec-

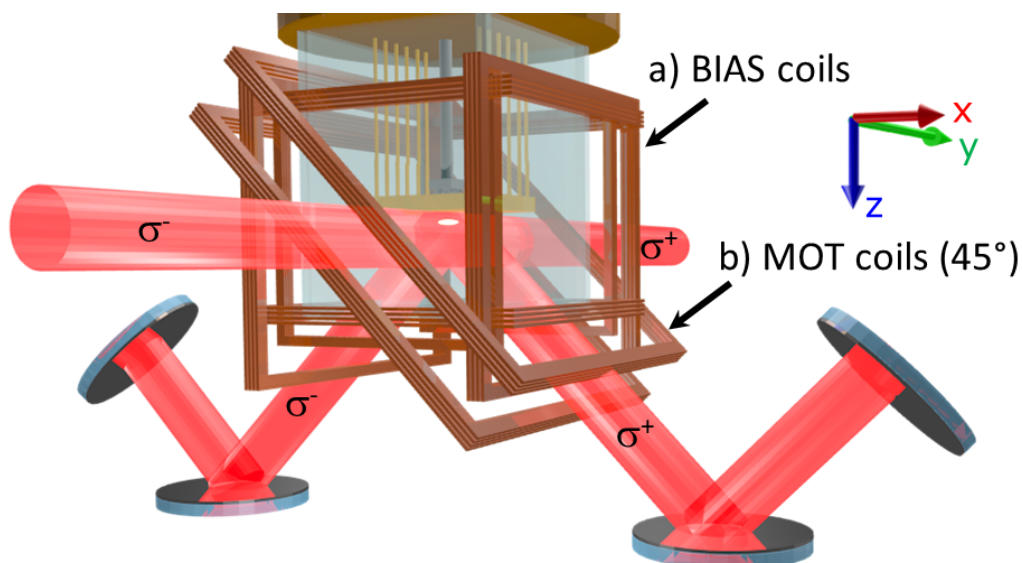


Figure 2.6: *Mirror-MOT*. 3D vision of our mirror-MOT coil suits and laser beams. The vacuum science cell, with the atom-chip mounted inside with its golden side facing down, is placed at the center of the coils. The four MOT beams with the required circular polarizations are represented: two straight beams propagate in opposite directions parallel to the chip surface, the other two beams are reflected on two mirrors placed on the optical table and impinges at 45° on the chip surface. The latter beams, reflecting on the golden chip surface, provides the last two MOT-beams for a total of six. The magnetic coils suit indicated by (a) are the ones that generates the bias fields, while the ones indicated by (b) are parallel to the 45° beams and produce the magnetic field for the MOT. For illustrative purposes, an atomic cloud is drawn near the chip surface at the beam crossing.

tions and the dispensers occupy the upper part of the cell held by the flange. Several magnetic coils surrounds the science chamber in order to generate the magnetic fields used in the different stages of the cooling and trapping cycle. Three pairs of Helmholtz coils, two for each direction, provide the homogeneous magnetic bias fields (B_x , B_y , B_z) used to manipulate the atoms and compensate external environmental magnetic fields (coils (a) in Fig. 2.6). The 45° -tilted pair (coils (b) in Fig. 2.6), instead, are the anti-Helmholtz coils used to generate the quadrupole field of the MOT stage.

In our experiment we use a variant of the standard magneto-optical trap to cool and trap the atoms: the *mirror-MOT*. This configuration, inevitable when one wants to cool atoms that are near a surface, is shown in Fig. 2.6. It exploits the mirror surface of the chip to reflect two of the usual six counter-propagating MOT beams to realize the same cooling with just four beams. Two are counter propagating and aligned along the y direction, parallel to the chip surface, with opposite polarization σ^+ and σ^- . The other two impinge on the chip at 45° from

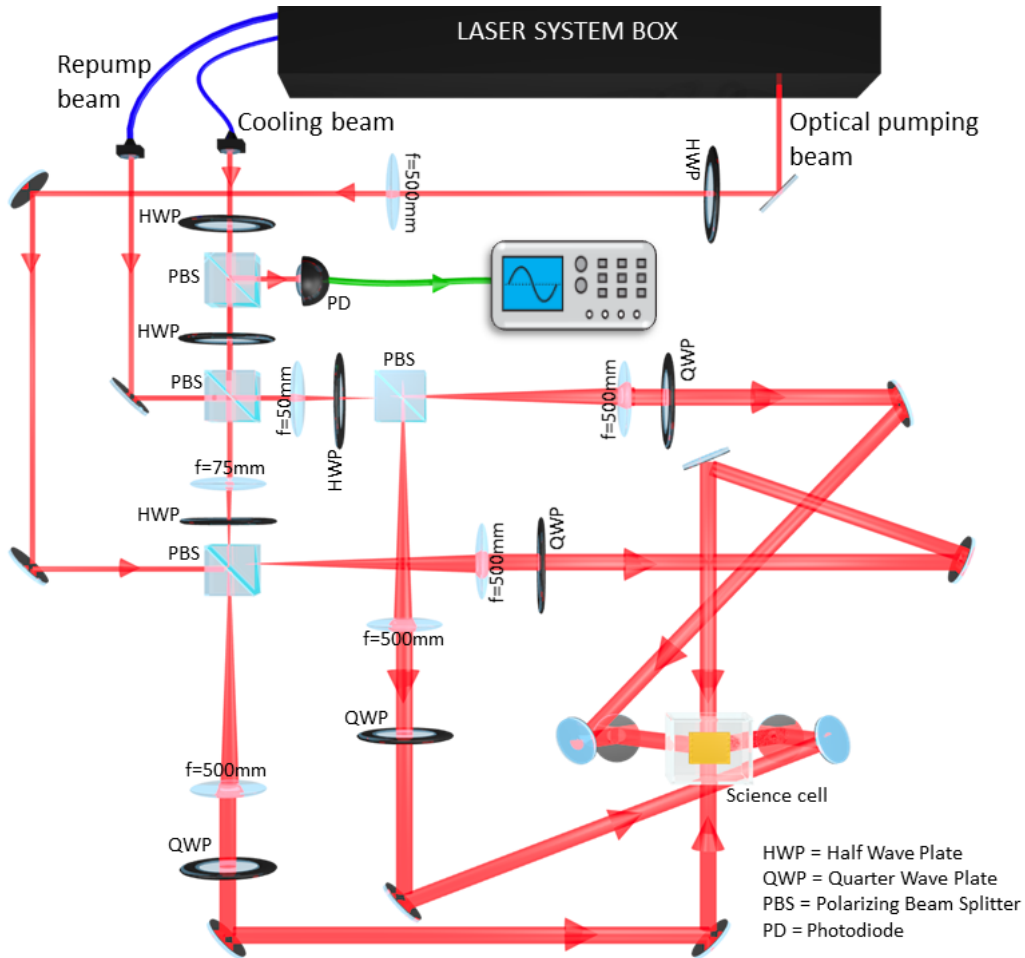


Figure 2.7: *Mirror MOT optical setup.* Schematic of the laser beams necessary to cool the atomic gas in a mirror-MOT. We show how the cooling light divides into the four mirror-MOT beams and mixes once with the repump beam, to enhance the MOT efficiency, and then with the optical pumping beam to prepare the atoms in the final magnetically trapped state $|F = 2, m_F = +2\rangle$ that will be the initial state of all our experiments described in chapter 3 and 4.

opposite directions and lay in the xz -plane. In this way the usual MOT geometry is realized in the half space delimited by the chip reflecting surface. The MOT coils (b) are tilted in order to be parallel to those beams and creating a minimum of the magnetic field in the region where the four MOT beams overlap at 7 mm from the chip surface.

Our mirror-MOT optical setup is schematized in Fig. 2.7. Inside the laser system black box, all the necessary beams are prepared (as described in detail in Subsec. 2.2.3). Before splitting into the four beams required for the mirror-MOT, a small portion of the master laser, used for cooling, is withdrawn and detected by a

photodiode in order to adjust possible noise. A half-wave-plate (HWP) and a polarizing beamsplitter (PBS) subsequently divide the cooling light into two beams: one, after passing through another PBS, realizes the two counter-propagating and parallel to the chip MOT-beams and similarly the other realizes the two tilted MOT-beams at 45° . Thus, after being split into the four MOT-beams, two pair of lenses in a telescope configuration enlarge the beams' size to an e^{-2} diameter of 30 mm in order to exploit all the chip surface. Four quarter-wave-plates (QWP) circularly polarize each of the four beams according to the MOT scheme. During the first loading phase, the frequency of the laser is red detuned -3Γ (-18 MHz, where $\Gamma = 2\pi \times 6$ MHz is the natural linewidth of the rubidium D2-line transition) from the transition $F = 2 \rightarrow F' = 3$ (see Rubidium D2-line scheme in Fig. A.1). The power of the cooling beam is 200 mW and the first polarizing beam-splitter sends a portion of it of $1/3$ to the straight beam pairs, while a portion of it of $2/3$ to the tilted beam pairs.

Even though the chosen transition for the MOT $F = 2 \rightarrow F' = 3$ is a closed transition, the probability of the atoms falling in the $F = 1$ state is non zero given that the laser frequency is slightly detuned from resonance and thus not far from the state $F' = 2$. This is sufficient to lose the MOT trapping requirements explained in Subsec. 1.2.3. In order to prevent this loss and to enhance the MOT efficiency, a second laser, resonant with the transition $F = 1 \rightarrow F' = 2$, is implemented thus repumping the lost atoms in the $F = 2$ ground state. It has a total power of 5 mW after the fiber and is mixed with the cooling light in the first polarizing beam-splitter.

Finally, to maximize the transfer of atoms into the magnetic trap, another beam, that pumps them into the desired low field seeking state $|F = 2, m_F = +2\rangle$, is exploited. It is indicated as optical pumping beam and, in order to fulfill this purpose, is resonant with the $F = 2 \rightarrow F' = 2$ transition. It is mixed in the second polarizing beamsplitter with the straight MOT-beams and is aligned such that impinges on the atomic cloud at a distance from the chip surface where the on-chip magnetic trap center forms.

2.2.3 Laser system

It is clear till now that, for our experiment to work, several laser lights at different frequencies are required. We can summarize all of them as: cooling laser, repump laser, optical pumping laser and imaging laser. A schematic of the exploited ^{87}Rb hyperfine structure of the ground $5^2S_{1/2}$ and excited $5^2P_{3/2}$ states of the D2-line transition, is depicted in Fig. 2.8 and reports all the frequencies used during our experiment. These frequencies are provided by two distributed feedback lasers (DFB) placed inside a black box on our optical table and connected to the outside by polarization maintaining optical fibers, except for the optical pumping beam

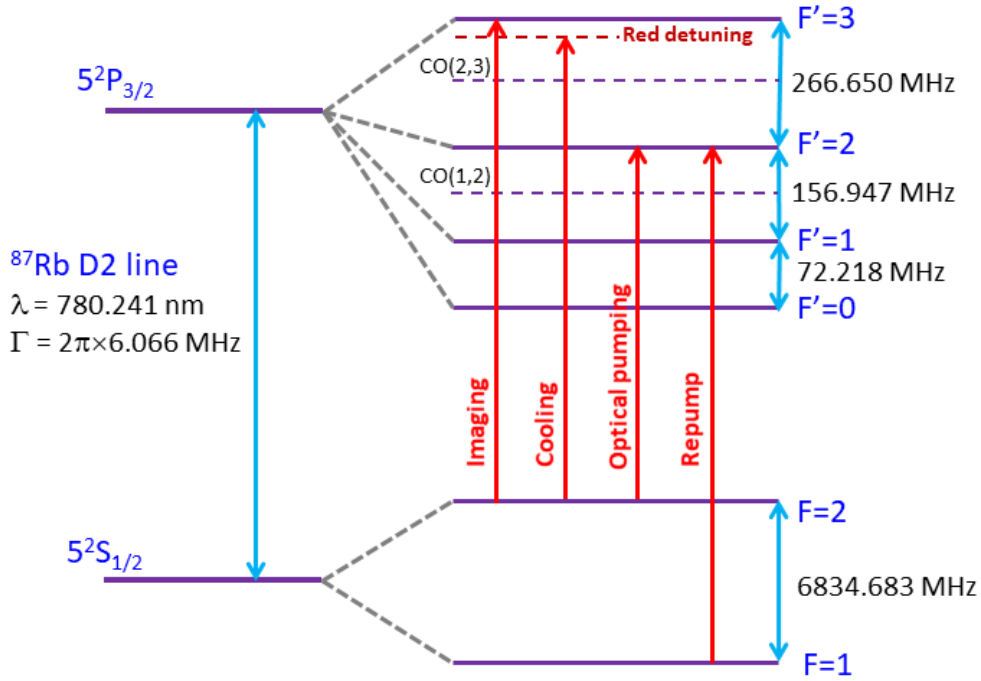


Figure 2.8: ^{87}Rb D2-line and laser frequencies. Hyperfine structure of the $5^2S_{1/2}$ and $5^2P_{3/2}$ states of the ^{87}Rb D2-line transition is shown. Red arrows are the laser frequencies required by our experiment, while light-blue arrows indicate the spacing between the levels reported in MHz [57].

that exits in free space from a hole in the box (as shown in Fig. 2.7). One DFB laser (the master) provides lights for the MOT cooling, the optical pumping and the absorption imaging. While the second DFB laser provides the light for the repumping.

The **DFB master laser** is locked on the crossover transition $F = 2 \rightarrow F' =$ CO(2, 3) (a smooth transition between the two separate ones $F = 2 \rightarrow F' = 2$ and $F = 2 \rightarrow F' = 3$) by a frequency-modulated (FM) spectroscopy. According to Fig. 2.9, we can see that after passing through an optical isolator and an anamorphic prism, the light is divided into two beams one is sent to a tapered amplifier (TA) and another to the double-pass AOM-1 (Acusto Optic Modulator). The latter shifts the laser frequency in order to be close to the $F = 2 \rightarrow F' = 3$ transition necessary for the MOT cooling stage. From the output of AOM-1, a small portion of light ~ 1 mW is used for the FM-spectroscopy and ~ 4 mW is sent to another double-pass AOM-4 to get the **optical pumping light**. AOM-4 shifts the light frequency to the $F = 2 \rightarrow F' = 2$ transition necessary to prepare the atoms in the final low field seeking state $|F = 2, m_F = +2\rangle$. This light is then mixed in a polarizing beamsplitter (PBS) with a portion of the repump laser (resonant with

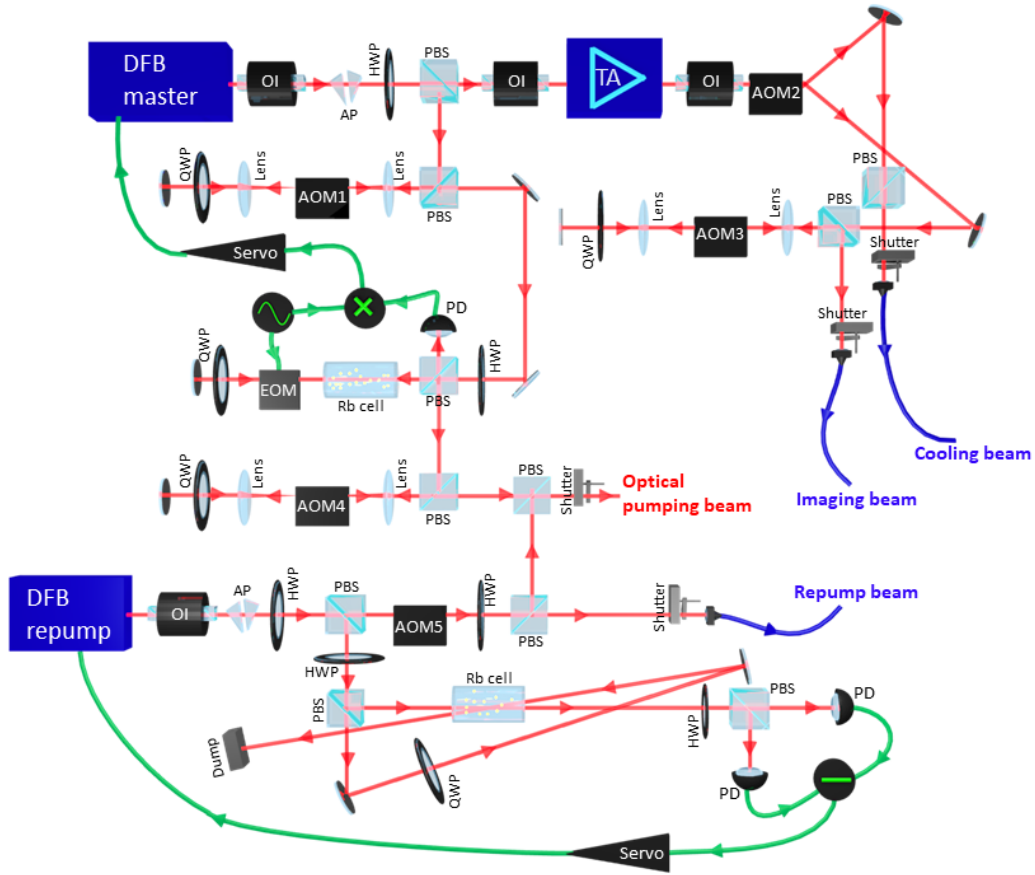


Figure 2.9: *Laser system.* Schematic of the DFB master and DFB repump lasers that provides all the necessary frequencies for the experiment. The master generates lights for: cooling, imaging and optical pumping stages. While the DFB repump laser produces the repumping light only. We use the following abbreviations to indicate: AOM, acousto-optic modulator; AP, anamorphic prism; EOM, electro-optic modulator; HWP, half waveplate; OI, optical isolator; PBS, polarizing beamsplitter; PD, photodiode; QWP, quarter waveplate; TA, tapered amplifier.

the $F = 1 \rightarrow F' = 2$ transition) in order to improve the pumping efficiency. The part of the beam that goes to the TA, instead, is amplified up to 850 mW. This amplification, indeed, is required for the collection of a large number of atoms in the first cooling stage realized by the MOT. Such amplified beam is then sent to a single-pass AOM-2 that shifts its frequency setting the desired red detuning from resonance necessary during the MOT and optical molasses stages. Its negative first diffraction order is sent to a PBS and coupled to an optical fiber to go out of the box and realize the **cooling light**. Since the TA produces a great power, we can exploit also the ~ 15 mW coming from the first positive diffraction order of the AOM-2 to realize the **imaging light**. This beam is sent to another double-pass AOM-3 that shifts down its frequency in order to be resonant with

BEC total preparation time (8 s)							
Steps	Mirror-MOT	CMOT	Molasses	Optical pumping	Big-Z trap	Small-z trap	Evaporative cooling
Duration (ms)	5000	14	3.5	0.3	250	250	2500

Figure 2.10: Time-line of the BEC production program.

the $F = 2 \rightarrow F' = 3$ transition and then to go to an optical fiber out of the box. The **second DFB laser** is used only for the **rempump light**. A small part of this beam is sent to a spectroscopy cell in order to stabilize, by means of polarization spectroscopy, the laser frequency on the crossover resonance $F = 1 \rightarrow F' = CO(1, 2)$. The other part of the beam is sent to the single-pass AOM-5 shifting the frequency in order to be resonant with the desired transition $F = 1 \rightarrow F' = 2$. The beam is then divided by a PBS into two parts. The first is mixed, as already explained, with the optical pumping beam. The second is coupled into an optical fiber and directed out of the box to be mixed with the MOT beams. Finally, several mechanical shutters are mounted along each laser's path in order to control the timing of the laser light. Together with the AOMs, they switch the lasers on and off when necessary during the entire experimental cycle.

2.2.4 Steps towards BEC on the atom-chip

The experimental cycle to produce a Bose-Einstein condensate in our laboratory has a duration of 8 s. A summary of our BEC production program time-line is shown in Fig. 2.10. Let us analyze it step by step.

- **Mirror MOT.** At the beginning of the cycle, a 2 s long pulse at 7 A activates the injection of the rubidium vapor gas from a pulsed-dispenser placed behind the chip to the science cell. As they escape from the dispenser, the rubidium atoms have an initial phase-space density of $\Phi \simeq 10^{-25}$ at an evaporation temperature of $\sim 700^\circ\text{C}$. Together with the activation of the dispenser, the mirror-MOT stage (described in Subsec. 2.2.2) is started thus allowing the loading of a large pre-cooled number of atoms at 7 mm from the chip surface. Here the atom number is maximum and they will need to be subsequently shifted and transferred into the on-chip magnetic trap which is effective only in the small range of typically < 3 mm from the chip surface. During this stage the peak atom number is obtained with a light detuning $\Delta = -18$ MHz (-3Γ) from the rubidium D2-line transition, a beam intensity of 35 mW cm $^{-2}$ and a quadrupole gradient of 15 G cm $^{-1}$. After 5 s of loading we obtain:

$$N = 7 \times 10^8 \text{ atoms};$$

$$T = 120 \mu\text{K};$$

$$\Phi = 8.5 \times 10^{-8}.$$

- **CMOT.** The spatial extent of the MOT cloud, reached in the previous step, is too big to be transferred to the magnetic trap made by the small- z wire on the chip surface. For an optimum loading of the magnetic trap it is important to reduce the spatial extent of the MOT. This is the intent of the Compressed-MOT (CMOT) stage. This stage has to be performed in close proximity of the chip surface where the magnetic on-chip trap will be turned on. Therefore, a transfer of the atoms from the distance of 7 mm to 2 mm from the chip is realized first. The position of the MOT center is displaced applying an appropriate homogeneous magnetic field made by the bias- x and bias- z currents flowing in the bias coils. To implement this movement, these fields are linearly ramped in 450 ms. At this point, the compression can start. The CMOT differs from the MOT in the increased red detuning of the trapping laser (from -3Γ to -14Γ), decreased power of cooling light (80% reduction) and greatly reduced repumping laser power (from 5 mW to 50 μW). The change in the frequency locking of the cooling laser is compensated in its FM-spectroscopy by a frequency jump lock. The CMOT effect is to reduce the radiation pressure thus creating a denser cloud. Indeed, reducing the detuning of the trapping laser decreases the scattering rate and as a consequence the possibility of the radiated photons to be re-absorbed from the neighboring atoms thus risking a repulsive undesired effect. The entire CMOT stage lasts about 14 ms, after which we obtain:

$$N = 7 \times 10^7 \text{ atoms};$$

$$T = 25 \mu\text{K};$$

$$\Phi = 8.5 \times 10^{-7}.$$

- **Molasses.** A short optical molasses is performed at the end of the compression stage. The quadrupole field is turned off and the bias magnetic field is adjusted in order to compensate spurious magnetic fields coming from the environment. In this regard the cloud is released to expand freely and homogeneously in all directions. Here we can take a first “photograph” of the cloud thanks to which we can balance the laser beams in order to have the correct compensation of the fields. Indeed, if one direction is not correctly compensated, the cloud tends to move in that direction (as you can see in Fig. 2.11). The optical molasses benefits are great in terms of the reached temperature, which is consistent with sub-Doppler “sisyphus-like” cooling reported in Subsec. 1.1.4. After its 3.5 ms duration we have:

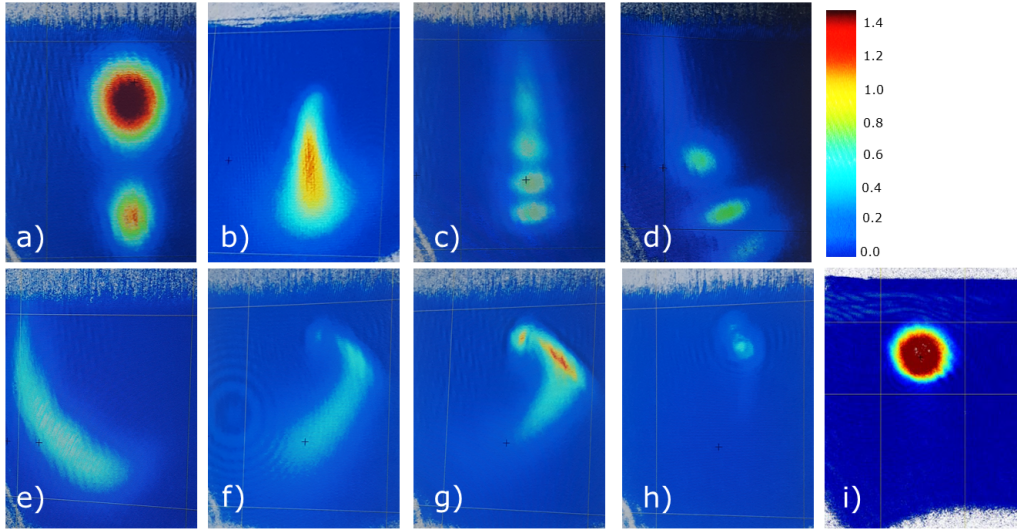


Figure 2.11: *Unbalanced compensation fields effects.* Here are reported several pictures of how the atomic cloud appears when some compensation field of the magnetic trap is unbalanced. At the top side of each image you can notice the chip profile as a gray shade. In these particular cases, the circuit that turns on a compensation field was disconnected (but we didn't know it!). Hence, we were trying to understand the origin of the problem by changing the optical alignment and the values of the compensation fields. The pictures e), f), g) and h) show how a little portion of atoms, when you are reaching the correct balancing, is finally moving towards the trap center! Subfigure i) shows how the magnetically trapped atoms appear with a good compensation of fields and optimal alignment of MOT beams.

$$N = 7 \times 10^7 \text{ atoms};$$

$$T = 10 \mu\text{K};$$

$$\Phi = 4.5 \times 10^{-6}.$$

- **Optical pumping.** At this stage the molasses light are turned off together with the magnetic fields and the optical pumping stage starts lasting for an overall time of $300 \mu\text{s}$. The first $100 \mu\text{s}$ are spent to trigger the y -coils (at 1 G) in order to have the optical pumping beam polarized with a polarization σ^+ with respect to the quantization axis provided by the y -coils themselves. Subsequently the opening of a shutter let the optical pumping beam reach the atomic cloud and interact with it for $150 \mu\text{s}$ and for further $50 \mu\text{s}$ with the repumping light. Hence, the optical pumping light transfer the whole atomic population in the low field seeking state $|F = 2, m_F = +2\rangle$ that is a dark state for the transition $F = 2 \rightarrow F' = 2$ exploited for this purpose. Indeed, this keeps the heating to a minimum during the optical pumping

pulse. However, a small heating of the atomic cloud by means of the optical pumping is observed together with a slight displacement of the cloud in the beam direction. This reveals a non perfectly defined polarization of the light, hence resulting in a not entirely dark state. After this step the characteristics of the atomic cloud become:

$$N = 7 \times 10^7 \text{ atoms};$$

$$T = 13 \mu\text{K};$$

$$\Phi = 3.0 \times 10^{-6}.$$

- **Big-Z magnetic trap.** The atoms are now prepared to be magnetically trapped by the fields generated via the atom-chip. A first field induced by the big-Z wire is needed to transfer the atoms into the on-chip small-z magnetic trap. To do so, a rapidly increasing current I_Z (from zero to a maximum of 25 A), flowing through the big-Z wire behind the chip, is activated. Simultaneously, a bias field along x is set ($B_x = 10.5$ G) in order to position the trap minimum of the resulting confining potential at 2 mm from the chip surface. The bias field along y is also turned on ($B_y = 3$ G) in order to avoid the Majorana spin-flips due to the vanishing field minimum of the big-Z Ioffe-Pritchard trap. The total time for this transfer procedure is of 250 ms. At this stage it is also possible to take another absorption image of the cloud in order to optimize the optical pumping beam thus maximizing the magnetic trap loading efficiency. Note that absorption imaging is a destructive measurement, therefore, after the optimization is completed, a new cycle have to start from the beginning to reach the final stage of condensation.

The characteristics of the cloud at this point of the cycle are:

$$N = 3 \times 10^7 \text{ atoms};$$

$$T = 15 \mu\text{K};$$

$$\Phi = 4.9 \times 10^{-6}.$$

- **Small-z magnetic trap.** The small-z trap provides the trapping potential in which the final stage of evaporation takes place. The final evaporation cooling requires high collision rates to have a faster atom thermalization. The small-z trap, therefore, must strongly compress the atoms to reach the desired corresponding high densities. The strength of micro-traps resides right in their extreme compressibility. In this regard, the atoms are adiabatically transferred to the small-z potential by linearly ramping its current from zero to 1.7 A in 250 ms, whilst the big-Z current is ramped off. The y bias coils are also ramped down to maintain the residual field at

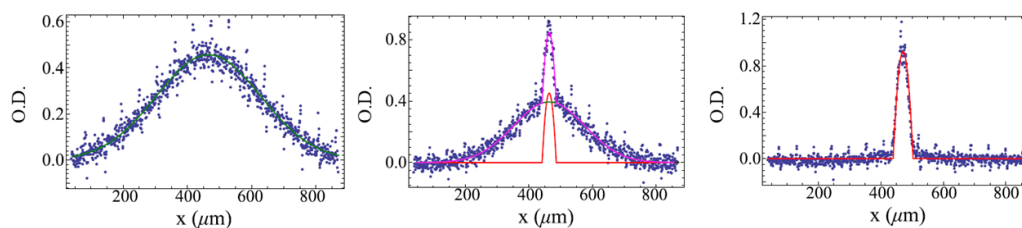


Figure 2.12: *BEC density profile.* From left to right: in the first image we are slightly above the threshold of the BEC phase transition where the density distribution is still Gaussian. In the second one, a sharp parabolic peak of condensed atoms is emerging within a Gaussian profile of non-condensed atoms. In the third image, a Thomas-Fermi distribution of an almost pure condensate has formed. Image and caption adapted from [52].

the trap center. The x bias coils are, instead, ramped up from $B_x = 10.5$ G to $B_x = 15.5$ G. In this trap the atoms are highly compressed and take the typical cigar-shape. At the end of this compression stage, they are $190 \mu\text{m}$ far from the chip center and the cloud temperature undergoes an increase. After 500 ms from the compression phase ending, when rethermalization has taken place, the measured characteristic of the cloud are the following:

$$\begin{aligned} N &= 1.5 \times 10^7 \text{ atoms;} \\ T &= 90 \mu\text{K;} \\ \Phi &= 1.8 \times 10^{-5}. \end{aligned}$$

- **Evaporative cooling.** At this stage, evaporative cooling is achieved applying to the U-shaped conductor, hosted behind the chip, a radio-frequency signal that exponentially sweeps from 22 MHz to 0.7 MHz in 3 s. The signal is provided by a home-made Direct Digital Synthesizer (DDS) adapted to the requirement of the setup and connected to the U-shaped conductor that serves as the antenna. The signal is designed and controlled through a Mathematica[®] program. The RF interaction induces transitions in the m_F atomic sub-levels effectively turning the potential from trapping to anti-trapping. This results in lowering the potential depth and thus reaching the phase transition point. The required parameter values to attain Bose-Einstein condensation are fulfilled and in the case of our experiment are:

$$\begin{aligned} N &= 90 \times 10^3 \text{ atoms;} \\ T &= 480 \text{ nK;} \\ \Phi &> 2.612. \end{aligned}$$

The remaining atoms are finally in a Bose-Einstein condensate in the unique pure quantum state $|F = 2, m_F = +2\rangle$ and are distributed following a Thomas-Fermi

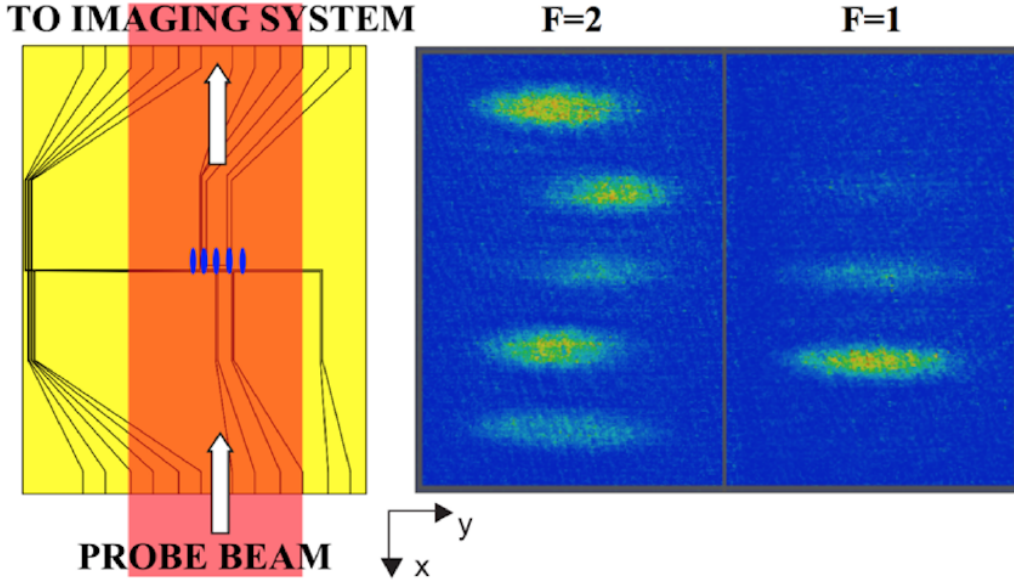


Figure 2.13: *Imaging system.* Left-hand side: View from the top of the probe beam for the imaging of the BEC spatially separated atomic clouds of manifold $F = 2$. The beam is along the \hat{x} direction, perpendicular to the atomic clouds spatial spreading. Right-hand side: Absorption images of the $F = 2$ and $F = 1$ manifolds.

profile (see Fig. 2.12) having an axial dimension of $d_{axial} = 15.5 \mu m$ and a radial dimension of $d_{rad} = 1.26 \mu m$.

2.2.5 Imaging system

Observing a trapped Bose-Einstein condensate is a very difficult task because of its small and optically thick dimensions. That is why we adopt an absorption imaging technique combined with Stern-Gerlach [56] discrimination. At this stage the magnetic fields are switched off, thus letting the atoms fall expanding ballistically for some ms, depending on the experiment. During this time, a weak homogeneous magnetic field, $B_y = 1$ G, realized by a pair of coils oriented along the y -direction (see left side of Fig. 2.13) and in Helmholtz configuration, defines the quantization axis of the system. Moreover, an inhomogeneous magnetic field gradient, lasting 10 ms, is generated by a pair of bias coils in anti-Helmholtz configuration and is applied along the quantization axis. Therefore, atoms in different m_F sub-levels of $F = 1$ and $F = 2$ are subject to the force:

$$F_y = \langle F, m_F | \nabla(\boldsymbol{\mu} \cdot \mathbf{B}) \cdot \hat{y} | F, m_F \rangle = \mu_B g_F m_F \frac{\partial B_y}{\partial y}, \quad (2.7)$$

that spatially separate them. Atoms in the magnetic sub-levels $|m_F = \pm 1, \pm 2\rangle$ are, indeed, deviated in opposite directions, whilst the ones in $|m_F = 0\rangle$ sub-level, having zero angular momentum, are not affected.

Then, after further 13 ms of free expansion, we observe the clouds by shining an imaging laser beam directed along the x -direction, in resonance with the atomic transition $F = 2 \rightarrow F' = 3$ and σ^+ polarized. The absorption of light creates a shadow of the BEC clouds in the imaging beam that is recorded by a CCD camera (see right side of Fig. 2.13). The amount of light absorbed gives the column optical density (OD) along a particular direction through the clouds, from which we extract: position, dimension and density of the atomic cloud. Every experimental result in this thesis work comes from the analysis of images of optical density structures. In more detail, for an imaging beam oriented along x -direction with an intensity profile $I_0(y, z)$ and an atomic cloud of spatial density $n(x, y, z)$, the transmitted beam intensity is:

$$I_t(y, z) = I_0(y, z)e^{-\sigma \int n(x, y, z) dx}, \quad (2.8)$$

where $\sigma = 3\lambda^2/2\pi$ is the resonant absorption cross section and the integral is computed along the observation direction \hat{x} . Through this equation and the images of the probe beam profiles with and without the atomic clouds, we can get the column atom density $\tilde{n}(y, z) = \int n(x, y, z) dx$. Precisely, we exploit also a “dark” image, whose intensity profile is $I_d(y, z)$ and which consists in an image without the atoms and laser both, to avoid offset errors due to spurious light sources. The column atom density becomes:

$$\tilde{n}(y, z) = \int n(x, y, z) dx = -\frac{1}{\sigma} \ln \left(\frac{I_t - I_d}{I_0 - I_d} \right). \quad (2.9)$$

The image containing the sample of atoms gives us information on the absorption $I_t(y, z)$, the image without the atoms on the incident light $I_0(y, z)$ and the dark image on $I_d(y, z)$.

We can summarize our imaging sequence as follows:

- The imaging beam resonant with the $F = 2 \rightarrow F' = 3$ transition shines on the spatially separated clouds for $25 \mu s$, taking an image on the CCD camera of the five atomic clouds of the $F = 2$ manifold (see right side of Fig. 2.13);
- After 1 ms from the first image, the imaging beam and repumping beam are simultaneously switched on for $25 \mu s$ thus taking an image of the three atomic clouds of the $F = 1$ manifold (again see right side of Fig. 2.13);

- After the imaging beam has blown away all the atoms from the trap, the previous two steps are repeated in order to have an image of both manifolds but without any atoms;
- A final image of the dark background alone without any light is then taken.

The overall free falling time during the imaging sequence is thus of 24 ms. Finally, the program on which we analyze the collected images permits to extract all the necessary information by manually selecting the region of the absorption spot.

Note that absorption imaging is a destructive measurement during which the atoms accumulate enough recoil to be blown away from the condensate state. Therefore, every time you need to repeat a measurement, a new cycle (as described in Subsec. 2.2.4) has to be performed to produce a new BEC. In order to prepare the system to start a new cycle, after the imaging sequence, further 15 s are required to recover the vacuum optimal conditions. The overall duration of an experimental cycle is thus 23 s.

2.3 Manipulating the BEC internal states

The quantum protocols developed in this thesis work, require the manipulation of the internal state dynamics of our condensate. This is achieved exploiting the rubidium hyperfine structure letting it interact with radio-frequency and microwave fields, as shown in Fig. 2.14. The radio-frequency interaction drives the coherent evolution among the $|m_F\rangle$ sub-levels of the same manifold, while the micro-wave driving allows to jump from a manifold $F = 1$ to another $F = 2$. The resulting population distribution among them, at the end of the evolution, is measured via the imaging system as described in Subsec. 2.2.5. Since the atoms are identical and don't interact, the relative atomic population of the sub-levels is equivalent to the occupation probability of each, thus allowing an estimate of the system final quantum state. The coherences of the state can be measured as well, by implementing a quantum state tomography as we will discuss later in this thesis. Furthermore, a theoretical treatment for each interaction and a more complete description is given in the dedicated chapters, hence clarifying the chosen notation that better fits each experiment.

2.3.1 Microwave manipulation

The micro-wave manipulation is provided by the far-field produced by an external flat antenna placed on the optical table under the atom-chip as shown in Fig. 2.15. The generated microwave field has an angular frequency $\omega_{MW} =$

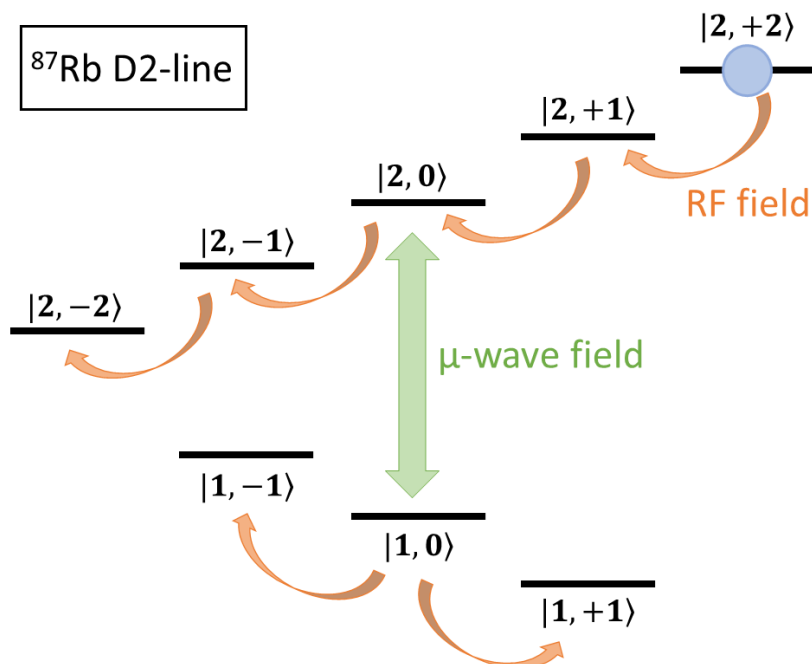


Figure 2.14: *Internal states manipulation of our BEC.* The Rubidium hyperfine structure is exploited to manipulate the internal state dynamics of the BEC. The radio-frequency interaction (orange arrows) drives the coherent evolution among the $|m_F\rangle$ sub-levels of the same manifold, while the micro-wave driving (green arrow) allows to jump from a manifold $F = 1$ to another $F = 2$.

$2\pi \times 6.834$ GHz in order to be resonant with the $|F = 1\rangle$ and $|F = 2\rangle$ energy splitting of the rubidium ground state. It is provided by a BCO Series phase-locked source in multiplied configuration (6834 multiplying factor) operating on an external reference frequency of 10 MHz. The reference frequency at 10 MHz is sent to the BCO by a signal generator. The timing of the output coming from the BCO is controlled by a series of three mixer that switch it off and on. Indeed, they are mixed with a signal coming from an arbitrary waveform generator that allows the modulation and control of the micro-wave signal with a resolution of 4 ns. The output is finally amplified and sent to the flat antenna via a SMA cable.

2.3.2 Radio-Frequency manipulation

The radio-frequency manipulation is provided by the near-field produced by the u-wire integrated on the atom-chip and highlighted in green in Fig. 2.4. We will refer to this wire calling it “*chip-antenna*” and we will restrict only to the dynamical evolution induced on the sub-manifold $F = 2$ where our BEC is produced. The chip-antenna generates a magnetic field induced by the current $I(t) = RA \cos(\omega_{RF}t)$

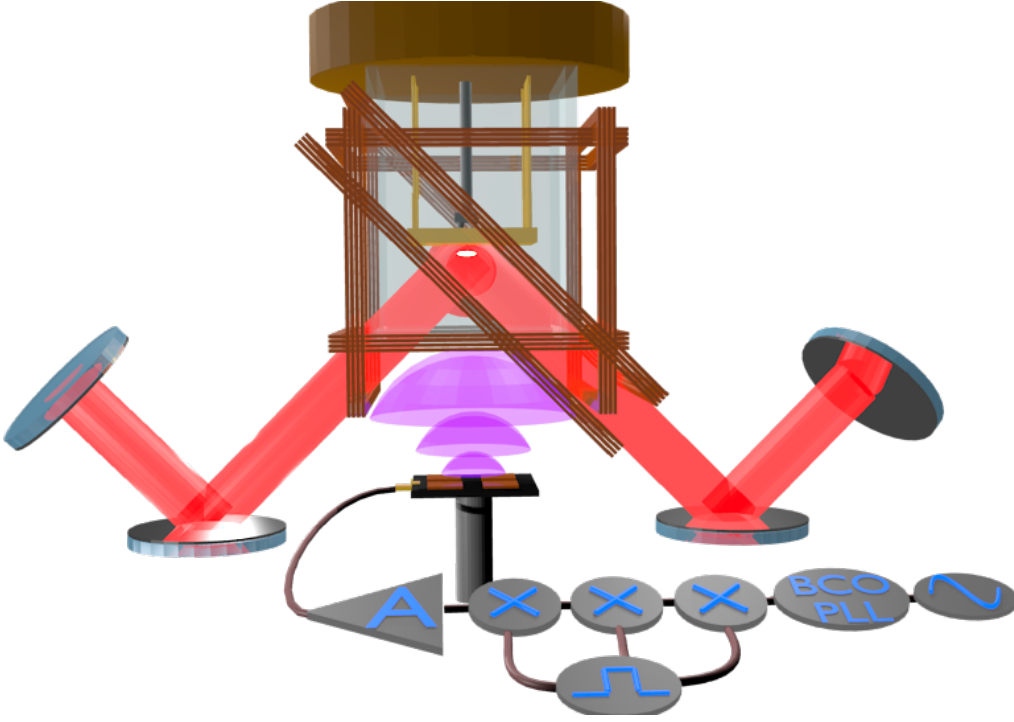


Figure 2.15: *Micro-wave antenna*. 3D reconstruction of the experimental setup used to couple the microwave antenna far-field with the atomic cloud. A sinusoidal signal at 10 MHz is the frequency reference for the BCO phased lock source. The signal timing is regulated by three mixer X controlled by an external rectangular-wave signal. After passing through an amplifier A, the output reaches the antenna via an SMA cable.

produced applying a voltage signal of amplitude A to its edges, R being the wire resistance and ω_{RF} the signal frequency. The corresponding magnetic field is $B(t) = B_{RF} \cos(\omega_{RF}t)$, where $B_{RF} = A\mu_0 R/2\pi d$ and $d = 190 \mu\text{m}$ is the distance of the condensate from the chip surface. When such a field is applied, the atoms in the BEC starts to coherently oscillate, with a Rabi frequency Ω , between the magnetic sub-levels $|m_F\rangle = \{+2, +1, 0, -1, -2\}$. Since the Rabi frequency Ω induced by the field is linear in B_{RF} , it turns also that $\Omega \propto A$. Therefore, the desired strength of the coupling between the atoms and the field can be tuned simply changing the applied signal amplitude A . In order to have an estimate of the relation between Ω and A , we measure the oscillations induced by radio-frequency signals of variable time duration $\tau_n = 2\pi n/\omega_{RF}$, n being an integer number, at different amplitudes [58]. In particular we set $\omega_{RF} = 2\pi \times 4.323 \text{ MHz}$ so to be resonant with the m_F sub-levels energy splitting induced by an external bias magnetic field $B = 6.1794 \text{ G}$ oriented along the \hat{y} direction, while the field induced by the radio-frequency signal is along \hat{x} . By fitting the theory to the experimental data produced by each evolution, we extract the dependency of Ω from the

amplitude A obtaining: $\Omega/2\pi \simeq 13.78A$ (kHz V⁻¹).

To tune the magnetic bias field at the desired value, instead, we use Ramsey spectroscopy [59]. We apply two radio-frequency pulses at $\Omega = 2\pi \times 60$ kHz and $\omega_{RF} = 2\pi \times 4.323$ MHz, both lasting $T_P = 2\pi \times \frac{18}{\omega_{RF}} \simeq 4.16$ μ s, one for preparation and one for recombination, separated by a free evolution time interval of $T_B \gg T_P$. Fitting the fringes produced by different currents I_B applied to the external Helmholtz bias coils, we obtain the linear relation $B \simeq 1.727I_B$ (G A⁻¹) [58]. As it will be cleared in chapter 4 by experimental evidence, the radio-frequency manipulation time lasts about 100 μ s. After this time, decoherence due to noise can occur.

3 | State manipulation and control for Quantum Machine Learning

Nowadays the need of processing large amounts of data is considerably increasing, and the development of supercomputers has further encouraged the advancement of quantum technologies and the study of algorithms in that direction. Classical Machine Learning (ML), as a field of study that aims at developing computer algorithms that learn through experience, has already improved the field of artificial intelligence (AI) technology in which the system can learn from data and make consequent decisions with minimal human intervention. The applications of these kind of algorithms is extremely wide [62–65] and is still growing in the direction of finding efficient solutions in handling of big data [66]. However, the natural structure of the original data can be very complex and an intensive preprocessing is often necessary for ML algorithms to perform efficiently. The introduction of Quantum Machine Learning (QML) algorithms has provided a remarkable speed-up over their classical counterparts, as in performing tasks of topological data analysis, principal components analysis and support vector machines (SVMs) [60, 61, 81]. In the case of binary classification problems, one would aim at achieving a geometrical representation of the data in which they are easier to be identified into distinct categories later to be analyzed. In this context, we have investigated QML using parametrized quantum circuits that *embed* the input data in Hilbert space and perform quantum measurements to discriminate between classes. In particular, we have developed an extensive experimental study of this Quantum Embedding (QE) procedure by implementing the ideas proposed by Ref. [86] carried out on multiple experimental platforms. We have investigated how the protocol can be tailored to ultra-cold atoms, photonics, and via-cloud available NISQ [83] computers. Starting from a single prescription, we have implemented three different experiments, highlighting requirements and tolerances of each one for this task.

In the context of this thesis I will emphasize the description of the atomic plat-

form in which I realized the embedding on a BEC of ^{87}Rb atoms. The chapter is thus structured as follows. An introduction to the types of ML learning algorithms is presented in Sec. 3.1. The embedding protocol we implement, specifically, falls in the category of classification algorithms. Therefore, kernel-based methods are discussed in Sec. 3.2, which are the cornerstone of ML and offer a deep theoretical understanding. Here I highlight the peculiar topic of Quantum Embedding Kernels (QEKs) on which our work focus. I highlight how such a subclass of kernel methods is the ideal candidate to realize Quantum Machine Learning (QML) models. The training of our quantum embedding protocol is subsequently explained in Sec. 3.3. The theoretical background necessary to clarify the used notation and to understand the experimental implementation of such algorithm on the atomic platform is then described (Sec. 3.4). Here I focus on the Bloch sphere representation of atomic two-level systems and the description of their unitary evolution on it. I show how an atomic platform naturally suits the embedding scheme, by virtue of the fact that the manipulation of the atomic internal states is carried out by a sequence of rotations. The experimental implementation and the results achieved are then detailed in Sec. 3.5, together with the limits I encountered and the possible solutions proposed. Finally, in Sec. 3.6, the results of the superconductive and photonic platforms are also detailed. In the conclusion and discussion Sec. 3.7, I compare all the obtained results successfully demonstrating the quantum embedding protocol at different experimental levels. The specific features come into play in a complementary fashion, hence supporting the promising idea of hybrid quantum technologies for future quantum machine learning applications.

The fundamental results reported in this chapter are available at:

- Ilaria Gianani, Ivana Mastroserio, Lorenzo Buffoni, Natalia Bruno, Ludovica Donati, Valeria Cimini, Marco Barbieri, Francesco S. Cataliotti, and Filippo Caruso, *Experimental Quantum Embedding for Machine Learning*. Eprint: arXiv:2106.13835 (2021).

They are achieved within a collaboration with the theory group of Prof. Filippo Caruso, *Università di Firenze*, and the experimental group of Prof. Marco Barbieri, *Università degli Studi di Roma Tre*.

Prof. Caruso conceived the whole project and his theory group performed the numerical optimization and the analysis of the results from the Rigetti superconductive platform. The group of Prof. Barbieri carried out the experiment on the photonic platform. Within the experimental group supervised by Prof. Francesco S. Cataliotti, *Università di Firenze* and *Istituto Nazionale di Ottica (CNR-INO) Firenze*, I performed the experiment on the atomic platform.

3.1 Types of learning algorithms

Since ancient times transferring acquired knowledge has induced mankind to develop solutions by applying established results in different contexts. This tendency remains valid even for today's most sophisticated technologies. Indeed, the current need of processing large amount of data and the availability of supercomputers has fostered an innovative take on programming: rather than trying and structuring the database so that a computer can walk through it, we now mimic processes of natural intelligence [68–70]. Algorithms are then able to act as quasi-conscious agents, thanks to the introduction of Machine Learning (ML). Artificial intelligence (AI) technology aspiration is to realize machines that mimic the *cognitive* functions of human's mind, such as *learning* and *problem solving*. In this regard, the Machine Learning subset branch deals with developing computer algorithms that improve autonomously through experience. After having experienced a learning data set, the learning-machine should accurately perform new unseen tasks. The types of ML algorithms differ in their approach to construct learning models. They can be divided into the three following broad categories [71]:

- **Supervised learning** [72,73]. In these kind of algorithms, the goal of the learning-machine is to build a general rule that maps an input in the correct output. This is realized on the basis of some previously learned *example inputs* and their *desired outputs*. For instance, consider a dataset $\{(x_i, y_i)\}_{i=1}^N$, where x_i are the inputs, or *feature vectors*, that constitutes the training examples. The elements y_i are, instead, the labels on which we build the knowledge of the learning algorithm. Through an iterative optimization of an objective function, the supervised learning algorithm produces a model that can predict the correct label y to be assigned to a new input x that is not belonging to the training data. Classification and regression algorithms fall in this category.
- **Unsupervised learning** [74–76]. These kind of algorithms have in input a collection of unlabeled vectors $\{x_i\}_{i=1}^N$. They have to find on their own, thus without feedbacks, some common properties from the input data in order to group or cluster them into categories. The algorithm will react positively or negatively based on the presence or absence of those common features. Typical applications of unsupervised learning are dimensionality reduction, density estimation, similarity metric.
- **Reinforcement learning** [62]. In this kind of algorithms the learning-machine interacts with an environment in which it must perform some goal. The machine can perform different actions and in particular has to

maximize a notion of cumulative reward. The goal is to learn a strategy that associates to a particular feature vector, representing the environment state, the best action to execute. The optimal policy maximizes the expected average reward. Reinforcement learning algorithm finds wide general applications, such as game theory, like playing chess, information theory, genetic algorithms, autonomous vehicles.

The quantum protocol described in this chapter is developed in the context of classification algorithms, thus belonging to the category of supervised learning models. The idea is similar in spirit to classical Support Vector Machines (SVMs) [72] first developed at AT&T Bell Laboratories by Vapnik and colleagues [77, 78]. SVM, indeed, maps some training examples to points in space in order to maximize the width of the gap between the two categories. It can efficiently perform also non-linear classification using the so called *kernel trick* that maps the inputs into high-dimensional feature space, as will be cleared in the following section.

3.2 Quantum embedding kernels

Kernel machines are a class of algorithms that makes use of *kernel functions*. A kernel function transfers some raw data into a high-dimensional space in which their classification is easier. To better understand what kernel methods do, let us consider some examples and simple definitions [86, 87]. In particular we want to relate this overview in the context of our quantum protocol investigation. The latter faces the problem of *linear classification* in which we want to assign binary labels to datapoints dividing them into regions separated by a linear boundary. It is an approach similar to that of Support Vector Machines that is the best known member of supervised learning models using kernel methods.

Given a data domain X , and a set of data samples $\{a_1, \dots, a_{M_a}\}$ from class $A \subseteq X$ with label $y = 1$ and a set of data samples $\{b_1, \dots, b_{M_b}\}$ from class $B \subseteq X$ with label $y = -1$, the problem of binary classification is to predict the label of a new input $x \in X$ assigning it to either class A or class B . A *classifier* is an algorithm that solves the problem of binary classification. It is a *map* from the data domain to the real numbers $f : X \rightarrow \mathbb{R}$. It assigns a binary label to x according to the threshold rule:

$$y = \begin{cases} -1 & \text{if } f(x) < \tau \\ 1 & \text{if } f(x) \geq \tau \end{cases} \quad \tau \in \mathbb{R} \quad (3.1)$$

If no other information is provided, τ is assumed to be zero. An example of linear classifier is reported in Fig. 3.1, where the decision boundary is a straight line that divides full circles from empty circles. The margins, defined by support

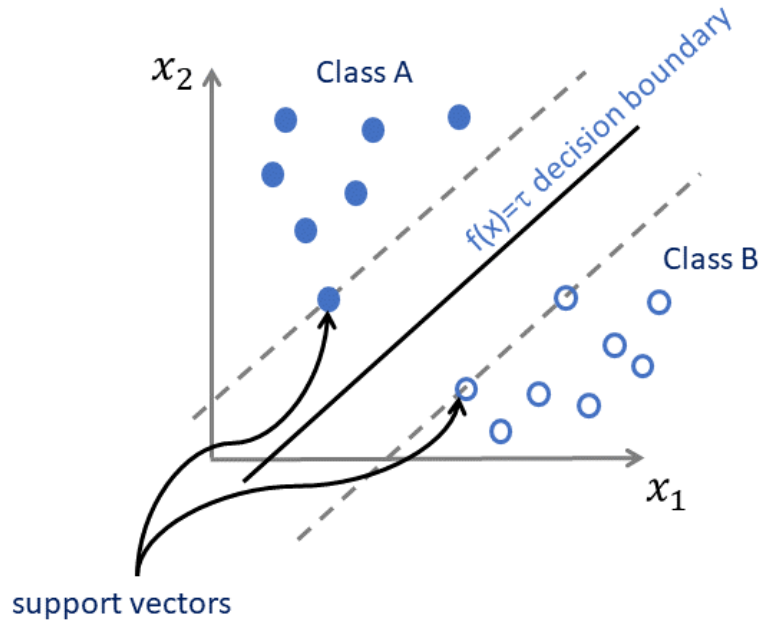


Figure 3.1: *Linear classifier*. A linear decision boundary separates full circles from empty circles. The samples that delimit the margins are called *support vectors*.

vectors, describe the distance of the dataset on either side of the line. Having a larger margin is intuitively the best situation, indeed outliers of the dataset have smaller chance to be wrongly classified. The same reasoning works for higher dimensional spaces too, where the decision boundary does not just define a line but a hyperplane. However, this method of linear classification is not always possible. Indeed, there are datasets that are not separable by a hyperplane and thus cannot be classified with high accuracy using this scheme. In order to enhance the capabilities of a linear classifier, one can use a *feature map* $\Phi(x)$ that embeds them into a larger *feature space* in which the linear classification is possible. Such a strategy is very powerful inasmuch allows to perform non-linear classification in the original space of datasets. Usually this is done by means of a function k called *kernel*, to which the feature map Φ is associated. It is a function that contains only the inner products between vectors in the embedding space:

$$k(\mathbf{x}, \mathbf{x}') = \langle \Phi(\mathbf{x}), \Phi(\mathbf{x}') \rangle. \quad (3.2)$$

It is the central property of kernel-based methods, indeed using the trick of just computing the inner products between the images of all pairs of data in the feature space, one has no need to explicitly compute all the coordinates of the feature vectors. In many cases, computing the embedding requires a much higher cost with respect to the computationally cheaper kernel. This implicit embed-

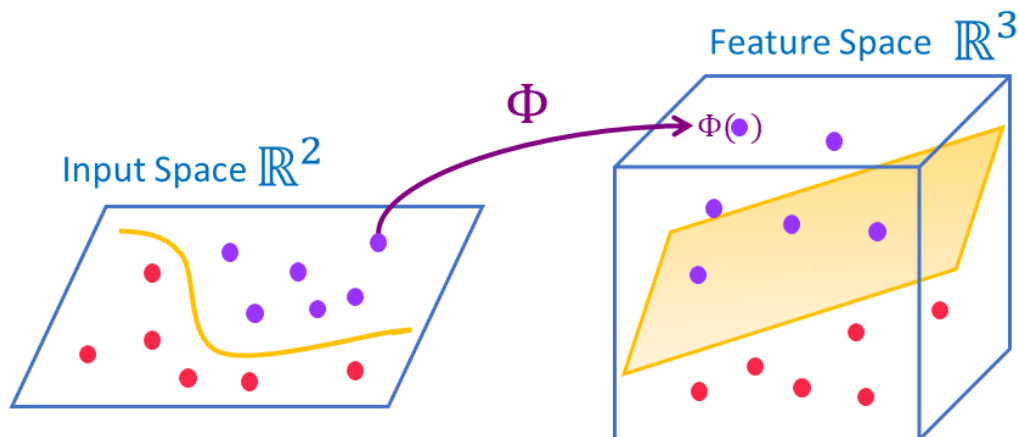


Figure 3.2: *The kernel trick*. A set of training points, originally belonging to a 2-dimensional input space in which they are not linearly separable, are mapped via a feature transformation Φ into a 3-dimensional space where a separating hyperplane can be easily found.

ding through its associated kernel is known as the kernel trick, and is pictorially shown in Fig. 3.2. In general, any function fulfilling the *Mercer condition*:

$$\sum_{i,j} c_i c_j k(\mathbf{x}_i, \mathbf{x}_j) \geq 0 \quad (3.3)$$

for all possible sets of real coefficients $\{c_i\}$ and sets of datapoints $\{\mathbf{x}_i\}$, is a kernel. Despite kernel machines are extremely useful to understand the learning methods, the current progress in learning models is dominated by deep neural networks. Kernel matrices, indeed, need to be constructed from the input data and have quadratic complexity in the number of datapoints. In the context of *big data*, this can constitute an obstacle. Other than that finding the suitable kernel for a given problem is not always a trivial task.

An interesting solution is provided by quantum mechanics. Indeed, quantum computers can perform kernel methods with an exponential speed up over the corresponding classical operations [67]. *Quantum embedding kernels* (QEKs) are a subclass of quantum kernel methods where a parametrized quantum circuit (PQCs) [79–82] is used to embed data-points into the Hilbert space of quantum states of a NISQ device [83]. Noisy Intermediate-Scale Quantum (NISQ) is a term coined by John Preskill in 2018 to describe the current state of art in the realization of quantum processors. The latter would be able to perform computations that are intractable for classical computers [67, 84, 85]. This comes in the framework of an exchange of concepts and methods between Machine Learning and quantum information.

Even in the simplest instance, the natural representation of a quantum bit is

the Bloch sphere, rather than the single-dimensional geometry of classical data. *Quantum classifiers* are models that use quantum theory to solve classification tasks. They make use of *quantum embeddings* which effectively embed data-points in the Hilbert space of quantum states, facilitated by a *quantum feature map*. To implement the latter on a NISQ hardware, quantum gates like Pauli rotations are used. They are unitary operations $\mathcal{U}(\mathbf{x})$ that depend on the specific data \mathbf{x} in input and constitute a *quantum circuit*. Once the data are loaded, the quantum feature map is thus represented by the action:

$$|\Phi(\mathbf{x})\rangle = \mathcal{U}(\mathbf{x})|0\rangle. \quad (3.4)$$

The associated quantum embedding kernel (QEK) is given by the *overlap* between the embeddings:

$$k(\mathbf{x}, \mathbf{x}') = |\langle\Phi(\mathbf{x}')|\Phi(\mathbf{x})\rangle|^2. \quad (3.5)$$

This is a definition for pure quantum states. However, it is not always possible to avoid noise. The embedded quantum state in this case is better represented by its associated density matrix $\rho(\mathbf{x})$, which for a pure state reduces to $\rho(\mathbf{x}) = |\Phi(\mathbf{x})\rangle\langle\Phi(\mathbf{x})|$. The quantum kernel becomes the Hilbert-Schmidt inner product for matrices:

$$k(\mathbf{x}, \mathbf{x}') = \text{Tr}\{\rho(\mathbf{x}), \rho(\mathbf{x}')\}. \quad (3.6)$$

In order to be able to use this kernel, the overlap of two quantum states needs to be computed on a NISQ device. There are many algorithms that realize this task [88–92], but here we will linger on the *fidelity classifier*. Indeed, the latter is the one used in this work to test the success of our embedding protocol.

Let us go back to the two classes A and B previously defined. The sampling of M quantum states from a set $\{|\psi_i\rangle\}$ is described by the density matrix $\rho = \frac{1}{M} \sum_i |\psi_i\rangle\langle\psi_i|$. According to this definition, we can sample M_a inputs from class A and embed them into Hilbert space in the ensemble $\rho = \frac{1}{M_a} \sum_{a \in A} |a\rangle\langle a|$. Similarly, we sample M_b inputs from class B in the ensemble $\sigma = \frac{1}{M_b} \sum_{b \in B} |b\rangle\langle b|$. Thus, ρ and σ are mixed states that describe the process of selecting embedded data point $|a\rangle$ and $|b\rangle$ with uniform probability from a training set.

The fidelity classifier is defined as:

$$f_{fid} = \langle x | \rho - \sigma | x \rangle. \quad (3.7)$$

Eq. (3.7) measures the fidelity, or overlap, between data states, indeed:

$$\langle x | \rho - \sigma | x \rangle = \frac{1}{M_a} \sum_a |\langle a | x \rangle|^2 - \frac{1}{M_b} \sum_b |\langle b | x \rangle|^2. \quad (3.8)$$

This operation requires a very few resources on a quantum computer. A quantum circuit for the fidelity classifier can, indeed, be efficiently implemented. It can be

performed by a C-SWAP test (see Appendix B), which measures the overlap of two quantum states using an auxiliary ulterior qubit. The quality of the fidelity classifier can be estimated, according to statistical learning theory, by analyzing the expected risk. In our case it results that:

$$\hat{I}[f_{fid}] = -\text{Tr} [(\rho - \sigma)^2] = -D_{H-S}(\rho, \sigma), \quad (3.9)$$

the empirical risk of the fidelity classifier under linear loss is opposite to the Hilbert-Schmidt distance. Thus maximizing the distance between the embeddings belonging to different classes, is equivalent to minimize the expected risk. These considerations have led us to construct the cost function used to train an optimal quantum feature map for our experimental protocol.

3.3 Training Quantum Embedding

In our investigation we explore the application of quantum embedding in the minimalistic, but illustrative instance, of a single-qubit embedder. This is carried out in two steps. In the first *learning* stage we train and identify the optimal quantum circuit that realizes the embedding. We adapt and numerically optimize the quantum embedding protocol by Machine Learning methods, mapping the data into new clusters that later can be more feasibly and possibly linearly separated by well trained artificial neural networks. Secondly, the circuit is implemented in three different quantum architectures to explore how different sources of noise and imperfections impact the realization.

The learning stage starts from a complex classical data set made of 1000 points, in which some elements a_i belongs to class A and some elements b_j belongs to class B . The latter are represented in red and blue in Fig. 3.3. As shown, they cannot be linearly separated in their one-dimensional space, thus making the quantum embedding a suitable resource to classify the two classes. The full quantum embedding is realized by the *quantum feature map* $\Phi(x, \theta)$ that depends on the classical data point x and on the training parameters θ . We apply it to an input qubit $|0\rangle$, which can be the initial state of any physical system, thus transforming the data in the following quantum states:

$$\begin{aligned} a_i &\rightarrow |a_i\rangle = \Phi(x = a_i, \theta)|0\rangle, \\ b_j &\rightarrow |b_j\rangle = \Phi(x = b_j, \theta)|0\rangle, \end{aligned} \quad (3.10)$$

such that they are as separated as possible in the Hilbert space, as pictorially shown in Fig. 3.4. To do so, we need to train $\Phi(x, \theta)$ until we find the optimal transformation. The training consists in a first choice of two data points, from the string of 1000 data, and embed them in the Hilbert space by means of Eq. (3.10)

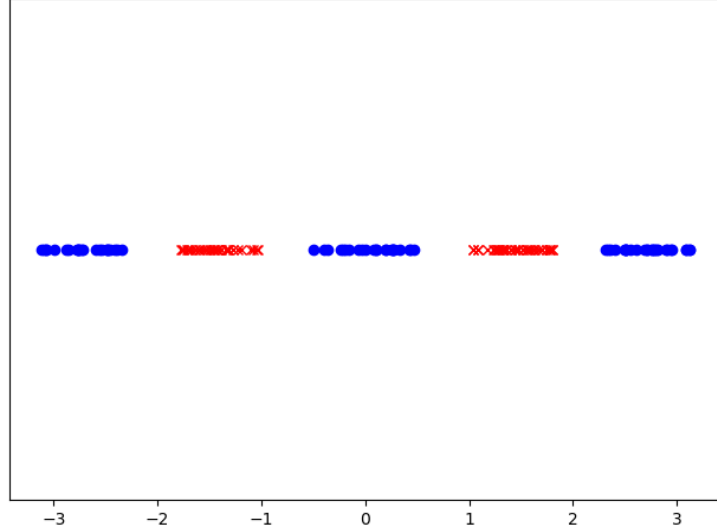


Figure 3.3: A string of classical data to be classified. The dataset, used for classification benchmark, is one-dimensional and it is not linearly separable. The classes (blue dots) and (red crosses) have been normalized to live in the interval $[-\pi, \pi]$.

with an initial random guess of the parameter θ . We then perform a C-SWAP test, between the two embedded quantum states, that computes the overlaps $|\langle a_i|b_j\rangle|^2$, $|\langle a_i|a_{i'}\rangle|^2$ and $|\langle b_j|b_{j'}\rangle|^2$ necessary to estimate the so-called *cost function* C (obtained specializing Eq. (3.8) to our case) defined as:

$$C = 1 - \frac{1}{2} \left(\sum_{i,i'} |\langle a_i|a_{i'}\rangle|^2 + \sum_{j,j'} |\langle b_j|b_{j'}\rangle|^2 \right) + \sum_{i,j} |\langle a_i|b_j\rangle|^2. \quad (3.11)$$

The optimal parameter θ will be the one that minimizes the cost-function. Indeed the first two terms, in Eq. (3.11), represents the distance, intended as the Hilbert-Schmidt norm, between points belonging to the same class. The third term represents the distance between points belonging to different classes. Overall, minimizing C is equivalent to both maximizing the Hilbert-Schmidt norm between elements of different classes and minimizing it between elements of the same class. The parameter of the embedding circuit is then updated by gradient descent using the automatic differentiation capabilities of the software PennyLane [93]. After 200 gradient descent steps (i.e. training steps) the cost function converges to a minimum, taking only a few minutes of computational time.

Once the optimization is done, meaning that the system has learned how to classify the data, we sample 10 more data points (not exploited for the training) in order to test the generalization capabilities of the embedding and to be the benchmark for all the experimental platforms. In our example, these points are

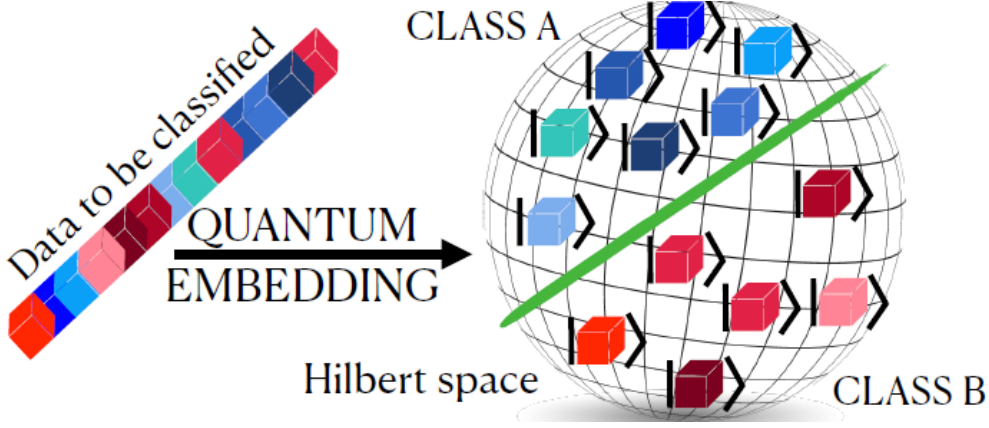


Figure 3.4: *Pictorial representation of quantum embedding.* The string of classical data on the left is composed by elements that belongs to two distinct classes A and B. They cannot be linearly separated in their one-dimensional representation. The quantum embedding algorithm transfers and separates the data in the Hilbert space where a classification boundary can be easily found.

10 scalars ϕ chosen in the interval $[-\pi, \pi]$ and arranged into two classes with 5 elements each. These test points are all correctly classified by the optimal circuit based on the following sequence of rotations on non-commuting axes of the Bloch sphere to be applied to the input qubit:

$$\Phi(\phi, \theta) = \{R_x(\phi), R_z(\theta_1), R_x(\phi), R_z(\theta_2), R_x(\phi), R_z(\theta_3), R_x(\phi)\}. \quad (3.12)$$

Here the circuit parameters to be optimized are $\theta = \{\theta_1, \theta_2, \theta_3\}$, in order to construct $|\phi\rangle$. From theory, we expect to see a clusterization of the two classes as depicted in Fig. 3.5.

We then implement the same embedding on the following three different experimental platforms, to test its robustness to real-world deployment scenarios.

- **Atomic platform.** The quantum embedding is performed on a BEC of ^{87}Rb atoms, in which the classical information to be encoded is mapped in the rotation angles of the Bloch vector, representing the atomic state, around the non commuting axes \hat{x} and \hat{z} of the Bloch sphere. The sequence of rotations necessary to realize the embedding is implemented by a series of quasi-resonant microwave pulses applied to the atoms.
- **Photonic platform.** The quantum embedding is performed on an optical experiment, applying the rotations to a heralded single-photon source generated via spontaneous parametric down conversion. A three-plate arrangement is used to impart the transformation dictated by the embedding sequence.

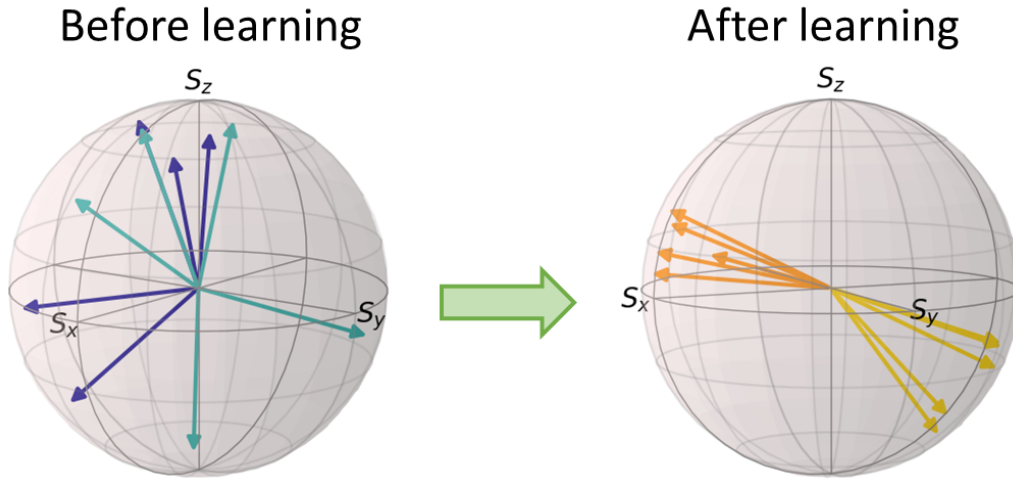


Figure 3.5: *Before and after learning.* Bloch sphere representation of the embedded quantum states that are randomly distributed (before learning) and clustered in two families (after learning), as provided by theory.

- **Superconducting platform.** The quantum embedding is performed on the superconducting chip of Rigetti [94] Aspen-8, composed by a lattice of 30 superconducting qubits in a ladder-like configuration. The rotations are implemented as quantum gates carried out remotely on the Rigetti’s cloud service.

Since different experiments have different capabilities, each implementation requires to “recompile” the embedding sequence to fit with the specifications of each device, while keeping the learned parameters fixed. Indeed, the scheme flexibility allows to extend the procedure to a more complex data set and to rotations around different axes in order to account for the specific needs. Finally, the performance of the embedding is conveniently captured, for each experimental platform, by the Gram matrix which contains all the scalar products between the embedded states. Therefore, if the system has learned to separate the points in the Hilbert space, the Gram matrix will clearly show a clusterization of quantum states into the two classes.

3.4 Theoretical background for the atomic platform

The manipulation of atomic internal states is naturally suited to the above scheme, since qubit operations in Eq. (3.12) are indeed rotations realized by sequences of

control pulses. In this regard, the intent of this section is to describe the coherent evolution of a two-level system, the atomic qubit, interacting with a single-frequency radiation in the representation of the Bloch sphere. Indeed, the latter gives a useful way of visualizing the effect of sequences of π - and $\pi/2$ -pulses on the atoms. Note that the notions reported in this section are universal for two-level systems, however I have chosen to present them here in order to clarify the notation that will be used in the experimental implementation. Furthermore, the described treatment is the foundation on which laser spectroscopy techniques are based and they are a crucial ingredient in the comprehension of the state manipulation and control work conducted in this thesis at this stage.

3.4.1 The Bloch sphere representation

The Bloch sphere is a very powerful tool to represent a two-level system and describe its dynamical evolution. The state $|\psi\rangle$ of a two-level system can be written as a superposition of the level at higher energy that we indicate as $|0\rangle$, and the level at lower energy indicated as $|1\rangle$. A generic superposition is:

$$|\psi\rangle = c_0|0\rangle + c_1|1\rangle \quad \rightarrow \quad |\psi\rangle = \begin{pmatrix} c_0 \\ c_1 \end{pmatrix} \quad (3.13)$$

where the squared magnitude of the coefficients $|c_0|^2$ and $|c_1|^2$ represent the probabilities of finding the atom in the upper state or in the lower state respectively, such that $|c_0|^2 + |c_1|^2 = 1$. They are complex numbers with two degrees of freedom each. Every transformation of $|\psi\rangle$, that leaves the state vector in the Hilbert space spanned by $|0\rangle$ and $|1\rangle$, can be represented by a 2×2 unitary matrix. These kinds of matrices can be written as a combination of the three Pauli matrices, representing the spin vector $\boldsymbol{\sigma} \equiv (\sigma_x, \sigma_y, \sigma_z)$, and the identity matrix:

$$\sigma_x = \begin{pmatrix} 0 & 1 \\ 1 & 0 \end{pmatrix}, \quad \sigma_y = \begin{pmatrix} 0 & -i \\ i & 0 \end{pmatrix}, \quad \sigma_z = \begin{pmatrix} 1 & 0 \\ 0 & -1 \end{pmatrix}, \quad \mathcal{I} = \begin{pmatrix} 1 & 0 \\ 0 & 1 \end{pmatrix}. \quad (3.14)$$

Some useful properties of the Pauli matrices are that $[\sigma_i, \sigma_j] = 2i\varepsilon_{ijk}\sigma_k$, where ε_{ijk} is the Levi-Civita symbol, and $\sigma_i\sigma_j = \delta_{ij}\mathcal{I} + i\varepsilon_{ijk}\sigma_k$. In particular, from the latter, we can retrieve the useful property:

$$e^{ia(\boldsymbol{\sigma} \cdot \hat{\mathbf{n}})} = \mathcal{I} \cos a + i(\boldsymbol{\sigma} \cdot \hat{\mathbf{n}}) \sin a, \quad (3.15)$$

where the operator $\boldsymbol{\sigma} \cdot \hat{\mathbf{n}}$ is the projection of the spin $\boldsymbol{\sigma}$ along a generic direction $\hat{\mathbf{n}} \equiv (\sin \vartheta \cos \varphi, \sin \vartheta \sin \varphi, \cos \vartheta)$ expressed in polar coordinates, with $\vartheta \in [0, \pi]$ and $\varphi \in [0, 2\pi]$.

The state $|\psi\rangle$ of a two-level system can be seen as an eigenstate of $\boldsymbol{\sigma} \cdot \hat{\mathbf{n}}$. This

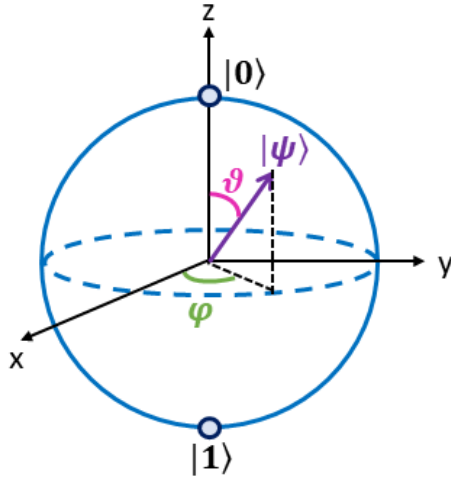


Figure 3.6: *Bloch sphere representation of a qubit.* The state $|\psi\rangle$ of a two-level system, standing for a qubit, can be identified as a point on the surface of the Bloch sphere having coordinates $\boldsymbol{\psi} \equiv (\sin \vartheta \cos \varphi, \sin \vartheta \sin \varphi, \cos \vartheta)$.

operator's eigenvalues are ± 1 . Solving the equation $(\boldsymbol{\sigma} \cdot \mathbf{n} - \mathcal{I})|\psi\rangle = 0$, for the eigenvalue $+1$, we find the following expression for $|\psi\rangle$:

$$|\psi\rangle = \cos\left(\frac{\vartheta}{2}\right)|0\rangle + e^{i\varphi} \sin\left(\frac{\vartheta}{2}\right)|1\rangle. \quad (3.16)$$

Therefore, the probability amplitudes for the superposition state are the quantities $c_0 = \cos(\vartheta/2)$ and $c_1 = e^{i\varphi} \sin(\vartheta/2)$, having just two degrees of freedom, and $e^{i\varphi}$ being the relative phase factor.

Note that the expectation values of σ_x , σ_y and σ_z on $|\psi\rangle$ are:

$$\begin{aligned} \langle \sigma_x \rangle &= \langle \psi | \sigma_x | \psi \rangle = \sin \vartheta \cos \varphi; \\ \langle \sigma_y \rangle &= \langle \psi | \sigma_y | \psi \rangle = \sin \vartheta \sin \varphi; \\ \langle \sigma_z \rangle &= \langle \psi | \sigma_z | \psi \rangle = \cos \vartheta. \end{aligned} \quad (3.17)$$

Hence, a generic state $|\psi\rangle$ of a two-level system, representing a *qubit*, corresponds to the unit vector:

$$|\psi\rangle \Leftrightarrow \boldsymbol{\psi} = \boldsymbol{\sigma} \equiv (\sin \vartheta \cos \varphi, \sin \vartheta \sin \varphi, \cos \vartheta). \quad (3.18)$$

We can thus visualize this vector lying on a sphere, the *Bloch sphere* (see Fig. 3.6), and name it *Bloch vector*. In this representation a classical bit can only be at the North pole $|0\rangle$ or at the South pole $|1\rangle$. A pure state is represented by a point on the surface of the Bloch sphere, while a mixed state is a point inside the sphere that is a vector with a length smaller than its unit radius.

3.4.2 Unitary evolution on the Bloch sphere

When an atom interacts with an external field, the Bloch vector representing its quantum state will start moving on the Bloch sphere surface. The induced

coherent evolution of its state can thus be described by a trajectory lying on the Bloch sphere surface. To understand how powerful this representation is, due to its simplicity, let us consider again the two-level system previously described in which now we introduce an interaction. The complete Hamiltonian $H = H_0 + H_I$ representing this interacting system is characterized by the unperturbed term $H_0 = \hbar\omega_{|1\rangle}|1\rangle\langle 1| + \hbar\omega_{|0\rangle}|0\rangle\langle 0|$, where $\hbar\omega_{|1\rangle}$ and $\hbar\omega_{|0\rangle}$ are the energies of the ground level $|1\rangle$ and the excited level $|0\rangle$ respectively, and the interaction term H_I . We choose the zero-energy of the system in such a way that we can rewrite the unperturbed term as:

$$\begin{aligned} H_0 &= \frac{\hbar\omega_0}{2} (|0\rangle\langle 0| - |1\rangle\langle 1|), \\ &= \frac{\hbar\omega_0}{2} \begin{pmatrix} 1 & 0 \\ 0 & -1 \end{pmatrix}, \\ &= \frac{\hbar\omega_0}{2} \sigma_z, \end{aligned} \quad (3.19)$$

where $\omega_0 = \omega_{|0\rangle} - \omega_{|1\rangle}$. In our experiment, the role of the interaction is played by the external microwave magnetic field generated by the antenna described in Subsec. 2.3.1. Therefore, the interaction term is given by $H_I = -\hat{\boldsymbol{\mu}} \cdot \mathbf{B}$. We adopt a semiclassical approach in which the oscillating magnetic field is treated as a classical wave $\mathbf{B} = B_0 \hat{b} \cos(\omega t + \phi) = \frac{B_0 \hat{b}}{2} (e^{i(\omega t + \phi)} + e^{-i(\omega t + \phi)})$, where ω and ϕ are the microwave frequency and phase respectively, B_0 is the magnetic field amplitude and \hat{b} is the unit vector that indicates its direction. $\hat{\boldsymbol{\mu}}$, instead, is the magnetic dipole moment operator that writes:

$$\begin{aligned} \hat{\boldsymbol{\mu}} &= \boldsymbol{\mu} (|0\rangle\langle 1| + |1\rangle\langle 0|), \\ &= \boldsymbol{\mu} \begin{pmatrix} 0 & 1 \\ 1 & 0 \end{pmatrix}, \\ &= \boldsymbol{\mu} \sigma_x, \end{aligned} \quad (3.20)$$

where $\boldsymbol{\mu}$ is real and is defined as the matrix element $\boldsymbol{\mu} \equiv \langle 1|\hat{\boldsymbol{\mu}}|0\rangle = \langle 0|\hat{\boldsymbol{\mu}}|1\rangle$. Note that the magnetic dipole moment operator applied to the $|1\rangle$ state swaps it into $|0\rangle$ and viceversa. It is a hermitian operator $\hat{\boldsymbol{\mu}}^\dagger = \hat{\boldsymbol{\mu}}$ and it is symmetric. Substituting in H_I we obtain the following expression for the interaction:

$$H_I = \frac{\hbar\Omega}{2} \sigma_x \left(e^{i(\omega t + \phi)} + e^{-i(\omega t + \phi)} \right), \quad (3.21)$$

under which the atomic population of the two levels starts to oscillate at the Rabi frequency defined as:

$$\Omega = -\frac{\boldsymbol{\mu} \cdot \hat{b} B_0}{\hbar}. \quad (3.22)$$

It is worth noting that in a full quantized approach, the quantization of the electro-magnetic (EM) field leads to write the magnetic field operator as:

$$\hat{\mathbf{B}}(t) = i\hat{b}\sqrt{\frac{\hbar}{2\omega\epsilon_0V}}\left(\hat{a}e^{-i(\omega t+\phi)} - \hat{a}^\dagger e^{i(\omega t+\phi)}\right), \quad (3.23)$$

in which the annihilation of a photon, by means of the operator \hat{a} , is associated to the term of the field $e^{-i\omega t}$ having positive frequency, while the creation of a photon, by means of the operator \hat{a}^\dagger , is associated to the one having negative frequency $e^{i\omega t}$. Hence, the interaction Hamiltonian is made by the following four terms:

- 1) $|0\rangle\langle 1|e^{-i\omega t}$: a photon is annihilated and the atom excites;
- 2) $|0\rangle\langle 1|e^{i\omega t}$: a photon is created and the atom excites;
- 3) $|1\rangle\langle 0|e^{-i\omega t}$: a photon is annihilated and the atom deexcites;
- 4) $|1\rangle\langle 0|e^{i\omega t}$: a photon is created and the atom deexcites.

The processes indicated by 2) and 3) do not preserve the energy and are out of resonance. Neglecting these terms, amounts to adopting the *Rotating Wave Approximation* (RWA). Therefore, going back to our semiclassical model, we write:

$$H_I = \frac{\hbar\Omega}{2}\left(\sigma_+e^{-i(\omega t+\phi)} + \sigma_-e^{i(\omega t+\phi)}\right), \quad (3.24)$$

where:

$$\sigma_+ = |0\rangle\langle 1| = \begin{pmatrix} 0 & 1 \\ 0 & 0 \end{pmatrix}, \quad \sigma_- = |1\rangle\langle 0| = \begin{pmatrix} 0 & 0 \\ 1 & 0 \end{pmatrix}. \quad (3.25)$$

With this approximation and switching to a rotating frame at the same frequency of the external field ω , we can conclude some interesting observations. Consider the unitary transformation:

$$\mathcal{U} = \exp\left\{-i\frac{\omega t}{2}\sigma_z\right\} = \begin{pmatrix} e^{-i\frac{\omega t}{2}} & 0 \\ 0 & e^{i\frac{\omega t}{2}} \end{pmatrix}, \quad (3.26)$$

such that $|\psi\rangle = \mathcal{U}|\tilde{\psi}\rangle$ and according to which the Hamiltonian transforms as:

$$H \xrightarrow{\mathcal{U}} \tilde{H} = \mathcal{U}^\dagger H \mathcal{U} - i\hbar\mathcal{U}^\dagger \frac{\partial \mathcal{U}}{\partial t}. \quad (3.27)$$

Considering each term separately we have:

$$\begin{aligned}
 \mathcal{U}^\dagger H_0 \mathcal{U} &= \frac{\hbar\omega_0}{2} \sigma_z, \\
 \mathcal{U}^\dagger H_I \mathcal{U} &= \frac{\hbar\Omega}{2} (\cos \phi \sigma_x + \sin \phi \sigma_y), \\
 -i\hbar \mathcal{U}^\dagger \frac{\partial \mathcal{U}}{\partial t} &= -\frac{\hbar\omega}{2} \sigma_z.
 \end{aligned} \tag{3.28}$$

We observe that, defining the detuning as $\Delta = \omega - \omega_0$, we get:

$$\begin{aligned}
 \tilde{H} &= -\frac{\hbar\Delta}{2} \sigma_z + \frac{\hbar\Omega}{2} (\cos \phi \sigma_x + \sin \phi \sigma_y), \\
 &= \frac{\hbar\Omega}{2} \cos \phi \sigma_x + \frac{\hbar\Omega}{2} \sin \phi \sigma_y - \frac{\hbar\Delta}{2} \sigma_z.
 \end{aligned} \tag{3.29}$$

In this frame, that rotates at the frequency of the external field, we arrive at the important conclusion that the Hamiltonian is the scalar product:

$$\tilde{H} = \frac{\hbar}{2} (\boldsymbol{\Omega} \cdot \boldsymbol{\sigma}), \tag{3.30}$$

between the spin vector $\boldsymbol{\sigma}$ and the Rabi vector identified on the Bloch sphere by the coordinates:

$$\boldsymbol{\Omega} = (\Omega \cos \phi, \Omega \sin \phi, -\Delta). \tag{3.31}$$

Furthermore, substituting this result in the Heisenberg equation for $\boldsymbol{\sigma}$ and in force of the commutation rules $[\sigma_i, \sigma_j] = 2i\varepsilon_{ijk}\sigma_k$, we get the fundamental result:

$$\frac{d\boldsymbol{\sigma}}{dt} = \boldsymbol{\Omega} \times \boldsymbol{\sigma}. \tag{3.32}$$

This means that in the Bloch description, the fictitious magnetic field lies along $\boldsymbol{\Omega}$ and the two-level system response to it is a precession motion around it with a precession rate given by the Rabi vector magnitude $|\boldsymbol{\Omega}| = \sqrt{\Omega^2 + \Delta^2}$, usually known as the *generalized Rabi frequency*.

This visual interpretation given by the Bloch sphere is an indispensable ingredient for designing an interaction made of a complex sequence of pulses, such as those used in the experimental implementation of quantum embedding as will be further clarified in the following.

In our experiment the microwave field that drives the evolution can be well represented by the unitary operator:

$$\mathcal{U}_\Omega(\Omega, \phi, \Delta, t) = \exp \left\{ -\frac{i|\boldsymbol{\Omega}|t}{2} \mathbf{n}_\Omega \cdot \boldsymbol{\sigma} \right\}, \tag{3.33}$$

where Ω is the Rabi frequency induced by the microwave field on the atoms, ϕ is the phase of the microwave signal that we set to zero, Δ is the detuning of the signal frequency from resonance, $|\Omega|$ is the magnitude of the Rabi vector induced by the microwave field, and:

$$\mathbf{n}_\Omega(\Omega, \phi = 0, \Delta) = (n_x, n_y, n_z) = \left(\frac{\Omega}{|\Omega|}, 0, -\frac{\Delta}{|\Omega|} \right) \quad (3.34)$$

is the rotation axis directed along Ω and around which the Bloch vector, representing the state of our system, precesses. It is worth noting that the choice $\phi = 0$ is equivalent to set a time origin of the evolution induced by the microwave field. Hence, the notation reported in the following is a reflection of this choice further supported by the fact that during our experiment the phase ϕ is not changed and remains zero during the whole evolution.

Thanks to the property of Eq. (3.15), the evolution operator of Eq. (3.33) can be rewritten as:

$$\mathcal{U}_\Omega(\Omega, \phi, \Delta, t) = \mathcal{I} \cos\left(\frac{|\Omega|t}{2}\right) - i(\mathbf{n}_\Omega \cdot \boldsymbol{\sigma}) \sin\left(\frac{|\Omega|t}{2}\right), \quad (3.35)$$

and its explicit 2×2 matrix form is the following:

$$\mathcal{U}_\Omega = \begin{pmatrix} \cos\left(\frac{|\Omega|t}{2}\right) + i\frac{\Delta}{|\Omega|} \sin\left(\frac{|\Omega|t}{2}\right) & -i\frac{\Omega}{|\Omega|} \sin\left(\frac{|\Omega|t}{2}\right) \\ -i\frac{\Omega}{|\Omega|} \sin\left(\frac{|\Omega|t}{2}\right) & \cos\left(\frac{|\Omega|t}{2}\right) - i\frac{\Delta}{|\Omega|} \sin\left(\frac{|\Omega|t}{2}\right) \end{pmatrix}. \quad (3.36)$$

We can describe this evolution in an equivalent way on the three dimensional Bloch sphere. The Bloch vector, indeed, evolves rotating of an angle $\alpha = |\Omega|t$ around the direction $\mathbf{n}_\Omega = (n_x, n_y, n_z)$ according to the following 3×3 matrix:

$$R(\alpha) = \begin{pmatrix} \cos \alpha + n_x^2(1 - \cos \alpha) & -n_z \sin \alpha & n_x n_z(1 - \cos \alpha) \\ n_z \sin \alpha & \cos \alpha & -n_x \sin \alpha \\ n_x n_z(1 - \cos \alpha) & n_x \sin \alpha & \cos \alpha + n_z^2(1 - \cos \alpha) \end{pmatrix}. \quad (3.37)$$

Therefore, we can experimentally design the desired evolution setting the fundamental parameters that are the Rabi frequency Ω , the detuning Δ and the interaction time duration t . All the experimental procedures in realizing the quantum embedding protocol on the atomic platform are based on these simple assumptions and will be described in the next sections.

3.4.3 Rotations around x-axis: controlled evolution

It is now straightforward specializing to the case of an evolution that contemplates just a rotation around the Bloch sphere x-axis. Thus, the direction along

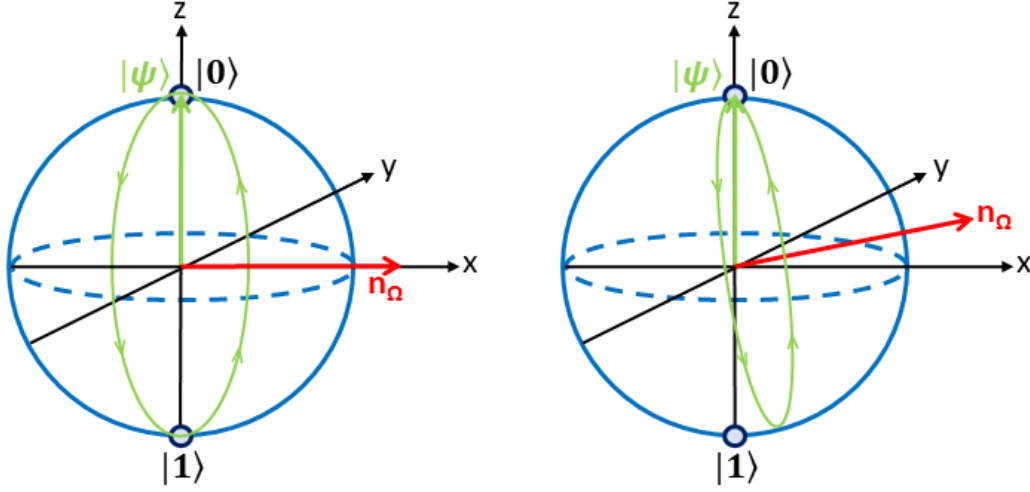


Figure 3.7: Rotations around \hat{x} . Precession of the Bloch vector $|\psi\rangle$ about the effective microwave field directed along $\mathbf{n}_\Omega = (n_x, 0, 0)$ for $\Delta = 0$ (left-hand side) and $\Delta \neq 0$ (right-hand side).

which \mathbf{n}_Ω is oriented, in this case, is $\mathbf{n}_\Omega = (n_x, 0, 0)$ and $\Omega = (\Omega, 0, 0)$. This means that in the case of a resonant microwave field ($\Delta = 0$) the direction of the Rabi vector is identified by the unit vector $\mathbf{n}_\Omega = (1, 0, 0)$ and the Bloch state, starting for instance from the initial state $|\psi\rangle = |0\rangle$, precesses around it about an angle $\alpha = \Omega t$ given by the Rabi frequency and the interaction time duration (as depicted in the left-hand side of Fig. 3.7). The motion will be clockwise or counterclockwise depending on the sign of the Rabi frequency and the evolution operator that describes it becomes:

$$\mathcal{U}_{\Omega, \hat{x}} = \begin{pmatrix} \cos\left(\frac{\Omega t}{2}\right) & -i \sin\left(\frac{\Omega t}{2}\right) \\ -i \sin\left(\frac{\Omega t}{2}\right) & \cos\left(\frac{\Omega t}{2}\right) \end{pmatrix}. \quad (3.38)$$

In the presence of a slightly-detuned from resonance field ($\Delta \neq 0$), instead, the precession axis is tilted as shown in the right-hand side of Fig. 3.7. The direction of the effective magnetic field will be close but not equal to the x-axis direction, rather forming an angle $\sim \Delta/|\Omega|$ from it. In this case the direction of the effective field is given by Eq. (3.34), the Rabi vector is $\Omega = (\Omega, 0, -\Delta)$ and the unitary evolution expressed according to Eq. (3.36).

We define this kind of rotation as *controlled evolution* because, in order to realize it experimentally, the microwave field is switched on ($\Omega \neq 0$).

3.4.4 Rotations around z-axis: free evolution

A rotation around the z-axis, instead, is when the Rabi vector is directed along it, thus $\mathbf{n}_\Omega = (0, 0, 1)$. This means that during the evolution the microwave field is

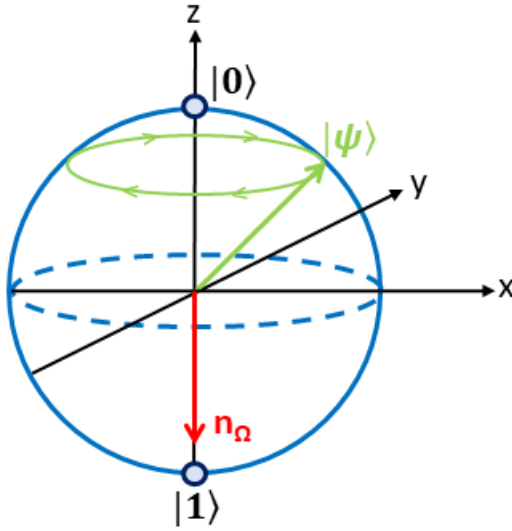


Figure 3.8: Rotations around \hat{z} . Precession of the Bloch vector $|\psi\rangle$ about the effective microwave field directed along $\mathbf{n}_\Omega = (0, 0, n_z)$.

switched off ($\Omega = 0$) and only the presence of detuning drives it. In this case, depending on the initial state, the Bloch vector of the system turns around the Rabi vector $\Omega = (0, 0, -\Delta)$ into a plane parallel to the equator (as shown in Fig. 3.8). The motion will be clockwise or counterclockwise depending on the sign of the detuning and the evolution operator that describes it becomes:

$$\mathcal{U}_{\Omega, \hat{z}} = \begin{pmatrix} \cos\left(\frac{\Delta t}{2}\right) + i \sin\left(\frac{\Delta t}{2}\right) & 0 \\ 0 & \cos\left(\frac{\Delta t}{2}\right) - i \sin\left(\frac{\Delta t}{2}\right) \end{pmatrix} = \exp\left\{i \frac{\Delta t}{2} \sigma_z\right\}. \quad (3.39)$$

It is an instructive exercise to apply this evolution operator to the generic Bloch vector of Eq. (3.16) for a rotation of an angle $\beta = \Delta T$, obtaining:

$$\mathcal{U}_{\Omega, \hat{z}}(\beta)|\psi\rangle = e^{\frac{i\beta}{2}} \left[\cos\left(\frac{\beta}{2}\right) |0\rangle + e^{i(\varphi-\beta)} \sin\left(\frac{\beta}{2}\right) |1\rangle \right]. \quad (3.40)$$

This result clearly shows that, at the end of the evolution, the state acquires a phase given by $\varphi - \beta$, apart from a negligible global phase factor $e^{\frac{i\beta}{2}}$. Furthermore, it is worth noting that the North pole $|0\rangle$ and the South pole $|1\rangle$, lying on the z -axis, are stationary points thus are not affected by this evolution. We define this kind of rotation as *free evolution* because, in order to realize it experimentally, the microwave field is switched off ($\Omega = 0$).

3.4.5 Ramsey sequence

A Ramsey sequence [59] is obtained when our atomic two-level system is subject to two radiation pulses separated by a time-interval much longer than their

duration. Such a combined evolution is obtained with two rotations around the Bloch sphere x-axis, that realizes the two pulses, and a rotation around the z-axis that realizes the waiting time between their application. The resulting quantum mechanical transition probability between the two levels provides interesting properties for precision measurement that will be adopted in this thesis work thus worthy of a discussion.

To understand this sequence, it is useful to introduce the concepts of π -pulses and $\pi/2$ -pulses.

The π -pulse is defined as a pulse made of resonant radiation such that $\Omega t = \pi$. In this case the evolution described in Eq. (3.38) becomes:

$$\mathcal{U}_\pi = \begin{pmatrix} 0 & -i \\ -i & 0 \end{pmatrix}. \quad (3.41)$$

If we apply this matrix to the generic state of a two-level system given in Eq. (3.13), we obtain that a complete transfer of population from one state to the other occurs:

$$|\psi\rangle = c_0|0\rangle + c_1|1\rangle \xrightarrow{\mathcal{U}_\pi} \mathcal{U}_\pi|\psi\rangle = c_0|1\rangle + c_1|0\rangle. \quad (3.42)$$

This operation realizes a *swap*, or population inversion, of the two states.

A $\pi/2$ -pulse is also frequently used in interferometry experiments and it is similarly defined by the condition $\Omega t = \pi/2$. It realizes the evolution:

$$\mathcal{U}_{\pi/2} = \frac{1}{\sqrt{2}} \begin{pmatrix} 1 & -i \\ -i & 1 \end{pmatrix}. \quad (3.43)$$

For an atom initially in state $|0\rangle$, a $\pi/2$ -pulse produces a superposition of states $|0\rangle$ and $|1\rangle$ with equal amplitudes therefore lying on the equator of the Bloch sphere:

$$|\psi\rangle = |0\rangle \xrightarrow{\mathcal{U}_{\pi/2}} \mathcal{U}_{\pi/2}|\psi\rangle = \frac{1}{\sqrt{2}}(|0\rangle - i|1\rangle). \quad (3.44)$$

In the Ramsey sequence, the field is applied in the form of two coherent $\pi/2$ -pulses of the same duration $\tau_P = \pi/2\Omega$ separated by a time interval $T \gg \tau_P$ during which the field is absent, as depicted in Fig. 3.9. Assuming a small detuning ($|\Delta| \ll \Omega$), after the first $\pi/2$ -pulse, a two-level atom prepared in the initial state $|0\rangle$ ends up in the superposition state $(|0\rangle - i|1\rangle)/\sqrt{2}$, with $\vartheta = \pi/2$ and $\varphi = -\pi/2$. This superposition subsequently evolves freely for a time T precessing around \hat{z} on the equatorial plane by an angle $\beta = \Delta T$. Finally the second $\pi/2$ -pulse closes the sequence and the final Bloch state has $\vartheta = \pi - \beta$ and $\varphi = \pi$. The final occupation probabilities $P_{|0\rangle}$ and $P_{|1\rangle}$, of the states $|0\rangle$ and $|1\rangle$ respectively, can be computed by applying the operator $\mathcal{U}_{\pi/2}\mathcal{U}_{\Omega\cdot\hat{z}}(T)\mathcal{U}_{\pi/2}$ to the initial

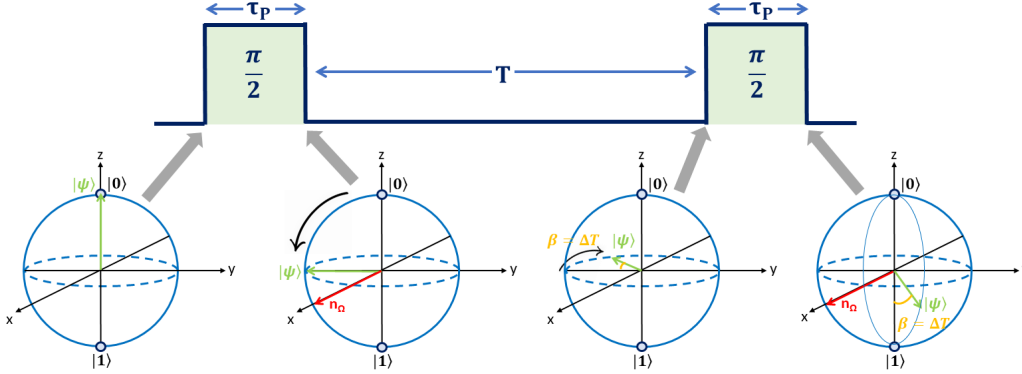


Figure 3.9: *Ramsey sequence*. The Ramsey sequence is here showed in the Bloch sphere description. For a small detuning ($|\Delta| \ll \Omega$), a $\pi/2$ -pulse brings the state $|0\rangle$ in the superposition $(|0\rangle - i|1\rangle)/\sqrt{2}$. A waiting time T , in which the interaction is absent, causes the state to accumulate a phase moving around the equator of an angle $\beta = \Delta T$. The final pulse brings the system in a final Bloch vector having $\vartheta = \pi - \beta$ and $\varphi = \pi$ and transforms the accumulated phase in a measurable population imbalance.

state. The resulting probabilities are:

$$\begin{aligned}
 P_{|0\rangle} &= |c_0|^2 = \sin^2\left(\frac{\Delta T}{2}\right), \\
 P_{|1\rangle} &= |c_1|^2 = \cos^2\left(\frac{\Delta T}{2}\right).
 \end{aligned} \tag{3.45}$$

In Fig. 3.10 we report the signal generated by this sequence for $P_{|1\rangle}$ as a function of the detuning Δ for different T . These oscillations are named *Ramsey fringes*. In the figure we show different fringes according to longer or shorter waiting time T between the two pulses. We can see that the central fringe, the one at resonance, is fixed and that the slopes increase with T .

The Ramsey method is very powerful in determining the detuning Δ with high precision. This is of fundamental importance in the context of the quantum embedding protocol developed in this thesis work where a high degree of control on the rotation angles is required.

In order to determine Δ we tune the apparatus on the more sensitive point that is the side-of-fringe $\Delta T = \pi/2$. Here the fluctuations $\delta P_{|1\rangle}$ of $P_{|1\rangle}$, computed by means of the error propagation formula, are:

$$\delta P_{|1\rangle} = \left| \frac{\partial P_{|1\rangle}}{\partial \Delta} \right|_{\Delta=\pi/2T} \delta \Delta. \tag{3.46}$$

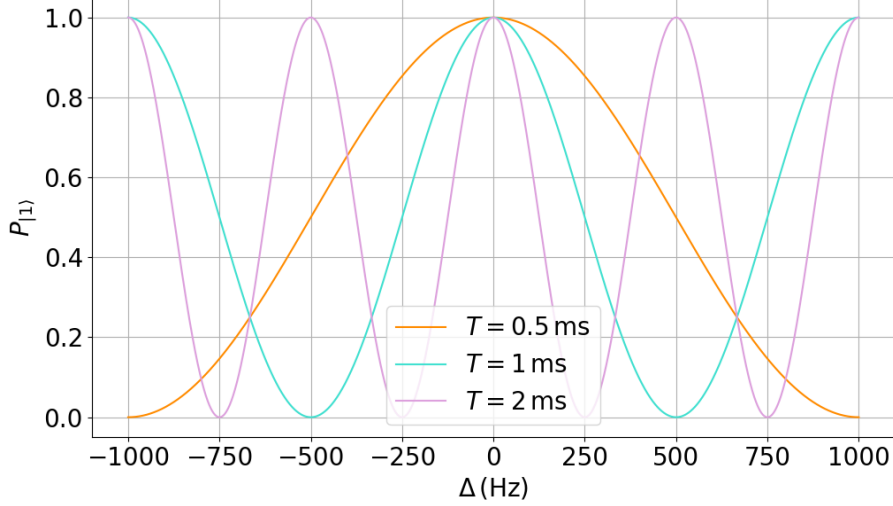


Figure 3.10: *Ramsey fringes*. In this figure, transition probabilities of Eq. (3.45) for the state $|1\rangle$, as a function of the detuning Δ , are reported for different free evolution times T . The oscillations are computed for a Rabi frequency $\Omega = 2\pi \times 60$ kHz. The central peak does not change while its slope increases with T .

Therefore the Ramsey sequence sensitivity in determining the detuning Δ is:

$$\delta\Delta = \frac{\delta P_{|1\rangle}}{\left| \frac{\partial P_{|1\rangle}}{\partial \Delta} \right|_{\Delta=\pi/2T}} = \frac{\delta P_{|1\rangle}}{T/2}. \quad (3.47)$$

It is now clear that a longer waiting time T , also known as the *observation time*, provides higher sensitivity. The latter is only limited by technical noise that can occur affecting $\delta P_{|1\rangle}$ and by the coherence time of the experiment that defines the maximum observation time.

3.5 Experimental implementation on the atomic platform

The aim of this section is to explain how the sequence of rotations of Eq. (3.12), described in Sec. 3.3, realizes the embedding protocol on the atomic platform. The qubit embedder we choose, and to which the embedding sequence will be applied, is the state $|0\rangle \equiv |F = 2, m_F = 0\rangle$ of Fig. 3.11. As shown in the figure, the preparation of the initial state of the experiment is realized by applying an optimally designed radio-frequency pulse [129] to the atoms. It transports the population of level $|F = 2, m_F = +2\rangle$, in which the BEC of typically $\sim 10^5$ ^{87}Rb atoms

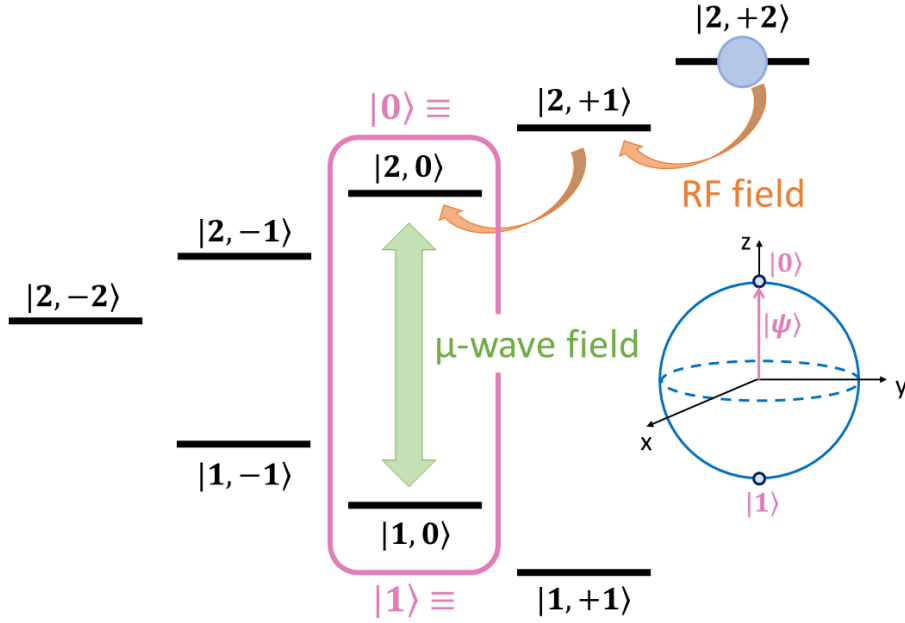


Figure 3.11: *Atomic level scheme for quantum embedding.* In this picture we show the involved levels of ^{87}Rb hyperfine ground state structure. Enhanced in pink is the chosen qubit encoder for the embedding, also shown in its Bloch sphere representation. The embedding sequence starts with all the atoms prepared in the state $|F = 2, m_F = 0\rangle$ by a radio-frequency signal here represented by orange arrows. The green arrow represents the microwave field that drives the dynamical evolution dictated by the quantum feature map.

is experimentally produced in our laboratory as detailed in chapter 2, to the level $|F = 2, m_F = 0\rangle$. The embedding sequence subsequently starts by coupling the magnetically insensitive levels $|0\rangle \equiv |F = 2, m_F = 0\rangle$ and $|1\rangle \equiv |F = 1, m_F = 0\rangle$ by means of an external micro-wave field applied to the atoms. We recall that the microwave antenna, described in Sec. 2.3, is driven by a rectangular wave sent to the three mixers depicted in Fig. 2.15 which control the timing of the output signal switching it off and on. Therefore, by designing the control pulse according to the rotations dictated by the embedding, we let the atoms dynamically evolve consequently.

As we explained in Sec. 3.3, different experimental implementations require to adapt the feature transformation of Eq. (3.12) to the peculiar needs of the realistic scenario. In our case, we design the microwave pulse according to the interaction time necessary to realize a controlled evolution (rotation around \hat{x} of an angle $x_i = \Omega\tau_i$) and a free evolution (rotation around \hat{z} of an angle $\theta_j = \Delta T_j$) given by the embedding sequence. Since the Rabi frequency Ω and the microwave detuning Δ , from the atomic resonance, are set at the beginning of the experimental sequence, our free parameter in reaching the desired rotation angle is the pulse

duration: τ_i for controlled evolution and T_j for free evolution. In particular, we set the amplitude of the pulse (following the procedure described in Subsec. 2.3.1) such that the induced Rabi frequency on the atoms is $\Omega = 2\pi \times 38$ kHz. The detuning of the microwave frequency from the atomic resonance, instead, is set to $\Delta = 2\pi \times 6.57$ kHz. As a consequence the interaction time necessary to perform a rotation $R_x(x_i)$ is $\tau_i = x_i/\Omega$, while the one needed to perform a rotation $R_z(\theta_j)$ is $T_j = \theta_j/\Delta$. Note that to realize the rotation R_z , i. e. a free evolution, the mixers will turn off the microwave signal ($\Omega = 0$) and the atomic Bloch vector will precess around $\mathbf{n}_\Omega = (0, 0, -1)$. Instead, since the parameters Ω and Δ are fixed at the beginning of the evolution and cannot be changed during it, the rotation $R_{x'}$ realized with the microwave switched on is not exactly oriented along \hat{x} . As already explained in the previous section, the induced evolution is a precession of the atomic Bloch vector around the Rabi vector direction that is $\mathbf{n}_\Omega = (\frac{\Omega}{\Omega}, 0, -\frac{\Delta}{\Omega})$. Therefore, the rotation R_x is in our case tilted of an angle $\arctan(\Delta/\Omega)$ respect to the \hat{x} direction. In order to eliminate the error on the rotation angle, that accumulates during a rotation $R_{x'}$, we proceeded as follows. Simulating the overall evolution, we computed, via a python script, the accumulated error in reaching the angle at each rotation step. We then subtracted this value from the angle reached experimentally. In this way we get a correction factor on the evolution duration for each rotation of the embedding sequence. This procedure has led us to the following reduced feature transformation:

$$\Phi(x_1, \theta, x_2) = \{R_{x'}(x_1), R_z(\theta), R_{x'}(x_2)\}, \quad (3.48)$$

after which the final embedded state $|x\rangle$ is reached. You can notice that we used less rotations with respect to the original sequence of Eq. (3.12). Indeed, even though our Ramsey fringes contrast keeps its maximum value till 300 μs of observation time (see Subsec. 3.5.1), we cannot perform a too long evolution for the following reason. The relative error of the rotation angle traveled by the Bloch vector during both the rotations $R_{x'}$ and R_z is equal to the relative error of Ω and Δ respectively. In our case they are of 1% (see Subsec. 3.5.1), meaning that if the interaction time during the free evolution, for instance, doubles so does also the error on the final angle. It is for this reason that we chose to operate with pulses that have an overall duration not exceeding 200 μs . Moreover, a too long interaction time overheats the atom-chip risking to damage it.

According to all these fundamental considerations we have designed 10 different microwave pulses to implement the 10 embeddings sampled to test the protocol as described in Sec. 3.3. They are arranged in two classes of 5 elements each. Therefore, at the end of the experimental sequence, we expect to see the final states clustered in two separated regions of the Bloch sphere as depicted in Fig. 3.5.

The interaction time with microwave switched on (τ_1, τ_2) and with microwave

switched off (T) are reported in Tab. 3.1 for each of the 10 optimally embedded quantum states. After the evolution is ended, we then measure, for every final

State	τ_1 [μs]	T [μs]	τ_2 [μs]
1	19	36	8
2	45	51	7
3	20	37	1
4	20	38	3
5	19	28	3
6	30	47	38
7	32	20	8
8	4	7	35
9	4	25	12
10	7	10	6

Table 3.1: *Embedding parameters for the atomic platform.* Interaction times with the microwave switched on (τ_1, τ_2) and off (T) for the atomic experiment, in order to generate the 10 optimally embedded quantum states.

state, the number of atoms $N_{|0\rangle}$ in the state $|0\rangle$ and the number of atoms $N_{|1\rangle}$ in the state $|1\rangle$ by adopting the absorption imaging technique described in Subsec. 2.2.5. The relative population of the state $|1\rangle$ is retrieved as follows:

$$P_{|1\rangle} = \frac{N_{|1\rangle}}{N_{|0\rangle} + N_{|1\rangle}}. \quad (3.49)$$

From $P_{|1\rangle}$ we get the z -component of the state vector defined as $\langle\sigma_z\rangle = (N_{|0\rangle} - N_{|1\rangle})/(N_{|0\rangle} + N_{|1\rangle})$. Obtaining:

$$\langle\sigma_z\rangle = 1 - 2P_{|1\rangle}. \quad (3.50)$$

To measure also the other components $\langle\sigma_x\rangle$ and $\langle\sigma_y\rangle$ and thus perform a full tomography of the state, we adopt the following strategy. We rotate the reference frame in order to have the x - and y -components both directed along the z -axis. In this way we can measure them using the relation of Eq. (3.50). We experimentally realize it by designing the microwave pulses reported in Fig. 3.12. The pulse depicted in Fig. 3.12 c, is the one that realizes the embedding sequence of Eq. (3.48). At the end of it we directly measure $\langle\sigma_z\rangle$. The pulses in Fig. 3.12 a and 3.12 b, instead, are obtained by adding, at the end of the embedding sequence in Fig. 3.12 c, further rotations (thus interaction times) around the x' - and z -axis. We compute these rotation angles via a simulation of the state vector evolution

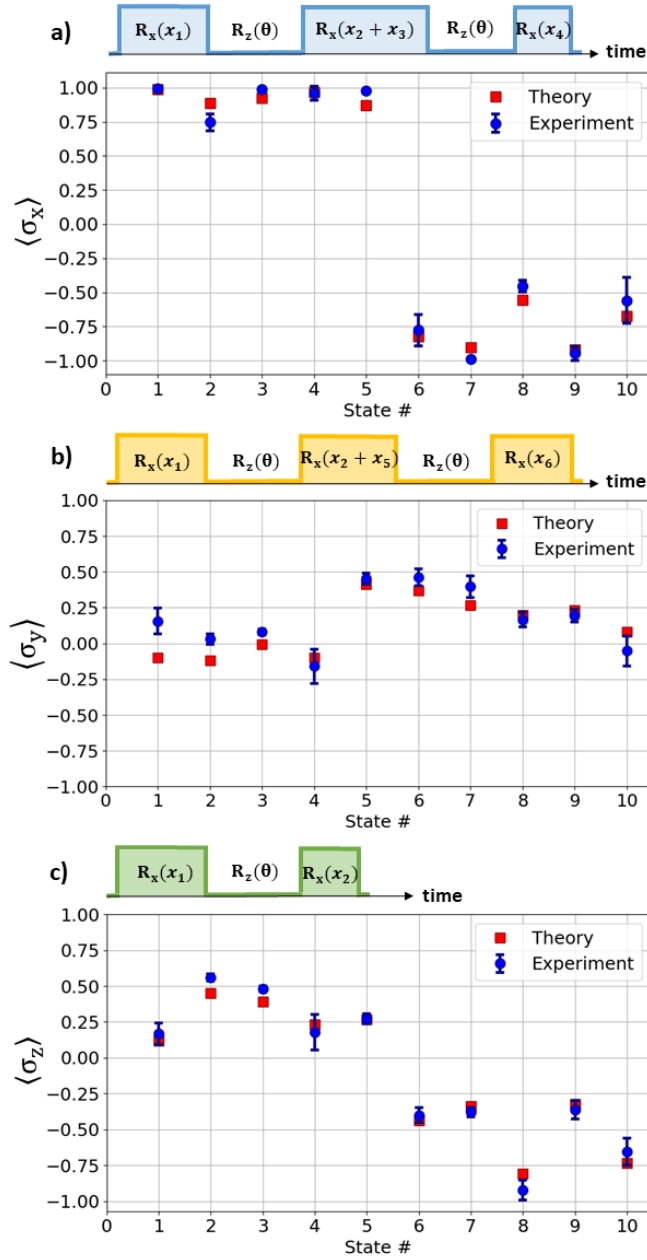


Figure 3.12: Control pulses sequences and embedded states results. In this figure is reported the control pulses sequence used to measure each component of the 10 final embedded states on the Bloch sphere. The performed tomography in order to obtain them is detailed in the text. For each experimental point is represented also the expected one from theoretical prediction. Every experimental sequence is repeated 5 times and the depicted uncertainties are computed via error propagation.

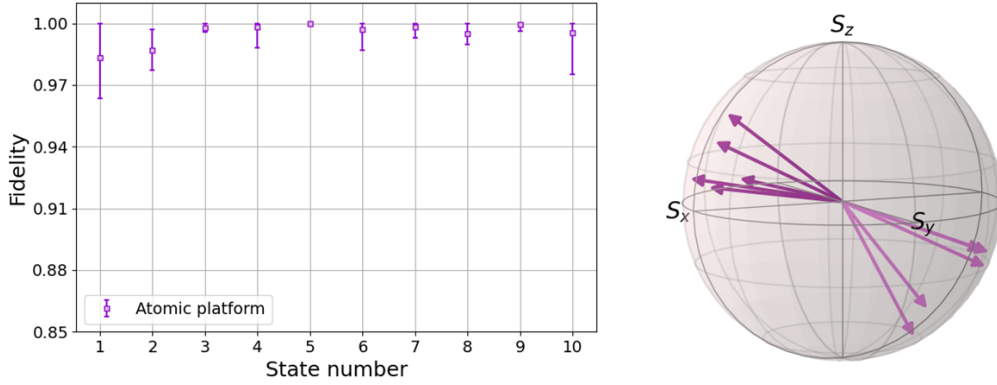


Figure 3.13: *Fidelities and Bloch vectors results for the atomic platform.* Left-hand side: Fidelity between the predicted state and the one reconstructed in the atomic experiment calculated for the 10 validation states. The experimental states are obtained by measuring the three components of the Bloch vector after applying the quantum embedding circuit. The experimental sequence is repeated 5 times and the uncertainty on the fidelity is obtained via error propagation. Note that the error bar for the state 5 is smaller than the marker. Right-hand side: Bloch sphere representation of the 10 embedded quantum states experimentally measured on the atomic platform. The results clearly show a clusterization in two families in accordance with the theoretical prediction reported in Fig. 3.5.

in order to project the $\langle \sigma_x \rangle$ and $\langle \sigma_y \rangle$ components along \hat{z} . In more detail, in order to measure $\langle \sigma_x \rangle$, a rotation along \hat{x}' about an angle x_3 is necessary, followed by a rotation around \hat{z} of an angle θ and a final rotation around \hat{x}' about an angle x_4 . Similarly, for $\langle \sigma_y \rangle$ we compute the rotation angles x_5 and x_6 . Note that the rotation along \hat{z} is always of the same amount θ , the latter, indeed, is the “learned” parameter that has to be kept fixed.

The experimental results obtained for each component of the 10 states are reported in the same Fig. 3.12 below the pulses used to generate them. The error bars are computed via standard deviation from five repetitions of the experimental sequence.

The experimental findings in terms of the Bloch vectors are also showed in Fig. 3.13. Here, a clear clusterization of the reconstructed states can be seen, as we expected from the theoretical predictions reported in Fig. 3.5. The fidelities between the theoretical states and the experimentally reconstructed ones are also reported. Since the evolution that the system undergoes is unitary, the state’s purity is preserved within experimental error. Therefore, we computed the fidelities using the following formula for pure states:

$$\mathcal{F}(\psi_{theo}, \psi_{exp}) = |\langle \psi_{theo} | \psi_{exp} \rangle|^2. \quad (3.51)$$

The measured fidelity is on average better than 0.99, and the error bars have been computed via uncertainty propagation.

3.5.1 Experimental limits of the atomic platform

The experimental realization of the embedding protocol with atoms is fundamentally limited by the following two factors. One is the *accuracy* with which we measure both the Rabi frequency and the radio-frequency detuning, values that we set at the beginning of the experimental sequence. Another is the *stability* in time of these frequency values.

In order to have an estimate of the accuracy, we performed measurements of Rabi oscillations and Ramsey interferometer up to a duration of 300 μs . The latter is a duration much longer than that of any of the embedding sequences. This has led to a measure of $\Omega = 2\pi \times 38.89(2)$ kHz and $\Delta = 2\pi \times 6.57(4)$ kHz, respectively. The uncertainties $\delta\Omega_{fit} = 2\pi \times 0.02$ kHz and $\delta\Delta_{fit} = 2\pi \times 0.04$ kHz, are computed by the fitting error.

To estimate the stability of our system, instead, we performed a measurement of the *Allan variance* [96] of the Rabi frequency and of the resonance frequency. The Allan variance (or Allan deviation) is the most often used tool for the time-domain characterization of oscillators. It is defined as the expectation of the two-sample variance, i.e. the classical variance of Eq. (3.53) for $N = 2$. The time-domain average \bar{y} of a variable y , for $k = 1, \dots, N$, is defined as:

$$\bar{y}_k(\tau) = \frac{1}{\tau} \int_{k\tau}^{(k+1)\tau} y(t) dt. \quad (3.52)$$

Given N samples $\bar{y}_k(\tau)$, the classical variance is:

$$\sigma_y^2 = \frac{1}{N-1} \sum_{k=1}^N [\bar{y}_k - \langle \bar{y} \rangle_N]^2, \quad (3.53)$$

where we denote with $\langle \rangle_N$ the average of N values. The Allan variance is thus defined as the mathematical expectation \mathbb{E} of the classical variance for $N = 2$:

$$\sigma_y^2(\tau) = \mathbb{E} \left\{ \frac{1}{2} [\bar{y}_{k+1} - \bar{y}_k]^2 \right\}. \quad (3.54)$$

It is assumed that the two samples \bar{y}_{k+1} and \bar{y}_k are contiguous in time. If the samples $\bar{y}_k(\tau)$ are not contiguous, then a correction is necessary, which depends on the noise type. In practice, the statistical expectation is replaced by the simple mean. Given a string of M contiguous samples $\bar{y}_k(\tau)$, we have $M - 1$ differences $\bar{y}_{k+1} - \bar{y}_k$. Thus the measured Allan variance is:

$$\sigma_y^2(\tau) = \frac{1}{2(M-1)} \sum_{k=1}^{M-1} (\bar{y}_{k+1} - \bar{y}_k)^2. \quad (3.55)$$

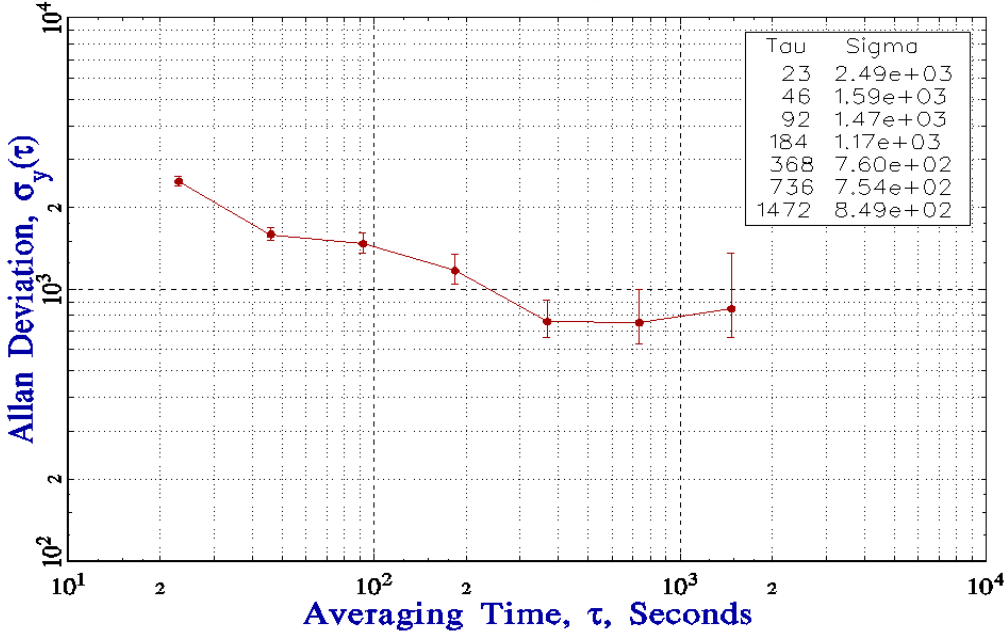


Figure 3.14: *Rabi frequency stability: Allan deviation.* The values reported have been computed via the frequency stability analysis program Stable32 [97]. The analysis is the result of an overall number of frequency measurements of 390, performed for a total time of three hours. The chosen averaging time between two contiguous measurement is 23 s, corresponding to the duration of one BEC experimental sequence.

This quantity estimates the stability due to noise processes and not to that of systematic errors or imperfections that can occur. It compares the variance of a first measurement with the subsequent one for an averaging time τ .

We measured the Allan variance of the Rabi frequency as follows. We applied on the atoms a microwave $\pi/2$ -pulse of duration $\tau = \pi/(2\Omega)$, that is $2\pi \times 6.47 \mu\text{s}$, and measured the relative population $P_{|1\rangle}$. We repeated the same measurement for a total time interval of three hours. The averaging time between two contiguous measurements is of 23 s, that is the duration of one BEC experimental cycle after which a new BEC is created. In complete analogy with the discussion in Subsec. 3.4.5, for each $P_{|1\rangle}$, we then computed the sensitivity of the Rabi frequency at $t = \tau = \pi/2\Omega$ respect to the relative population fluctuations $\delta P_{|1\rangle}$, getting:

$$\delta\Omega = \frac{\delta P_{|1\rangle}}{\left. \frac{\partial \delta P_{|1\rangle}}{\partial \Omega} \right|_{\tau=\pi/2\Omega}} = \frac{\delta P_{|1\rangle}}{\tau/2}. \quad (3.56)$$

The obtained values of $\delta\Omega$ were fed into the Stable32 Frequency Stability Analysis Program [97] getting the results reported in Fig. 3.14.

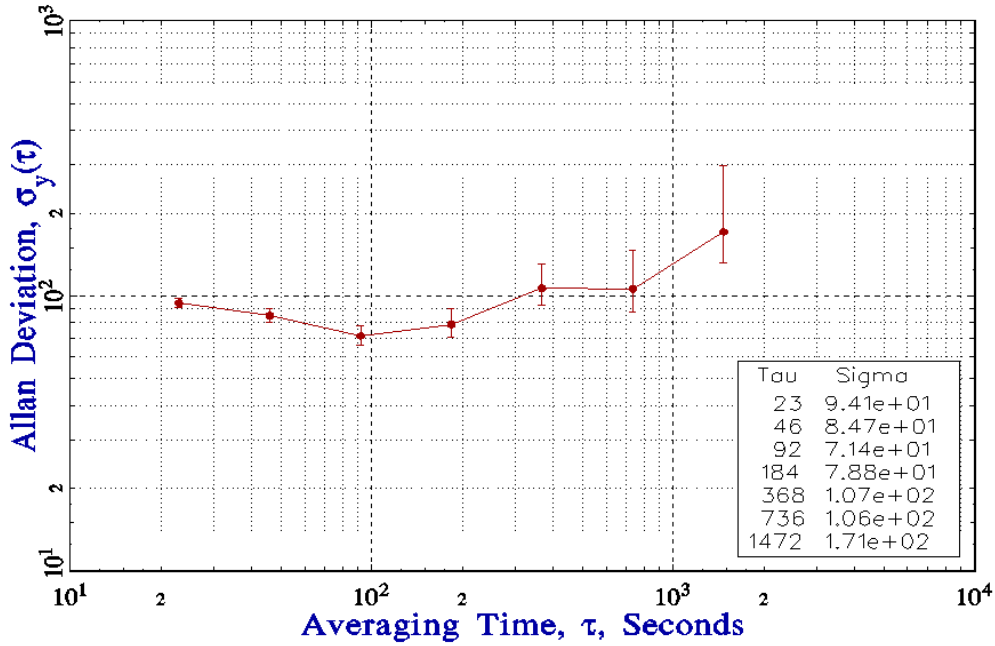


Figure 3.15: *Detuning stability: Allan deviation.* The values reported have been computed via the frequency stability analysis program Stable32 [97]. The analysis is the result of an overall number of frequency measurements of 390, performed for a total time of three hours. The chosen averaging time between two contiguous measurement is 23 s, corresponding to the duration of one BEC experimental sequence.

To measure the stability of the detuning frequency, thus its Allan variance, we adopted a similar strategy. This time applying to the atoms the Ramsey sequence described in Subsec. 3.4.5 to measure the interferometer sensitivity reported in Eq. (3.47). We applied the sequence tuning the apparatus on the more sensitive point that is the side-of-fringe $\Delta T = \pi/2$ and setting an observation time of $T = 300 \mu\text{s}$. At the end of the sequence we measured the relative population $P_{|1\rangle}$. We repeated the same measurement for a total time interval of three hours and with an averaging time of 23 s. Inserting the obtained $\delta\Delta$ into the Stable32 program, we get the results reported in Fig. 3.15 for the Allan variance. Observing both figures for Rabi and Ramsey sequences, we can see that at very short observation times, the Allan deviation is high due to noise. At longer τ it decreases because the noise starts to be averaged out. But at still longer τ , the Allan deviation starts increasing again, suggesting that the frequency under investigation is gradually drifting. This investigation has allowed us to understand that the major source of instability in our system is given by the Rabi frequency, even though the resonance frequency starts drifting earlier. They are presumably due to microwave power fluctuations for the Rabi frequency and magnetic field fluc-

tuations for the detuning from resonance.

These results have allowed us to estimate a fluctuation of $\delta\Omega_{Allan} = 2\pi \times 1.5$ kHz for the Rabi frequency and of $\delta\Delta_{Allan} = 2\pi \times 71$ Hz for the detuning. These last are evaluated on an averaging time of 115 s corresponding to the time needed for five repeated measurement of each embedded state.

The overall uncertainty that takes into account both our accuracy and stability analysis, is thus $\delta\Omega = \sqrt{\delta\Omega_{fit}^2 + \delta\Omega_{Allan}^2}$ for the Rabi frequency and $\delta\Delta = \sqrt{\delta\Delta_{fit}^2 + \delta\Delta_{Allan}^2}$ for the detuning. This reflects, via error propagation, on the uncertainty on the component σ_z of the final embedded states as:

$$\delta\sigma_z = \left| \frac{\partial\sigma_z}{\partial\Omega} \right| \delta\Omega + \left| \frac{\partial\sigma_z}{\partial\Delta} \right| \delta\Delta, \quad (3.57)$$

similarly on the other components σ_x and σ_y . From our simulation of the experiment, we numerically compute the value of the partial derivatives for a small increment. The latter, together with the findings of the Allan variance, let us expect an error of $\delta\sigma_z = 0.1$ on the components of the final Bloch vector. A value that has been confirmed from the experimental results in Fig. 3.12.

3.5.2 Rotations around non-orthogonal axes

In our quantum embedding implementation on the atomic platform, we investigated a possible experimental solution to the problem of rotations around non-orthogonal axes that we encountered. The solution we suggested is to perform the embedding sequence in a rotated frame defined by the following Rabi vector directions:

$$\begin{aligned} \hat{x}'' = \mathbf{n}_\Omega &= \left(\frac{1}{\sqrt{2}}, 0, \frac{1}{\sqrt{2}} \right), \\ \hat{z}'' = \mathbf{n}_\Omega &= \left(-\frac{1}{\sqrt{2}}, 0, \frac{1}{\sqrt{2}} \right). \end{aligned} \quad (3.58)$$

These directions are orthogonal and can be achieved by tuning our apparatus such that the value of the detuning is equal to that of the Rabi frequency, thus realizing a rotation around the axis \hat{x}'' . By setting the detuning equal and opposite to the Rabi frequency, instead, we can realize a rotation around the \hat{z}'' axis. The new frame is depicted in Fig. 3.16. In this way the non-orthogonality problem is overcome.

The embedding sequence can be transferred in the new frame by a simple transformation. The change of reference, indeed, is a rotation around the \hat{y} axis of an

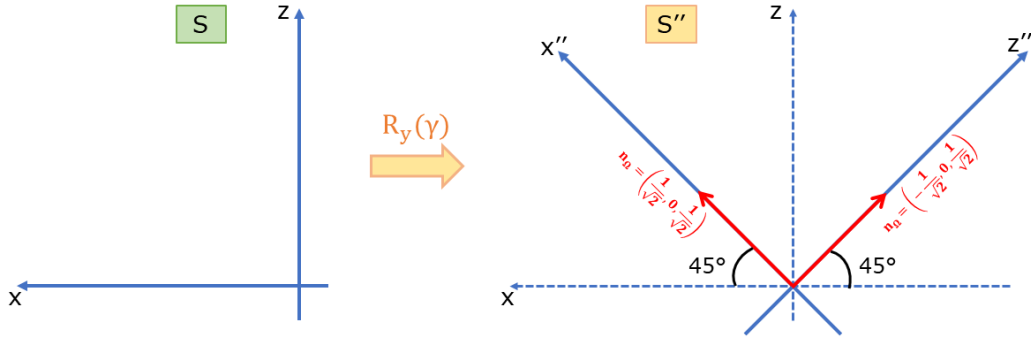


Figure 3.16: *Quantum embedding in the rotated frame.* The embedding sequence can be transferred in a rotated frame about $\gamma = 45^\circ$ around the \hat{y} axis. It can be easily experimentally implemented by setting the Rabi frequency value once equal and once equal and opposite to the detuning frequency of the microwave field from resonance. Thus realizing the rotation axes \mathbf{n}_Ω shown in figure.

angle of $\gamma = 45^\circ$. The matrix that realizes it is:

$$R_y(\gamma) = \begin{pmatrix} \cos \gamma & 0 & \sin \gamma \\ 0 & 1 & 0 \\ -\sin \gamma & 0 & \cos \gamma \end{pmatrix}, \quad (3.59)$$

according to which, the new coordinates are:

$$\begin{aligned} x'' &= \frac{x + z}{\sqrt{2}}, \\ y'' &= y, \\ z'' &= \frac{-x + z}{\sqrt{2}}. \end{aligned} \quad (3.60)$$

From these transformations we can retrieve the expressions that link the Bloch vector's spherical coordinates ϑ and φ with the new coordinates in the rotated reference frame. They are:

$$\begin{aligned} \vartheta'' &= \arccos \left(\frac{-\sin \vartheta \cos \varphi + \cos \vartheta}{\sqrt{2}} \right), \\ \varphi'' &= \text{atan2}(y, x), \end{aligned} \quad (3.61)$$

where $y = \sin \vartheta \sin \varphi$ and $x = (\sin \vartheta \cos \varphi + \cos \vartheta)/\sqrt{2}$.

The corresponding microwave pulse to be designed will have equal positive and negative amplitude, and the microwave will always be turned on during the whole evolution. This solution could be convenient in terms of the speed of the

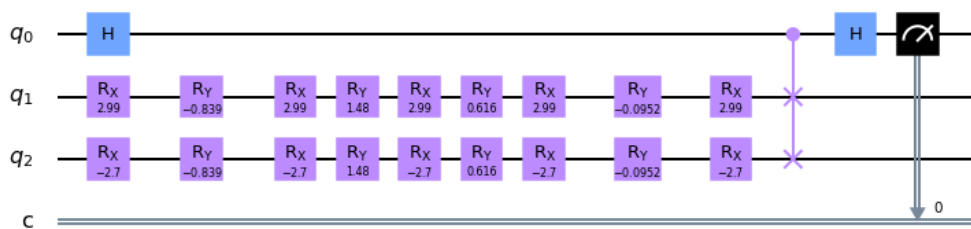


Figure 3.17: *Quantum circuit for the superconducting platform.* A quantum processor trains the circuit shown in figure. After the embedding sequence has been performed through the showed rotations, a C-SWAP gate computes the overlap between the two embedded qubits q_1 and q_2 .

overall dynamics, that is increased using such a high detuning. In addition to the fact that no correction factors have to be computed. It is, however, experimentally challenging to achieve the condition in which Ω and Δ are equal. Therefore, a correction factor that accounts for this fact must be considered. Furthermore, the final tomography will require the design of additional microwave pulses to project the three Bloch vector's components in the original reference frame. The two approaches are substantially equivalent so one can choose the one that better fits the experimental setting.

3.6 Superconducting and photonic platforms results

Different platforms, however, do not necessarily have the same features and constraints. We evidence this, by taking as an example the case of the superconducting chip of Rigetti [94] named Aspen-8. It is composed by a lattice of 30 superconducting qubits in a ladder-like configuration. The qubits are controllable by the action of single and two-qubit gates giving this platform all the characteristics of an universal quantum computer. We thus use this platform to deploy again the same embedding of Eq. (3.12) but on a completely different device with different noise profile and constraints. Using Rigetti's cloud service, each circuit, shown in Fig. 3.17, is sampled 2000 times for each of the 100 data-points necessary to build the Gram matrix. As shown in Fig. 3.19, the Gram matrix (even if it is sensibly noisier than our other tests) clearly exhibits the separation boundary between the two classes. The advantage of this experiment is that it could be performed without the need of an *ad hoc* laboratory; it has been carried out remotely by just reserving some time on the Rigetti system and programming it [95]. The entire set of experiments performed on this platform has taken a total time of around

5 minutes to run.

It is also of interest to perform the quantum embedding with “flying” qubits i.e. photons. Thus, we have also investigated quantum embedding in an optical experiment by generating photon-pairs at the degenerate wavelength 810 nm via parametric down conversion realizing a heralded single-photon source. In particular, the degenerate 810 nm photon-pairs are generated from a 50 mW CW laser at 405 nm through Type I spontaneous parametric down conversion using a 3 mm BBO crystal. Both photons are filtered with band-pass filters (FWHM = 7.3 nm) and single mode fibers. One photon acts as a trigger and is directly coupled to an Avalanche Photodiode Detector (APD), while the other undergoes the embedding transformation as follows. The input state of the photons is set to horizontal polarization direction $|H\rangle$ and then the embedding is performed by applying a single unitary:

$$\mathcal{U}(\phi; \mathbf{n}) = \cos\left(\frac{\phi}{2}\right) \sigma_0 - i \sin\left(\frac{\phi}{2}\right) (\mathbf{n} \cdot \boldsymbol{\sigma}), \quad (3.62)$$

where $\mathbf{n} = (n_x, n_y, n_z)$ denotes the associated rotation axis. The embedding parameters dictating the rotation for each of the 10 states are reported in Tab. 3.2.

This alternative approach of constructing the embedding in the form of a fea-

State	ϕ [rad]	n_x	n_y	n_z
1	0.668	0.667	0.143	0.731
2	1.986	-0.423	0.460	-0.781
3	2.111	-0.510	0.379	-0.772
4	2.408	0.619	0.240	0.748
5	1.301	-0.405	0.914	0.034
6	4.258	0.418	0.908	-0.006
7	4.367	0.247	0.969	0.026
8	3.549	-0.475	0.847	0.239
9	4.379	0.197	0.980	0.036
10	3.762	-0.433	0.877	0.208

Table 3.2: Embedding parameters for the photonic platform.

sible unitary is more suited to photonic experiments. On one hand, this scheme requires superior controllability of the system, since we cannot choose the rotation axis in advance. On the other hand, using only a one-shot embedding instead of a step-by-step approach is a significant simplification.

For photon polarization qubits, rotations in the form of Eq. (3.62) are conveniently performed by means of a series of three wave plates: a quarter wave

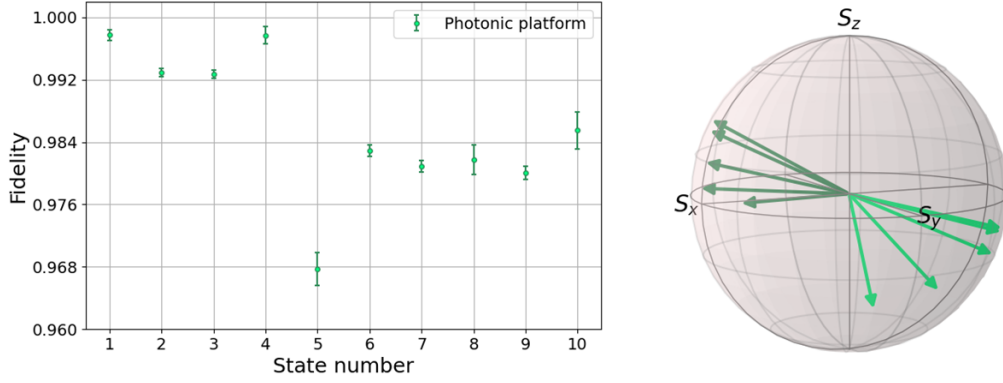


Figure 3.18: *Fidelities and Bloch vectors results for the photonic platform.* Left-hand side: Fidelity between the predicted state and the experimentally reconstructed one in the photonic experiment, obtained by quantum state tomography after applying the quantum embedding circuit, calculated for the 10 validation states. Right-hand side: Bloch sphere representation of the 10 embedded quantum states experimentally measured on the photonic platform. The results clearly show a clusterization in two families in accordance with the theoretical prediction reported in Fig. 3.5.

plate (Q1), a half wave plate (H2) and a second quarter wave plate (Q3), whose angles are associated to the parameters ϕ and \mathbf{n} as follows:

$$\begin{aligned}
 \theta_{Q1} &= \frac{1}{2} \left[-\arctan\left(\frac{n_z}{n_x}\right) - \arctan\left(n_y \tan\left(\frac{\phi}{2}\right)\right) \right], \\
 \theta_{H2} &= \frac{1}{2} \left[-\arcsin\left(n_x \sqrt{\frac{n_z^2}{n_x^2} + 1} \sin\left(\frac{\phi}{2}\right)\right) - \arctan\left(\frac{n_z}{n_x}\right) \right], \\
 \theta_{Q3} &= \frac{1}{2} \left[-\arctan\left(\frac{n_z}{n_x}\right) - \arctan\left(n_y \tan\left(\frac{\phi}{2}\right)\right) \right].
 \end{aligned} \tag{3.63}$$

This is a standard approach, relying on the availability of reliable hardware components, at the cost of losing a direct mapping of each term in the sequence of Eq. (3.12) into a physical object.

Verification of the outputs is carried out by means of quantum state tomography, operated by a further half waveplate/quarter waveplate sequence and a polarizer. It is then performed by collecting coincidence counts in correspondence of the projections along the polarization directions Horizontal, Vertical, Diagonal, Anti-diagonal, Right-circular and Left-circular. For each state, approximately 20000 coincidence events are collected, distributed among the six projectors. The reconstructed Bloch vectors are reported in Fig. 3.18. The two main sources of imperfection are the limited accuracy in the setting of the wave-plate axis ($\pm 1^\circ$ for the encoding plates, $\pm 0.25^\circ$ for the tomography plates), and deviations of the

imparted phase shifts from the target values $\pi/2$ or π . Despite these deviations, clustering of the states in two classes is clearly observed. Once again the fidelity between the experimental results and the theoretical predictions, also shown in Fig. 3.18, is on average above 0.96 which for one qubit accounts for a more than satisfactory agreement. Uncertainties have mainly statistical origin, due to fluctuations in the number of collected counts. In order to account for those, we have performed a Monte Carlo routine, simulating 300 experiments: in each of them, counts are generated by bootstrapping on the observed values, assuming Poissonian statistics, as customary. The uncertainty on the fidelity is thus evaluated as the standard deviation of the fidelities with the target state observed in the Monte Carlo replicas.

3.7 Discussion & conclusions

The Gram matrices reported in Fig. 3.19 reveal that all the architectures we have considered indeed give satisfactory results in realizing the quantum embedding. To make this observation more quantitative, we here provide a theoretical bound, based on the observed fidelities, for the number N_{max} of different classes and/or different points that can be embedded on a single qubit. Our bound is derived from geometrical constraints of the embedding on the Bloch sphere. The minimal assumption we can make for the embedding to be successful is to avoid overlapping between different classes. These are associated to distinct spherical sectors defined by its central angle ϑ ; in our example, the two sectors correspond to two separate halves of the sphere ($\vartheta = \pi$). By simple geometrical arguments, the surface occupied by a single spherical sector is given by $2\pi [1 - \cos(\vartheta/2)]$. Since we want the sectors to be non-overlapping, and the total available surface of our Bloch sphere is 4π , we can formulate a geometrical constraint considering the number of classes N as follows:

$$2\pi N \left[1 - \cos\left(\frac{\vartheta}{2}\right) \right] \leq 4\pi. \quad (3.64)$$

This equation thus computes the tightness of the embedding given a number N of classes to embed.

These methods also provide an upper bound on the data set which can effectively be embedded. We use the fidelity \mathcal{F} between the experimental states and the corresponding targets. While the ideal state is associated to a unique direction in the Bloch sphere, accounting for the imperfections of the actual prepared state leads us to consider a spherical surface $2\pi(1 - \mathcal{F})$ as the proper geometric

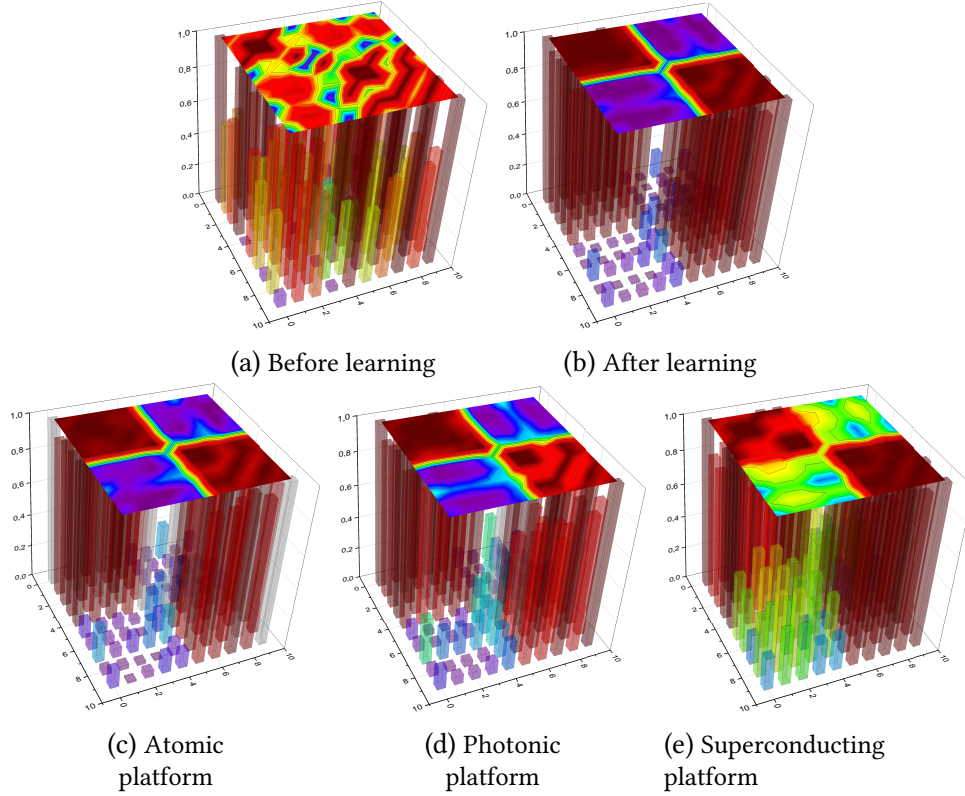


Figure 3.19: *Gram matrices results of quantum embedding.* Gram matrix representation of the embedded quantum states as predicted by theory before learning in (a) and after learning in (b). The experimental findings for all the explored platforms are also reported below in (c), (d) and (e). All the architectures we considered show satisfactory results, indeed, the two classes are clearly distinct. However, the results of the atomic platform prove that, respect to the others, ultra-cold atoms appear the more promising candidates for such implementations.

measure. Thus, the maximum number of points allowed is:

$$N_{max} \leq \frac{4\pi}{2\pi(1 - \mathcal{F})}. \quad (3.65)$$

Our experiments demonstrate that a fidelity exceeding 0.9 can be routinely achieved on all platforms we have explored. This determines a maximal embedding capacity $N_{max} \simeq 20$ as a conservative estimate. This reasoning can be obviously generalized to the 2^n -dimensional hypersphere in the case of multi-qubit embedding.

Our experimental investigation demonstrates how quantum embedding techniques may suit radically different approaches to qubit encoding and manipulation by pulses as for cold atom, by quantum logic circuits as for the Rigetti machine, or by compiled operations as for photons. Such a versatility shows

promises for future interconnected systems on hybrid architectures, with specialized hardware for storage, processing and distribution of quantum data. Finally, the potential advantages of representing classical data on quantum systems include not only the possibility to simplify a classification problem as experimentally demonstrated in this work, but also the ability to speed up any processing of the classical data such as, among the others, the quantum parallelism to search through a database, feature extraction, image segmentation, and edge detection. Indeed, combining quantum machine learning and quantum image processing is expected to allow to potentially solve *real world* problems that are very challenging via classical supercomputers, especially in the case of large volumes of data in various domains ranging from sociology to economy, from geography to bio-medicine.

4 | Reversing time with ultra-cold atoms for quantum *undo* operations

In our everyday experience, *empirical-knowledge* suggests that *time* goes on according to the inevitable fact that the events have a proper spatial and temporal relation. The scientific counterpart of our interpretation of time coming from the familiar experience of growing or becoming, is made by the concept of *entropy* which provides the *arrow of time*. The latter comes from the second law of thermodynamics which led Arthur S. Eddington to the definition of a time's arrow in 1928 [98], thus establishing the fundamental difference between past and future. According to it, the progress of time towards the future, indeed, follows the direction of more and more random elements in the state of the world. In the direction where the random elements decrease, instead, the arrow of time is pointing towards the past. It follows the fundamental statement that *the introduction of randomness is the only thing which cannot be undone*. According to this law, it is too *improbable* that at a certain point a universe evolves backwards hence developing in the opposite direction of our own system. However, this statement is not in conflict with the primary laws for which the fundamental microscopic equations of motion are symmetrical with respect to time-reversal transformation. There are some conditions for which no increase in the random elements can occur. Indeed, if we are able to isolate a portion of space such that no energy can enter or leave and boundary effects are compensated, then the time's arrow gets lost. This is a very distinctive property that is typical of “*a fortuitous concourse of atoms*”, in Sir Eddington words, a *much-prized rarity* in thermodynamical equilibrium. Precisely it means that, at thermodynamical equilibrium, the random elements have reached their limit of increase and have become steady. The arrow of time does not know anymore where to point. However, it does not mean that this region of space is *timeless*: *the atoms vibrate as usual like little clocks; by them we can measure speeds and durations; time is still there and retains its ordinary properties, but it has lost its arrow; like space it ex-*

tends, but it does not “go on”. Time reversal in such systems is therefore possible, in the sense that in an infinite time all the configurations of the phase space of the system will be explored.

In this regard, I here report a time inversion experiment realized on a BEC of ^{87}Rb atoms, by driving its dynamical evolution forth and back along several paths in its Hilbert space. A BEC can be considered as a very well isolated system at thermal equilibrium, however interacting with an external coherent driving field. In our case, indeed, irreversibility comes into play in the sense of the unavoidable decoherence time of our condensate. The latter imposes a temporal limit to its evolution thus exhibiting entropy production. The procedure we propose is therefore an entropy rectification method that makes use of optimal control strategies successfully applied in our context in several experimental implementations. In particular, we want to apply our findings for the practical realization of quantum *undo* operations in quantum technology contexts, ranging from quantum computing to quantum communications. By means of the *undo* command, indeed, one can time-reverse the last performed operation on a quantum computer so as to perfectly restore a condition in which an arbitrary new operation, chosen by the external user, can be then applied. Moreover, I will show that we can further generalize this concept, by applying the *undo* command also for the reversing of a quantum operation in a generic instant of the system’s past, and thus not only in the last time instant.

The chapter is organized as follows. In Sec. 4.1 I introduce the *undo* operation in the context of quantum computers applications, highlighting how the proposed solution can be adapted to a generic experimental platform. In Sec. 4.2 both the quantum system Hamiltonian and the optimization protocol are described, by explaining the way the driving field is optimally designed by means of the dCRAB algorithm. In Sec. 4.3 I present all the experiments we realized to test time-reversal transformations with ultra-cold atoms, to be seen as the proof of principle of *undo* operations in quantum regimes. Finally, Sec. 4.4 concludes the chapter, by discussing the relevance of our experimental results and providing for them a thermodynamic interpretation whereby the employed optimal control strategy corresponds to an entropy rectification procedure.

The results reported in this chapter are under preparation:

- Ivana Mastroserio, Stefano Gherardini, Cosimo Lovecchio, Tommaso Calarco, Simone Montangero, Francesco S. Cataliotti, and Filippo Caruso, *Experimental realization of optimal time-reversal on an atom-chip for quantum undo operations*.

4.1 Undo operations on a quantum computer

The *undo* command allows to reverse a calculation or, more in general, an operation that has been performed in a past step of a complex computational routine. Specifically, the *undo* command is a basic tool to be addressed in all those computational processes, in which the external user may need to proceed step by step thus visualizing the result of each operation. This already holds in traditional/classical (in the sense of “not quantum”) computer or computing systems managed by a high-level interface (as e.g. an operating system) where such a command is a requirement that is practically taken for granted [99, 100].

In quantum platforms for quantum computing, the *undo* command is expected to need more onerous procedures with respect to the classical case. So far, procedures carrying out time-reversal transformations [101] have been implemented in specific settings [102, 103], however without employing universal features that might be valid in a general quantum technologies context. Indeed, in doing this, two main challenges have to be still addressed: one from the procedural side, ensuring high-performance, and the other from a technological point of view.

The first challenge concerns the establishment of an optimal procedure for the realization of quantum *undo* operations. For instance, by reducing as much as possible the execution error and requiring a moderate computation load depending on the experimental devices at disposal. In real experiments, indeed, one can often implement only a small set of operations, due to practical limitations, experimental imperfections and few resources. Moreover, such an optimal procedure has to be designed to be possibly implemented in a generic experimental platform. The solution to these issues, which we propose, is the use of quantum optimal control (OC) methods introduced for the control of quantum systems dynamics. Quantum OC theory is one of the optimal ways to successfully prepare quantum states and perform desired tasks. The latter are crucial elements in the implementation of quantum-based technologies, ranging from atomic to molecular and optical systems [104–121]. Specifically, in this work we adopt the dressed Chopped Random Basis (dCRAB) optimal control algorithm [122–126] that has been already successfully tested in several experiments involving many-body atomic systems [127–131] thanks to its efficiency and versatility.

The second challenge in designing quantum *undo* operations is to identify what are the key mechanisms and devices without which a time-reversal routine cannot be experimentally realized. As previously mentioned, such OC tools are required to allow for the realization of quantum *undo* operations in a generic experimental platform, and thus not only in a Bose-Einstein condensate as we implemented in this work.

In this context, we theoretically and experimentally exploit the power of dCRAB

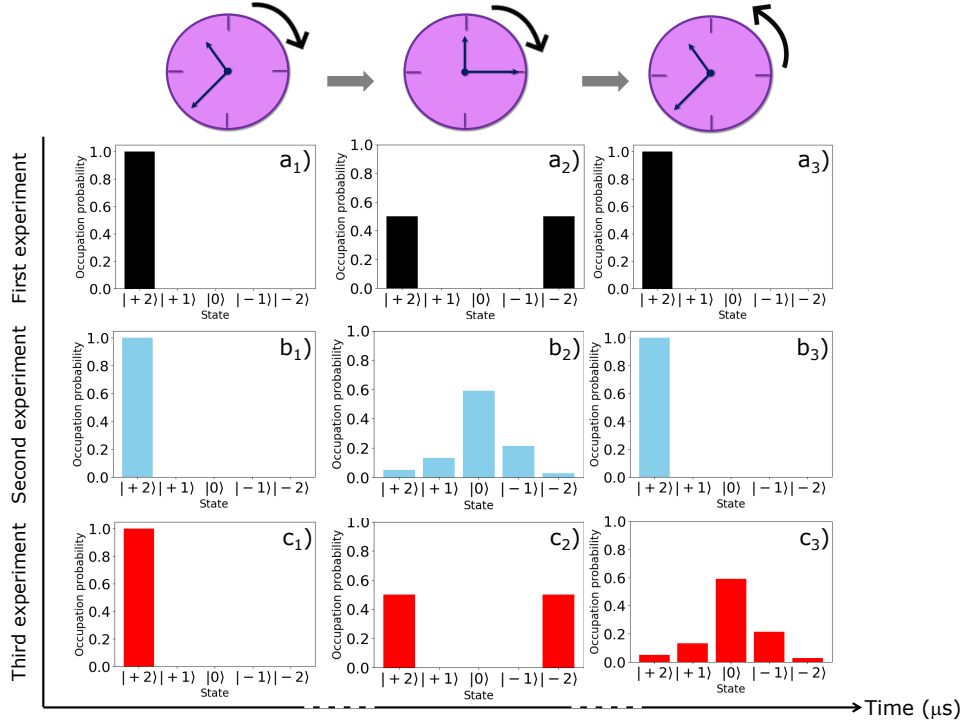


Figure 4.1: Pictorial representation of the realized time-reversal experiments. We prepare a ^{87}Rb BEC in the state $|F = 2, m_F = +2\rangle$ that is the initial state for all the performed experiments; the experiments are respectively denoted as a), b) and c). In the first experiment, the atoms evolve from a₁) towards the state a₂) where their population is equally distributed among the states $|F = 2, m_F = +2\rangle$ and $|F = 2, m_F = -2\rangle$, and then brought back to the initial state $|F = 2, m_F = +2\rangle$ corresponding to the configuration a₃). In the second experiment, the atoms evolve from b₁) towards a state b₂) by using the optimal pulse employed in the first experiment but with a shorter length that belongs to $[10, 100) \mu\text{s}$. Then, the atoms evolve back to the initial state – configuration b₃) – as in the first experiment. Finally, in the third experiment, the forward evolution of the atoms from c₁) to c₂) is the same of that in the first experiment, while in the backward process the system reaches the quantum state c₃) that has been already explored in the second experiment (thus, in its past). It is worth noting that also the latter transformation realizes a quantum *undo* operation, but on a shorter time-scale with respect to the other cases illustrated in the figure. Furthermore, although for illustrative purposes we chose to report in this plot only the populations of the states, we will show in Subsec. 4.3.3 that the state c₃) has the same coherences, within experimental error, of state b₂).

optimal control techniques to successfully perform time-reversal transformations. We invert the dynamical evolution of a very fragile quantum system realized with ultra-cold atoms from an atom-chip device (as summarized in Fig. 4.1). To make an illustrative comparison, we also show the large differences between the results from our experiments and the ones given by inverting, through the addition of a phase term (i.e. a prefactor $e^{i\pi}$), the time-dependence of the exter-

nal driving (radio frequency) field $f(t)$ used to address the atoms. Indeed, even in the absence of external noise (in our case, the system dynamics is to good approximation not affected by noise at least until around $100 \mu\text{s}$), the evolution of a driven quantum system is governed by the Schrödinger equation [132] in which the Hamiltonian operator is generally composed by two distinct contributions: one modeling the inner structure of the system (the atomic Hamiltonian H_0), and the other describing the interaction with external coherent fields, modelled e.g. by the time-dependent function $f(t)$, that steers its dynamics. Hence, leading the system back to its initial state is not simply done by the possible inversion of the time arrow of the driving field, i.e., $f(-t)$, because of the unavoidable presence of the Hamiltonian term H_0 that *always* evolves forward in time. It has been already proven that, in some specific cases, it is possible to exploit the periodicity of the quantum dynamics to retrace part of the evolution or to create an echo of the initial state [133–135]. Specifically, some peculiar time inversion tasks have been demonstrated, such as the reversal of atom-field interaction in a cavity quantum electrodynamics experiment [136] or feedback control-based deterministic reversal of projective measurements on a trapped ion experiment through a quantum error-correction protocol [137]. However, these strategies may be viable if no constraints on the duration of the time-reversal transformations to be implemented are taken into account. For example, in our case using ultra-cold atoms within an atom-chip device (but similarly even in many other atomic, molecular and optical systems) any dynamical transformation is constrained by the well-known decoherence time T_2 [7], which defines the period after which the system loses on average quantum coherence due to the presence of an external field or/and the coupling to external environment. In our experiments, the quantum system dynamics we implemented cannot be longer than around $100 \mu\text{s}$. Also for this reason, the use of OC techniques has been opted for the realization of quantum *undo* operations allowed by time-reversal procedures.

4.2 Physical system and optimization protocol

The experiment is performed on the Bose-Einstein condensate (BEC) of ^{87}Rb realized as detailed in chapter 2. The condensate dynamics is, in this case, driven on the five-fold Hilbert space given by the $F = 2$ rubidium hyperfine ground state. Hence, we assume that the internal state of the atomic system is described at each time t by the 5×5 density matrix $\rho(t)$.

After the creation of the BEC, at the beginning of the system evolution, the atoms are optically pumped in the $|F = 2, m_F = +2\rangle$ sub-level, as pictorially shown in Fig. 4.2. The free evolution of the atoms, within the BEC, is governed by the time-

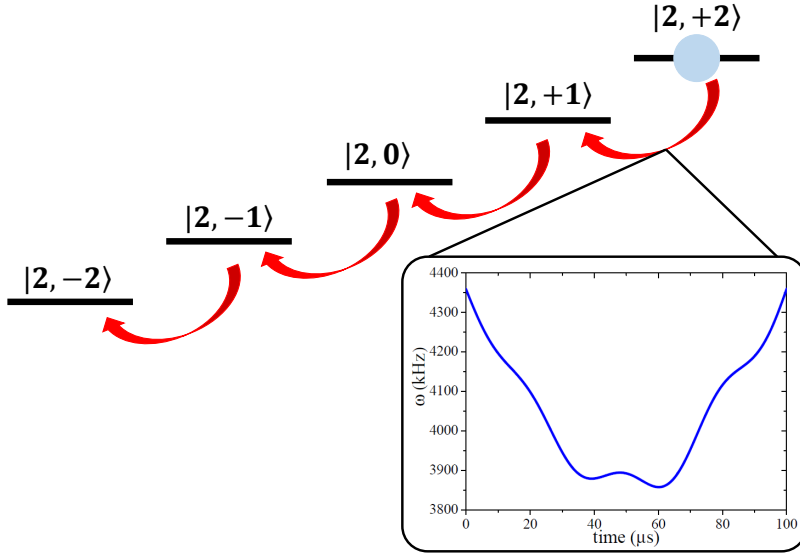


Figure 4.2: Relevant ^{87}Rb atomic energy levels. The whole quantum dynamics in our time-reversal experiments take place in the $F = 2$ hyperfine ground state of a ^{87}Rb Bose-Einstein condensate. The manifold is given by the five possible orientations of a spin-2, energetically separated by means of a homogeneous magnetic field. The atomic cloud is initially prepared in the $|F = 2, m_F = +2\rangle$ quantum state, and subsequently the five neighboring $|F, m_F\rangle$ states are coupled by a quasi resonant radio frequency radiation (depicted by the red arrows). By modulating the latter in time through an optimally designed strategy, the energies of the five sub-levels are effectively “shaken” in order to drive the system forth and back in time. The inset shows an example of optimally prepared pulse, whose frequency $\omega(t)$ typically belongs to the range 1 – 10 MHz.

independent atomic Hamiltonian H_0 that is evaluated via the Breit-Rabi formula [138]. Thanks to the Breit-Rabi formula, indeed, one can quantitatively determine the energies of all different sub-levels for a known magnetic field intensity. In particular, as detailed in Subsec. 2.3.2, for our system the atoms are in the presence of a constant bias magnetic field that we arbitrarily set to 6.179 G. As a result, we obtain the atomic Hamiltonian $H_0 = h \text{diag}(8635, 4320, 0, -4326, -8657)$ kHz, where h is the Planck’s constant, and the elements of the state basis are chosen to correspond to the hyperfine levels from $m_F = +2$ to $m_F = -2$ by ensuring that the reference zero-energy state is $|F = 2, m_F = 0\rangle$ (see Fig. 4.2).

Then, the atomic evolution is driven by means of a quasi resonant radio frequency (RF) field that is produced by micro structured conductors integrated on the atom-chip (again see Subsec. 2.3.2 for the description of the tuning of the experimental parameters). The driving is implemented through a frequency-modulated RF pulse $f(t)$ that couples the five neighboring m_F states and is de-

scribed by the Hamiltonian:

$$H_{RF}(t) = \hbar \begin{pmatrix} -2f(t) & \Omega & 0 & 0 & 0 \\ \Omega & -f(t) & \sqrt{3/2} \Omega & 0 & 0 \\ 0 & \sqrt{3/2} \Omega & 0 & \sqrt{3/2} \Omega & 0 \\ 0 & 0 & \sqrt{3/2} \Omega & f(t) & \Omega \\ 0 & 0 & 0 & \Omega & 2f(t) \end{pmatrix} \quad (4.1)$$

with \hbar reduced Planck constant. By using the rotating wave approximation (RWA) to express the system Hamiltonian, in Eq. (4.1) $f(t) = \partial_t[t\omega(t)]$ where $\omega(t)$ denotes the time-dependent frequency of the driving field. Instead, the coupling Rabi frequency Ω is proportional to the RF field amplitude and in the following will be set to $\Omega = 2\pi \times 60.0$ kHz.

Overall, the total Hamiltonian describing our system is $H(t) = H_0 + H_{RF}(t)$. We may also include in the model a dephasing term by means of super-operators expressed in the so-called Gorini-Kossakowski-Sudarshan-Lindblad (GKSL) form [139] to describe the presence of experimental low-frequency noise on the magnetic bias field and on the RF signal. However, it is worth noting that such noise field starts affecting the dynamics of the quantum system after a time interval of the order of the decoherence time of the BEC, which we have estimated to be around $100 \mu\text{s}$. In this regard, a quantitative analysis is realized in the second set of experiments described in Subsec. 4.3.2.

4.2.1 Radio-frequency modulation with dCRAB

In order to drive the system evolution forth and back in time, the optimal time-dependence of $f(t)$ needs to be determined. This goal is here achieved by minimizing the difference between the final and target quantum states of the atomic evolution, both expressed in terms of the corresponding density matrix ρ . This difference is provided by the error function $\epsilon \equiv \frac{1}{2} \sum_{n=1}^5 |\rho_{n,n}(T) - \widehat{\rho}_{n,n}|$, where T is the length of the control pulse, $\rho_{n,n}(T)$ denotes the ‘final’ atomic population of the n -th sub-level at $t = T$ (i.e., after the control pulse is ended), while $\widehat{\rho}_{n,n}$ is the corresponding target population. Let us note that the error function ϵ , defining the success score of our procedure, can be chosen depending on the experimental or evolution constraints we are facing with. In our case, we chose the simplest experimental way to get the optimal pulse output, i.e., by taking the error function as the mismatch between the target atomic populations and the ones obtained by letting evolve the optimally driven dynamics of the atoms in the BEC.

To minimize the error function ϵ , the time-dependence of the (slowly oscillating) frequency RF control pulse $f(t)$ is optimally modulated by following the prescrip-

tions of the dCRAB method [122–126]. For this purpose, the time-dependent frequency $\omega(t)$ of the driving field is expanded in the standard Fourier basis such that:

$$f(t) = 1 + \sum_{k=-7}^7 A_k (1 + i v_k t) e^{i v_k t}, \quad (4.2)$$

and the optimal values of the expansion coefficients A_k (amplitude of the control function modulation) are determined algorithmically by ensuring that the error function ϵ is minimized. Let us observe that in Eq. (4.2) $v_k = 2\pi k/T$, where k is the index that spans the set of harmonics pertaining to the driving field, with $k = 1, \dots, 7$ [140], and T denotes the length of the control pulse as above. Moreover, also note that the optimization procedure in determining the optimal values of A_k is performed via the subplex variant of the Nelder-Mead algorithm [141]. It is a subspace-searching simplex algorithm for unconstrained minimization of a function¹. Like the Nelder-Mead simplex method it generalizes, the subplex method is well suited for optimizing noisy objective functions. The number of function evaluations required for convergence typically increases only linearly with the problem size, so for most applications the subplex method is much more efficient than the simplex method. The depth of modulation in all the experiments is set to $\Delta\nu = 1.3$ MHz around the central frequency $\nu_0 = 4.323$ MHz. Let us emphasize that our time-reversal protocol operates only on the diagonal elements of the final density matrix $\hat{\rho}(T)$ (reached at the end of the evolution), corresponding to the quantum system populations that we directly measure. In fact, the optimization procedures, which we perform to design the optimal pulses driving the quantum system dynamics, are set not to employ non-diagonal elements of $\hat{\rho}(T)$ that should be necessarily measured by means of a tomography process. In this regard, by making use of the results in Refs. [129, 143] concerning the optimal preparation of quantum states on ^{87}Rb BEC atom-chip-based microtraps (as ours), we implement a preliminary test experiment to tune the values of the setup parameters for accurate state preparation and transfer. Specifically, in this test experiment, we measure the time evolution of the atomic population in each of the five m_F sub-levels during the application of an optimal pulse that brings the quantum system from an initial state, in which the population is equally distributed among the states $|F = 2, m_F = +2\rangle$ and $|F = 2, m_F = -2\rangle$, to a final state where all the population occupies the $|F = 2, m_F = -2\rangle$ sub-level. The experimental results, reported in Fig. 4.3 for illustrative purposes, are in satisfactory agreement with the theoretical predictions obtained by solving the well-known Liouville-von Neumann (differential) equation $\dot{\rho}(t) = -(i/\hbar)[H(t), \rho(t)]$. Finally, before proceeding, let us also observe that whenever a full density matrix reconstruction is performed for additional test experiments (see the next sec-

¹<https://cran.r-project.org/web/packages/subplex/subplex.pdf>

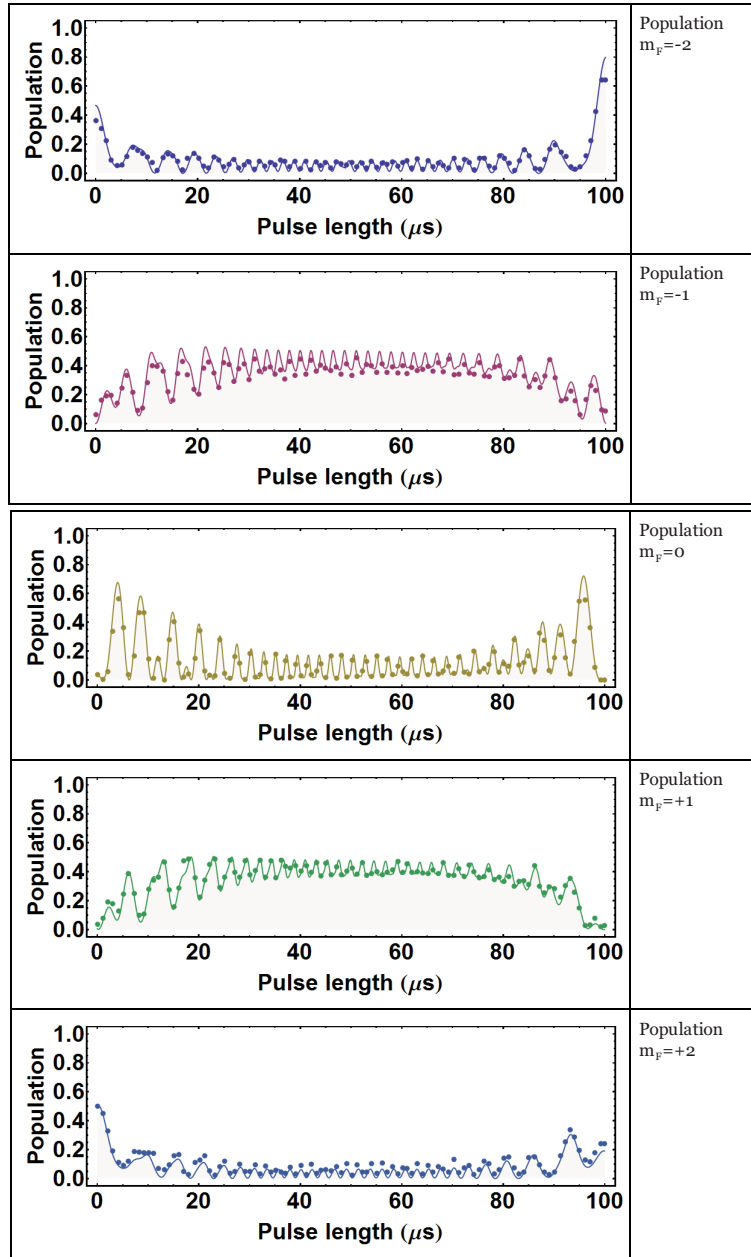


Figure 4.3: *Illustration of an atomic population dynamics.* Time evolution of the five m_F sub-levels, as an effect of the application of the optimal control pulse $f(t)$ to drive the system from an initial state where the population is equally distributed among the states $|F = 2, m_F = +2\rangle$ and $|F = 2, m_F = -2\rangle$, to a final state where all the population occupies the $|F = 2, m_F = -2\rangle$ sub-level. Continuous lines represent the theoretical simulations while the dots are the experimental values, which are the average result of ten experimental repetitions. Error bars, computed via standard deviation, are smaller than the diameter of the points and thus not shown.

tion), the distance between the target and the experimentally measured quantum states, $\widehat{\rho}$ and $\rho(t)$ respectively, is evaluated through the Uhlmann fidelity [142]:

$$\mathfrak{F}(\widehat{\rho}, \rho(t)) \equiv \left(\text{Tr} \sqrt{\sqrt{\widehat{\rho}} \rho(t) \sqrt{\widehat{\rho}}} \right)^2. \quad (4.3)$$

In all the other cases, the accuracy in performing a given operation is assessed by means of the error function, according to the formula $1 - \epsilon$.

4.3 Time reversal experiments

In this work we exploit the dCRAB control techniques to realize three different set of experiments (summarized in Fig. 4.4) to faithfully time-invert the evolution of a quantum system realized with ultra-cold atoms. The proposed strategies are successfully applied along several paths in the system's Hilbert space, where quantum operations can be inverted by using gradually higher level of control in terms of the complexity of the addressed control problems. Moreover, we also aim to illustrate how such techniques allow for the extension of the implemented time-reversal transformations to much more complicated situations, in which performing the backward evolution in a shortest time-scale and/or with accuracy values as high as possible may be crucial. Finally, in order to make a comparison and corroborate our need to employ quantum OC methods, we show how different the outcomes of such experiments are, if one inverts the time-dependence of the external driving field instead of using an optimal driving pulse.

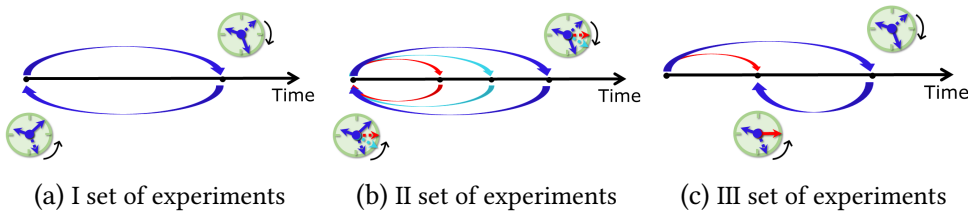


Figure 4.4: *Time reversal experiments.* (a) The atomic evolution is driven forward and backward in time from an initial state to a given target one. (b) The time-reversal of the quantum system evolution is performed along trajectories with gradually shorter time duration. (c) The quantum state of our system is driven back in time to a quantum state that has been already explored in the past.

4.3.1 First set of experiments

In the *first set of experiments* (also see Fig. 4.4a), our aim is to *drive the evolution of our quantum system forward and backward in time from an initial state $\rho(0)$ to a given target one $\widehat{\rho}$ and then back again to $\rho(0)$* . This experiment is two-fold: firstly by time-inverting the driving field $f(-t)$, and secondly by controlling the time-reverse evolution via the optimally designed driving pulse $f_{OC}(t)$, where again the subscript OC stands for ‘optimal control’. As we will show in the following, by comparing the experimental results of both procedures, we will clearly demonstrate that inverting the time-dependence of the driving field, without modifying the time-independent part of the system’s Hamiltonian (H_0), does not bring back the system to its initial state, and thus such a procedure may be a common misconception to get time-reversed quantum dynamics. Conversely, thanks to the use of OC algorithms, one is able to bring the quantum system back to the desired state and restore the initial conditions. The experiment is repeated four times to test the realization of an accurate time-reversal transformation over four different paths in the Hilbert space of the BEC. Specifically, our quantum system is driven – according to the optimal strategy of Ref. [129] – from the initial state $\rho(0)$, such that $\rho_{1,1}(0) = 1$ and $\rho_{k,j}(0) = 0$ for $k, j = 1, \dots, 5$ apart $k = j = 1$ (experimentally, it corresponds to the case where the atomic population occupies the state $|F = 2, m_F = 2\rangle \equiv | + 2\rangle$ as depicted in Fig. 4.2), to the following four different target states:

- i) $\widehat{\rho}_A: \widehat{\rho}_{1,1} = \widehat{\rho}_{5,5} = 0.5;$
- ii) $\widehat{\rho}_B: \widehat{\rho}_{2,2} = \widehat{\rho}_{4,4} = 0.5;$
- iii) $\widehat{\rho}_C: \widehat{\rho}_{1,1} = \widehat{\rho}_{2,2} = 0.5;$
- iv) $\widehat{\rho}_D: \widehat{\rho}_{n,n} = 1/5, \text{ for } n = 1, \dots, 5,$

where for each target all the other elements of ρ are equal to zero. Subsequently, the optimal control pulse $f_{OC}(T)$ (designed as in Subsec. 4.2.1) is applied to the BEC to bring the system back to the initial state $\rho(0)$ according to the two procedures introduced above. In all the analyzed cases, the time duration T of the forward and backward processes is set to $100 \mu\text{s}$, thus entailing a total system evolution of $200 \mu\text{s}$. To validate our experimental results as well as the goodness of using optimal control techniques to achieve time-reversal transformations, the atomic populations are measured at the end of the control pulse at $t = T$. Then, the error function ϵ is computed by comparing our measurements with the corresponding theoretical values obtained by reversing the time evolution of the BEC, both using $f(-T)$ (inversion of the time-dependence of the driving

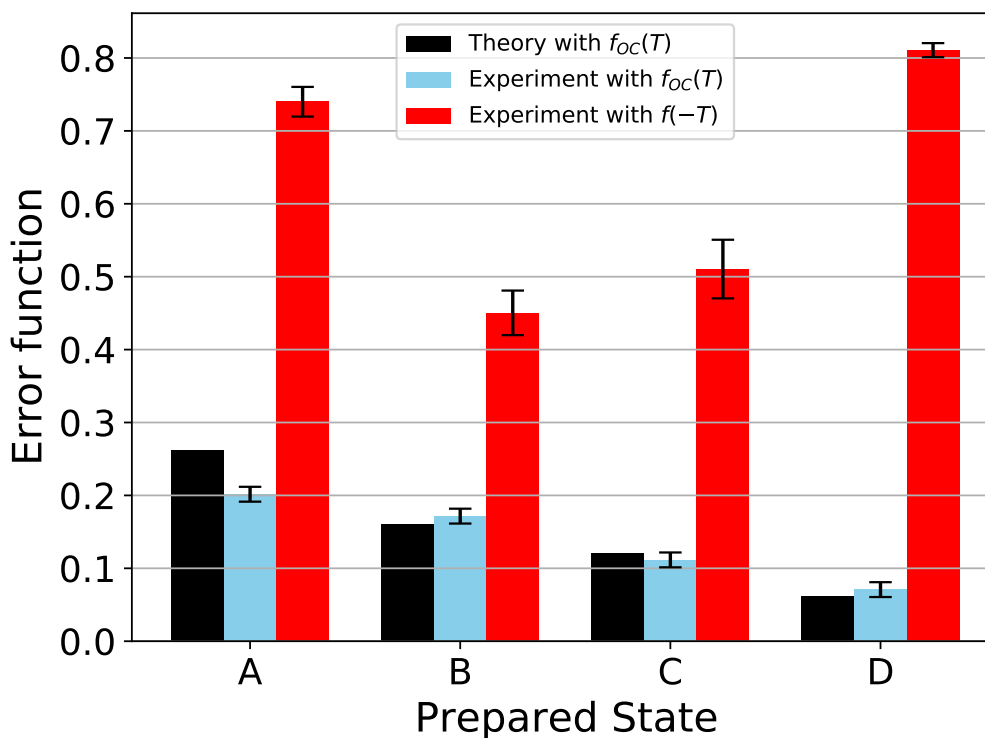


Figure 4.5: *Control error functions.* Theoretical and experimental error function computed for the implemented time-reversed quantum dynamics in reaching the initial state $\rho(0)$ by starting from the target states $\hat{\rho}_A$, $\hat{\rho}_B$, $\hat{\rho}_C$, $\hat{\rho}_D$ or at least in proximity of them, depending on the experimental accuracy achieved for their preparation. The black bar represents the numerically simulated error function obtained through the optimized inversion of the driving field $f_{OC}(T)$. The light blue bar is the corresponding experimental error function (with its standard deviation), while the red bar denotes the experimental error (with its standard deviation) obtained by changing the time-dependence of the driving field and thus applying the pulse $f(-T)$. The error bars are computed by repeating 10 times each set of experiments. It is worth noting that, clearly, the error function is not zero also in the case of the numerical simulation. Indeed, this occurs first for the presence of experimental decoherence, as we will show in Subsec. 4.3.2 where the optimal time-reversal is tested over time. Secondly it follows from the limited number of resources at disposal, in terms of OC operations, to avoid computational burden.

field) and $f_{OC}(T)$ (optimal driving field). The resulting values of the error functions are illustrated in Fig. 4.5 where similar behaviors can be observed for all the tested target states i), ii), iii) and iv). Here, it is worth noting that our results are validated just by using the atomic populations of the system. However, it is well-known that measuring the population elements of a quantum system represents only a partial knowledge of its full density matrix. For this reason, albeit the excellent agreement between theoretical continuous lines and experimental dots in

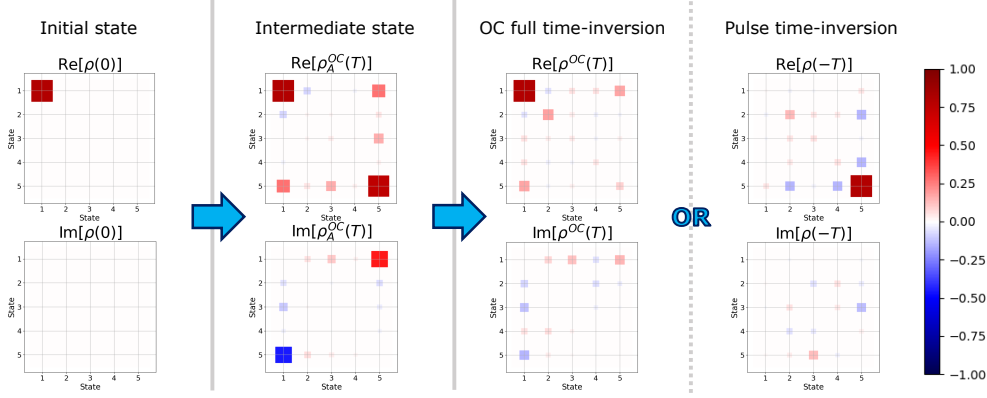


Figure 4.6: *Tomographic reconstruction.* Density matrix representation of the initial state $\rho(0)$, the intermediate state $\rho_A^{OC}(T)$ (reached via OC and as much close as possible to the target state $\hat{\rho}_A$), and the final states $\rho^{OC}(T)$ and $\rho(-T)$ obtained by inverting or the whole system quantum dynamics via OC techniques or the pulse time-dependence of the driving field respectively.

Fig. 4.3 that seems to confirm our assumption of unitary dynamics, we perform a full density matrix reconstruction for the case i). In this case, the atomic population of the target state is equally distributed among the two hyperfine states $|F = 2, m_F = 2\rangle \equiv | + 2\rangle$ and $|F = 2, m_F = -2\rangle \equiv | - 2\rangle$. As reported in Fig. 4.6, we have measured the density matrix of the experimental state $\rho_A^{OC}(T)$ that is reached in the forward evolution by following the optimized OC path from the initial state $\rho(0) = | + 2\rangle\langle + 2|$ to the intermediate target state $\hat{\rho}_A$. Then, the two possible final density matrices $\rho^{OC}(T)$ and $\rho(-T)$, corresponding respectively to the ending stage of the optimally controlled and time-inverted backward trajectories, are also reconstructed. The time evolution of sub-levels $| + 2\rangle$ and $| - 2\rangle$ is also shown in Fig. 4.7 and is in perfect agreement with the theoretical predictions. These experimental findings confirm our assumption on the accuracy of the implemented time-reversal transformations as well as the presence of the correct coherence terms in the measured density matrices. Furthermore, the results illustrated in Fig. 4.6 and 4.7 clearly show that inverting only the time-dependence of the driving field brings the BEC atomic population closer (in the sense given by the Uhlmann fidelity) to the orthogonal state $| - 2\rangle$ instead of $| + 2\rangle$, while the optimally reversed evolution successfully reaches the initial state.

4.3.2 Second set of experiments

To evaluate the time limits/constraints of the optimally-controlled time-reversal transformations implemented in the first set of experiments, we perform a *sec-*

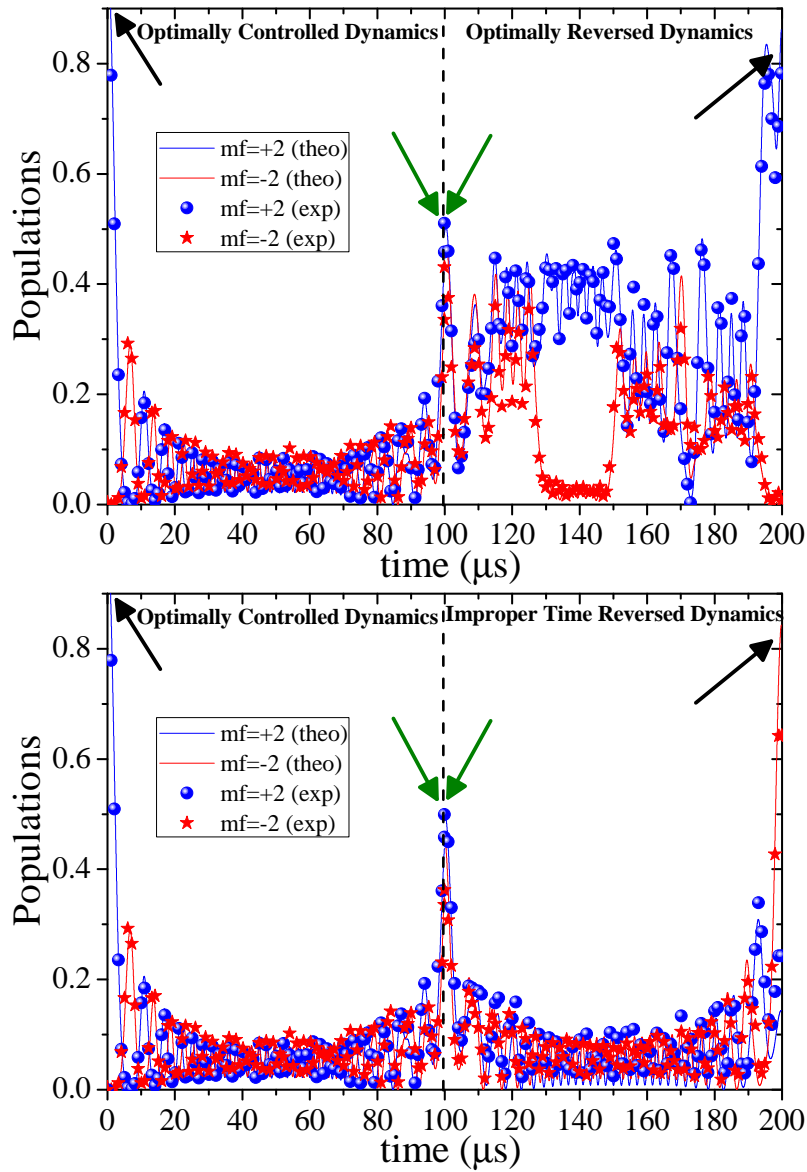


Figure 4.7: Forward and backward evolution of $|+2\rangle$ and $|-2\rangle$ sub-levels. Top: The backward evolution is driven by the pulse $f_{OC}(T)$. Bottom: The backward evolution is driven by the pulse $f(-T)$. In the optimally reversed dynamics the atomic population goes back to the initial state $|+2\rangle$, thus perfectly restoring the initial condition. In the time-reversed dynamics, instead, the atomic population accumulates in the orthogonal state $|-2\rangle$. Also here it can be noted that the theoretical curves do not reach unity in the backward process. It is due to decoherence and to resource consuming operations, from a computational point of view, in the OC optimization as previously motivated in the caption of Fig. 4.5.

and set of experiments (see Fig. 4.4b) to drive the quantum system evolution back

and forth from the state $\rho(0)$ to quantum target states $\widehat{\rho}_{Q_j}$, along the same trajectory, by using pulses of gradually shorter lengths T_j , which belong to the interval $\{10, 20, 40, 60, 70, 80, 100\} \mu\text{s}$. In all these experiments, the pulses that realize the forward and backward processes have the same duration. In more details, first we design an optimal forward pulse that brings the quantum system from the initial state $\rho(0)$ to the state $\widehat{\rho}_A$ reached at $T = 100 \mu\text{s}$. We thus obtain the optimal values of the pulse's parameters by fixing the length of the control pulse to $T = 100 \mu\text{s}$. Then, from such a pulse, we generate a set of sub-pulses with a gradually shorter length T_j (including $T = 100 \mu\text{s}$). In this way, by varying T_j from $10 \mu\text{s}$ to $100 \mu\text{s}$, the quantum state $\widehat{\rho}_{Q_j}$ is always closer (according to the error function ϵ) to $\widehat{\rho}_A$, until it coincides with $\widehat{\rho}_A$ for $T_j = 100 \mu\text{s}$. Then, a backward process from $\widehat{\rho}_{Q_j}$ to the quantum state $\rho(0)$ is realized, once by inverting the time-dependence of the forward pulse and another using OC to design the backward pulse, similarly to what done in the first set of experiments. Also the experimental results, reported in Fig. 4.8, show a quite small error in realizing reversed quantum dynamics via optimal control techniques, while on the contrary the dynamics obtained by changing the time-dependence of the driving field leads to a higher value of the error function ϵ . The experimental results are in perfect agreement with the corresponding theoretical predictions for driving pulses with short duration, while for experiments longer than $80 \mu\text{s}$ the mismatch increases. The reason behind this behaviour is in the presence of experimental dephasing noise that entails quantum coherence degradation. In fact, by including the presence of dephasing noise in the theoretical model, whose effects on the error function are depicted by the light-blue shaded area in Fig. 4.8, the mismatch between experimental and theoretical data can be explained. Dephasing noise in the model is included by means of the following Lindbladian super-operator term \mathcal{L} acting on the density matrix $\rho(t)$:

$$\mathcal{L}(\rho(t)) = \sum_{n=1}^5 \gamma_n [-\{ |n\rangle\langle n|, \rho(t) \} + 2|n\rangle\langle n| \rho(t) |n\rangle\langle n|] \quad (4.4)$$

where $\{\cdot, \cdot\}$ denotes the anticommutator. The action of \mathcal{L} is to randomize the phase of each sub-level n of the BEC with rate γ_n , whose value for simplicity has been taken constant for all the sub-levels, i.e., $\gamma_n \equiv \gamma \in 2\pi[20, 200]$ Hz. Hence, the light-blue shaded area is obtained as in the following. The difference between the experimental and theoretical points at $100 \mu\text{s}$ is attributed exclusively to the dephasing noise that determines the range of γ . Then, starting from such dephasing range, the minimum and maximum values of the shaded area at each pulse length T are obtained by numerically solving the GKSL equation:

$$\dot{\rho}(t) = -\frac{i}{\hbar}[H(t), \rho(t)] + \mathcal{L}(\rho(t)), \quad (4.5)$$

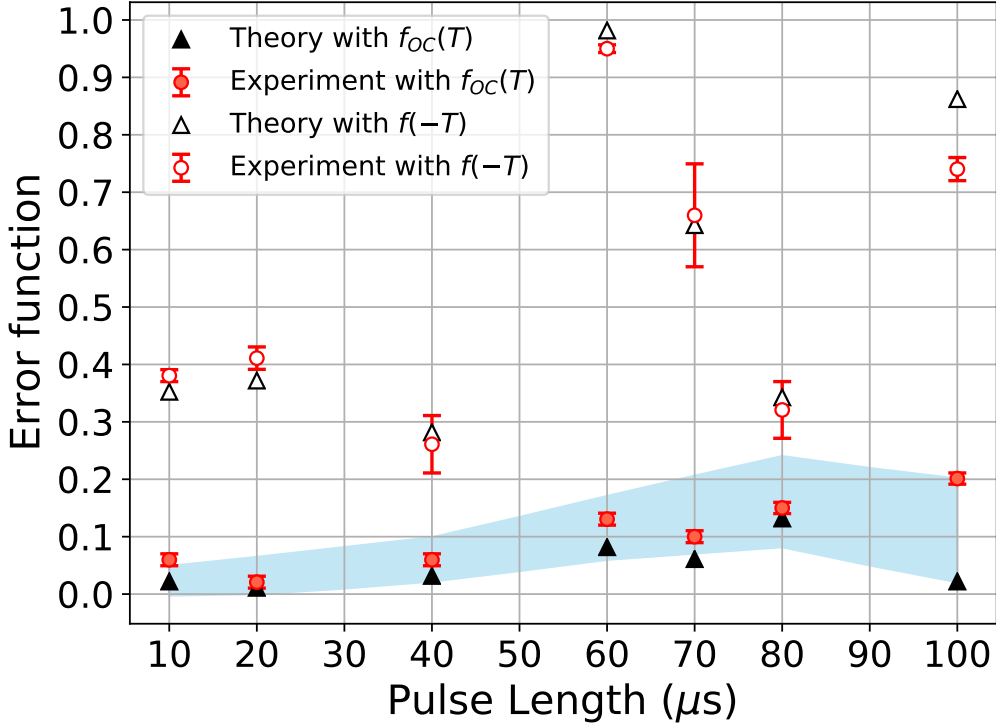


Figure 4.8: *Testing optimal time-reversal over time.* The error function vs pulse length T , with $T \in \{10, 20, 40, 60, 70, 80, 100\} \mu\text{s}$, is reported from both the theoretical and experimental side. The values of the error function are evaluated once by using the proposed optimal control strategy and another by inverting the time-dependence of the driving field. In the figure, we also take into account the presence of experimental dephasing noise on the quantum system evolution, by including in the numerical simulations a correction term that amends the theoretical prediction. The correction, pictorially represented in the figure by the light-blue shaded area, is numerically simulated for each value of T by solving the differential equation (4.5) in the dephasing range $\gamma_n \equiv \gamma \in 2\pi[20, 200]$ Hz (estimated at $T = 100 \mu\text{s}$) and with an additional magnetic field fluctuation with standard deviation of 1 mG . In this way, the correction is finally obtained by taking the corresponding minimum and maximum values of such computation.

by varying the dephasing rate $\gamma_n \equiv \gamma$ in the interval $2\pi[20, 200]$ Hz and considering magnetic field fluctuations within the range $\Delta B = 1 \text{ mG}$. In this regard, we recall that in the GKSL equation, which models the time evolution of the system's density matrix affected by dephasing noise, $H(t) \equiv H_0 + H_{RF}(t)$ with $H_{RF}(t)$ defined as in Sec. 4.2 and $f(t)$ is constrained in the range $f(t) \in 2\pi[4150, 4600]$ kHz, so as to maintain always the same coupling of the RF antenna to the driving circuit.

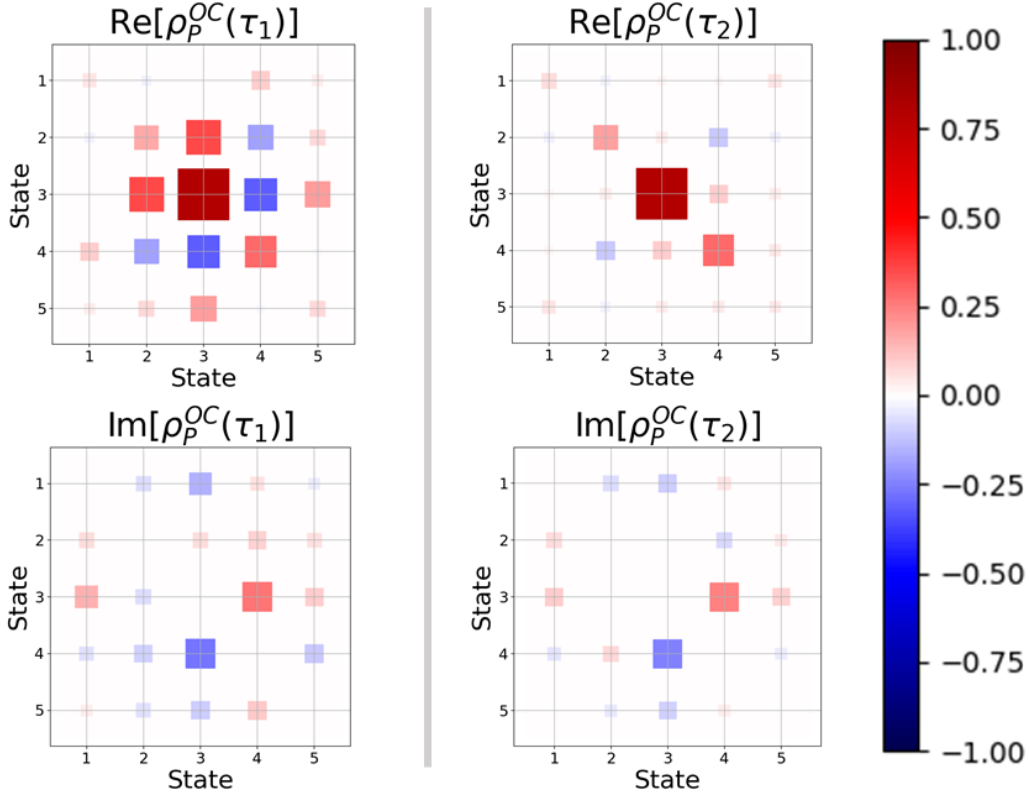


Figure 4.9: Tomography reconstruction of the measured states $\rho_p^{OC}(\tau_1)$ and $\rho_p^{OC}(\tau_2)$. The state $\rho_p^{OC}(\tau_1)$, reported on the left-hand side of the image, is reached in $\tau_1 = 33 \mu\text{s}$ in the first stage of the experiment and represents a state in the past of the system evolution. The state $\rho_p^{OC}(\tau_2)$ on the right-hand side of the image is reached in $\tau_2 = 67 \mu\text{s}$ via the optimally time inverted dynamics. The accuracy $1-\epsilon$ between these two measured density matrices is 97.3%.

4.3.3 Third set of experiments

To better illustrate the wide applicability of our implemented time-reversal procedures, in a *third set of experiments* (see Fig. 4.4c) we aim to show that our OC strategy is able to *invert the evolution of the quantum system by driving it back from $\hat{\rho}_A$ (target state at $T = 100 \mu\text{s}$) to a quantum state $\rho_p(\tau)$ that is reached in $\tau \leq 100 \mu\text{s}$ along the same trajectory linking $\rho(0)$ with $\hat{\rho}_A$* . In this way, we are going to show that it is also possible to drive the system back to a generic quantum state that has been already explored in the past. This effectively qualifies our experiments as a proof-of-principle of quantum *undo* operations, whereby the external user has to be able to reverse at will the last operation they performed. In more details, also in this case, the set of experiments is two-fold. First, starting from the initial state $\rho(0)$, the system evolution, enabled by the driving pulse

that drives the quantum system from $\rho(0)$ to $\widehat{\rho}_A$ in $100 \mu\text{s}$ (it is the same optimal pulse used in the first set of experiments), is interrupted after $\tau_1 = 33 \mu\text{s}$. In that instant, the system has reached the intermediate state $\rho_P^{OC}(\tau_1)$, which is then reconstructed via tomography. Therefore, this first stage of the experiment allows us to identify the state $\rho_P(\tau)$, with τ taken equal to τ_1 in our case. Secondly, the system is made evolve from the initial state $\rho(0)$ to the target state $\widehat{\rho}_A$ in $100 \mu\text{s}$ without interrupting the pulse. Exploiting the dCRAB optimization procedure, then, a path from $\widehat{\rho}_A$ to the state $\rho_P(\tau_1)$ is traced back by using an optimal pulse lasting $\tau_2 = 67 \mu\text{s}$ (note that, by construction, $\tau_1 + \tau_2 = 100 \mu\text{s}$), and the resulting state $\rho_P^{OC}(\tau_2)$ is measured again via a tomographic process. The experimental results are reported in Fig. 4.9.

The accuracy $1 - \epsilon$ between the measured density matrix $\rho_P^{OC}(\tau_1 = 33 \mu\text{s})$, representing a state in the past of the system evolution, and the measured state $\rho_P^{OC}(\tau_2 = 67 \mu\text{s})$ reached via the optimally time inverted dynamics, is around 97.3%. These results illustrate that the implemented OC strategy allows to perform a quantum *undo* operation not only of the last quantum state ρ_A but also of any past state $\rho_P(\tau)$ in the occurred quantum dynamics. In other terms, one is able to bring back the system from the target state $\widehat{\rho}_A$ to the initial one $\rho(0)$, but even from $\widehat{\rho}_A$ to a generic state along the pathway $\rho(0) \longleftrightarrow \widehat{\rho}_A$.

4.4 Discussion & conclusions

The experiments presented in this chapter have tested the validity of using optimal control theory, enabled in our case by a dCRAB technique, to carry out time-reversal transformations with high accuracy (on average around 92%) in a Bose-Einstein condensate realized on an atom-chip. Specifically, we have realized three sets of experiments. In the first set, the laser-cooled ^{87}Rb atoms of the condensate are driven forward and backward in time from an initial state $\rho(0)$ to a target one and then back to $\rho(0)$. In the second set of experiments, we have shown that the adopted OC technique works with almost equal accuracy in bringing back to the initial condition any quantum target state along the same trajectory, independently on the time instant in which the target state was achieved in the forward evolution of the system. In a third set of experiments, we have also experimentally demonstrated the possibility to drive the quantum system back to a quantum state already explored in its past dynamics. In our opinion, all these experiments constitute the proof-of-principle of a wide class of *undo* operations that might be implemented in the next future in several quantum technology contexts. In particular, the implementation of *undo* operations of the last step (or a few last steps) of a quantum circuit for quantum computing applications, is the main outlook of the experiments here presented. In this

regard, however, it remains an open question whether it is always possible to calculate such an *undo* operation, thus not only of the last few steps of a quantum circuit. Indeed, this would require the knowledge of the state of the system at any time which is not always possible.

To conclude, let us provide the thermodynamic interpretation of our experimental results. The introduction of a procedure to achieve time-reversal transformations is implicitly linked with the understanding of a clever way to nullify (or even rectify) the thermodynamic entropy originated by the system [144–151]. Thermodynamics, and in particular the second law, tells us that if a dynamical process (classical or quantum) is reversible, then it spontaneously (without further consumption of resources) operates to go back to the starting point by following the minimum energy trajectories allowed during the system evolution. Such dynamics are also denoted as autonomous, and thus it is not required to steer the system towards the desired state by means of an external drive. Clearly, this is not the case in our experiments. Indeed, the decoherence time, intrinsic to the Bose-Einstein condensate, imposes a time limit of 100 μs to the experimental implementation of the dynamics as we showed in Subsec. 4.3.2. This temporal constraint makes the quantum process irreversible thus needing to pump energy from the outside (in our case making use of optimal control strategies) to successfully carry out time-reversal transformations. In our experiments, we have quantified this aspect by computing the Loschmidt echo $M(\tau) \equiv |\langle \psi_0 | e^{i\mathcal{H}_2(\tau)\tau} e^{-i\mathcal{H}_1(\tau)\tau} | \psi_0 \rangle|^2$ [152–154], with \hbar here set to 1, $|\psi_0\rangle$ denoting the initial wave-function such that $\rho(0) = |\psi_0\rangle\langle\psi_0|$, and τ duration of both the forward and backward processes. Since in our case we can identify $\mathcal{H}_1(t) = H(t)$ (i.e., as the BEC Hamiltonian of the forward process in the implemented dynamics) and $\mathcal{H}_2(t) = H_{OC}(t)$ (i.e., the optimal control Hamiltonian in which the driving field is $f_{OC}(t)$), the Loschmidt echo $M(\tau)$ can be equivalently written as:

$$M(\tau) = \text{Tr} \left[e^{iH_{OC}(\tau)\tau} \widehat{\rho}(\tau) e^{-iH_{OC}(\tau)\tau} \rho(0) \right] = \text{Tr} \left[\rho^{OC}(\tau) \rho(0) \right], \quad (4.6)$$

where $\widehat{\rho}(\tau)$ is the target quantum state achieved by the forward process at $t = \tau$. The values of $M(\tau) = \text{Tr}[\rho^{OC}(\tau)\rho(0)]$ computed experimentally for each set of tomographic data are practically equal to the corresponding Uhlmann fidelity values $\mathfrak{F}(\rho^{OC}(\tau), \rho(0))$ that we have used to evaluate the accuracy of the implemented time-reversal transformations. This evidence, beyond providing a clear thermodynamic interpretation of our experimental findings, allows us to conclude in quantitative terms that the time-arrow inversion $t \rightarrow -t$ of the time-dependent terms in the interaction Hamiltonian is not sufficient in general to reverse a quantum evolution and thus to implement quantum *undo* operations.

Final remarks

In this thesis work I presented two quantum protocols that share a common atomic platform represented by a Bose-Einstein condensate of ^{87}Rb atoms realized on an atom-chip. I showed how the exquisite control that the atom-chip enables, is a powerful tool in the manipulation of the BEC internal state dynamics. The latter is fundamental in the development of the quantum protocols realized in this thesis work, whose success relies on the high degree of control reachable in the ultimate stages of our experimental sequence.

In the context of classification algorithms used in Quantum Machine Learning, I implemented a first protocol of quantum embedding to map a string of complex classical data into the Hilbert space of the BEC where the classification is easier. I described how, in a first “*learning*” stage, the optimal quantum circuit that realizes the mapping of the data is identified. This is provided by the construction of a cost function that, after an iterative routine of 200 gradient descent steps, finds the optimal parameters for the embedding taking only a few minutes of computational time. After the system has learned how to perform classification, by virtue of the acquired knowledge during the training, I illustrated how the protocol can be implemented on three different platforms, namely ultra-cold atoms, photons and superconductive circuits, to test its robustness to real-world deployment scenarios. The experimental results I presented demonstrate that a fidelity exceeding 90% can be routinely achieved on all the explored platforms. In particular the atomic platform reaches fidelities even higher than 97%, proving that ultra-cold systems are promising candidates for the implementation of this kind of algorithms. Indeed, the degree of control and isolation from the external environment, provided by the ultra-high-vacuum in which the atoms are held and by the stable magnetic and RF fields, is generally much better than what can be achieved with the other platforms. Estimating resources for quantum algorithms using realistic quantum computing architectures is an important near-term challenge. The optimization of specific algorithms to a specific hardware is the highest and most important level of quantum computers co-design. In this regard our experimental investigation demonstrates how quantum embedding techniques may suit radically different approaches to qubit encoding

and manipulation by pulses as for ultra-cold atoms, by quantum logic circuits as for superconductive platforms or by compiled operations as for photons. Such results show promise for future interconnected systems or hybrid architectures with specialized hardware for storage, processing and distribution of quantum data.

Another quantum protocol I described in this thesis concerns the driving forward and backward in time of our BEC's dynamical evolution, by adopting an optimal control theory, enabled by the dCRAB algorithm. I reported how the proposed strategy is successfully applied along several paths of the system's Hilbert space, where quantum operations can be inverted by using gradually higher levels of control. Indeed, in a first experiment the time-inversion is successfully achieved from an initial state $\rho(0)$ to a target one and then back again to $\rho(0)$. The procedure is further confirmed repeating the experiment by choosing different intermediate target states. In a second set of experiments, the implemented transformation is then extended to a more complicated situation in which the backward evolution is performed in a gradually shorter time-scale and in which high accuracy levels are required. Finally, a third set of experiments shows that it is also possible to drive the system back to a quantum state already explored in a past evolution, by starting from the present one in which the system is. In order to make a comparison and corroborate the need to employ quantum optimal control methods, I reported how different the experimental outcomes are if one simply inverts the time-dependence of the external driving field, through an addition of a phase term, instead of using an optimal driving pulse. The experimental findings with optimal control, indeed, have an average accuracy of 92%, while the ones with the pulse time-inversion have an average accuracy of 38%. All the experiments I described to test time-reversal transformations with ultra-cold atoms, can be seen as the proof-of-principle of *undo* operations in quantum regimes. An alternative outlook could be in the implementation of the above techniques for self-verification algorithms.

As I showed, ultra-cold neutral atoms can simulate a wide variety of phenomena, thanks to their high degree of isolation, flexible geometry, spin control and easily observable dynamics. However, challenges can arise in several scenarios like, for instance, the non-uniformity of trapping potentials or a variety of loss and decoherence mechanisms from the interaction with background vacuum gas. Sometimes the imperfections such as noise and decoherence cannot accurately be modeled theoretically and must be explored empirically by building and testing more complex simulation platforms. In some cases quantum control can be exploited to protect the quantum sensor from environmental noise or even enhance the system's response to an external unknown perturbation and investigate its nature. In this regard, even though this was not the subject of this thesis, in our group we experimentally explored a new method, based on the stochas-

tic Quantum Zeno effect [155–157], to estimate the power spectral density of an unknown noise field. The control signal, in this case, is applied together with repeated projective measurements to correlate the final survival probability of the system and the noise spectrum. The results of this work are available at:

- Hoang-Van Do, Cosimo Lovecchio, Ivana Mastroserio, Nicole Fabbri, Francesco S. Cataliotti, Stefano Gherardini, Matthias M. Müller, Nicola Dalla Pozza, and Filippo Caruso, *Experimental proof of quantum Zeno-assisted noise sensing*. *New J. Phys.* **21**, 113056 (2019).

The measurement of environmental effects on a quantum system is of great importance for the development of quantum technologies. For high performance quantum computers, indeed, it is essential to distinguish between the intrinsic noise in the qubits, coming from their coupling to the environment (decoherence), and the noise coming from control errors. The latter, for instance, can be either systematic in nature, such as drifts or crosstalks, or stochastic, such as thermal and shot noise in the control sources. Quantum control techniques can thus be included as a possible mitigation approach of such effects, by designing the controller in a way such that the impact of stochastic noise on the qubits is smaller than their intrinsic one, and the systematic noise is fully characterized and thus, where possible, reduced.

Appendices

A | Rubidium 87

In this appendix I supply some useful numbers of Rubidium 87 within the context of this thesis. Most information is taken from Ref. [57].

Relative Natural Abundance	$\eta(^{87}\text{Rb})$	27.83(2)%
Atomic Mass	m	$1.443\,160\,60(11) \times 10^{-25} \text{ kg}$
Nuclear Spin	I	3/2

Table A.1: Physical properties of ^{87}Rb .

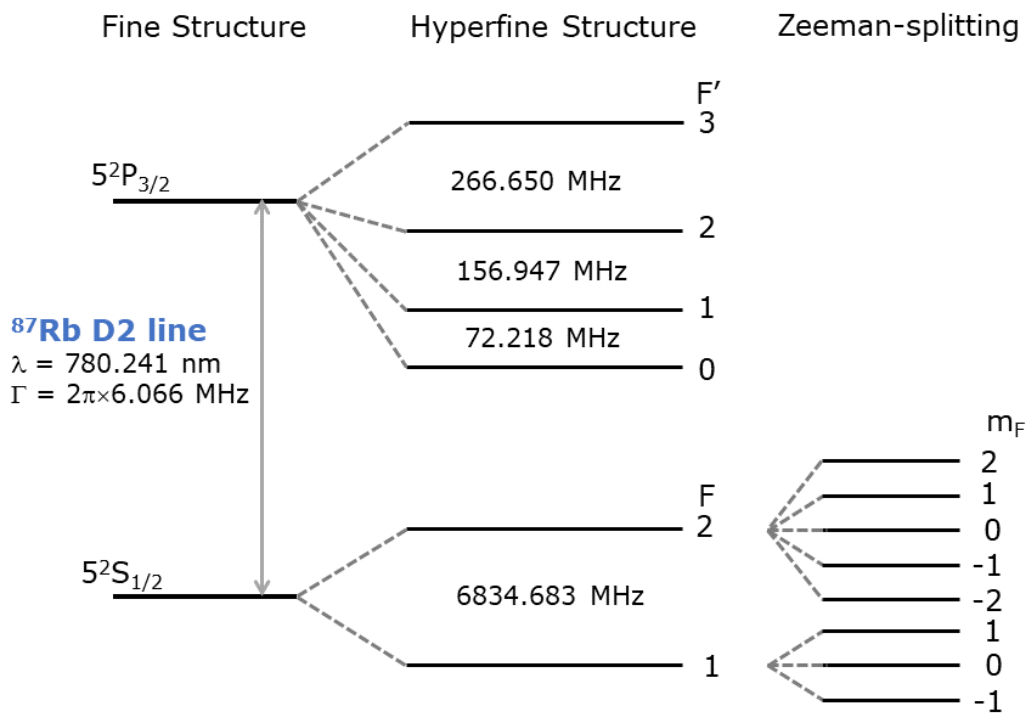


Figure A.1: ^{87}Rb D2 transition structure.

Frequency	ω_0	$2\pi \times 384.230\,484$ THz
Wavelength in vacuum	λ	780.241 209 nm
Wavelength in air	λ_{air}	780.032 00 nm
Wave Number in vacuum	$k_L/2\pi$	$12\,816.549\,389$ cm ⁻¹
Lifetime	τ	26.24(4) ns
Decay Rate/Natural Line Width (FWHM)	Γ	$38.11(6) \times 10^6$ s ⁻¹
		$2\pi \times 6.065(9)$ MHz
Recoil Velocity	v_r	5.8845 mm s ⁻¹
Recoil Frequency	ω_r	$2\pi \times 3.7710$ kHz
Recoil Temperature	T_r	361.96 nK
Doppler Shift ($v_{atom} = v_r$)	$\Delta\omega_D(v_{atom} = v_r)$	$2\pi \times 7.5419$ kHz
Doppler Temperature	T_D	146 μ K
Effective Saturation Intensity (π -polarized light)	I_{sat}	2.503(3) mW cm ⁻²

Table A.2: Optical properties of ⁸⁷Rb D2-line transition ($5^2S_{1/2} \rightarrow 5^2P_{3/2}$). Note that k_L is the wave-vector of the laser light.

Electron spin Landé g -factor	g_S	2.002 319
Electron orbital Landé g -factor	g_L	0.999 993
Nuclear Landé g -factor	g_I	-0.000 995
Fine structure Landé g -factor	$g_J(5^2S_{1/2})$	2.002 331
	$g_J(5^2P_{1/2})$	0.666
	$g_J(5^2P_{3/2})$	1.3362

Table A.3: Magnetic field interaction parameters of ⁸⁷Rb D transition.

B | C-SWAP Test

The *Controlled-SWAP* gate (C-SWAP or Fredkin gate) is a gate with three input and three output. It transfers the first input unchanged while swapping the last two if and only if the first input is 1. It is illustrated in Fig. B.1. In quantum computation, this test is used to check how two given quantum states differ. This quantum circuit efficiently implements the fidelity classifier reported in Eq. (3.8). Given the initial state $|0, \phi, \psi\rangle$ as an input for the C-SWAP circuit, it is easy to

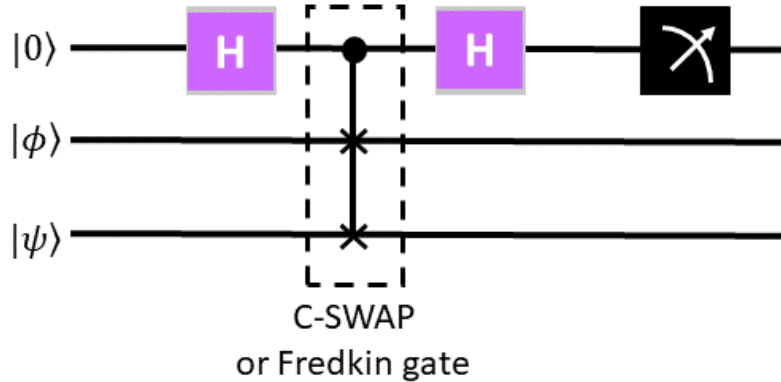


Figure B.1: *C-SWAP quantum circuit*. The quantum circuit, reported in this figure, implements a controlled-swap test between the states $|\phi\rangle$ and $|\psi\rangle$. The Hadamard gate is indicated with H , $|0\rangle$ is the ancilla qubit and $|0, \phi, \psi\rangle$ is the initial state to which the gate is applied.

verify that a C-SWAP and two Hadamard gates realize the swapping of the two states in input $|\phi\rangle$ and $|\psi\rangle$, with the use of the ancilla qubit $|0\rangle$. Let us recall the matrix form of the Hadamard gate:

$$H = \frac{1}{\sqrt{2}} \begin{pmatrix} 1 & 1 \\ 1 & -1 \end{pmatrix}. \quad (\text{B.1})$$

Following the circuit in Fig. B.1, after the first Hadamard gate, the state of the system becomes:

$$H \longrightarrow \frac{1}{\sqrt{2}} (|0, \phi, \psi\rangle + |1, \phi, \psi\rangle). \quad (\text{B.2})$$

The C-SWAP gate, applied to the latter, swaps only the states that have the ancilla as $|1\rangle$, thus obtaining:

$$\text{C-SWAP} \longrightarrow \frac{1}{\sqrt{2}} (|0, \phi, \psi\rangle + |1, \psi, \phi\rangle) . \quad (\text{B.3})$$

The second Hadamard gate will then give:

$$\text{H} \longrightarrow \frac{1}{2} |0\rangle (|\phi, \psi\rangle + |\psi, \phi\rangle) + \frac{1}{2} |1\rangle (|\phi, \psi\rangle - |\psi, \phi\rangle) . \quad (\text{B.4})$$

Finally, the measurement gate on the first qubit will ensure that it is $|0\rangle$ with probability:

$$P_{|0\rangle} = \frac{1}{2} + \frac{1}{2} |\langle \psi | \phi \rangle|^2 . \quad (\text{B.5})$$

Hence, if $\psi \perp \phi$, then $|\langle \psi | \phi \rangle|^2 = 0$ and the probability to measure $|0\rangle$ is $P_{|0\rangle} = 1/2$. While, if $\psi = \phi$, then $|\langle \psi | \phi \rangle|^2 = 1$ and the probability to measure $|0\rangle$ is $P_{|0\rangle} = 1$.

List of abbreviations

AI	Artificial Intelligence
AOM	Acusto Optic Modulator
AP	Anamorphic Prism
APD	Avalanche Photodiode Detector
BBO	Beta Barium Borate
BEC	Bose-Einstein condensate
CCD	Charged Coupled Device
CMOT	Compressed Magneto Optical Trap
CW	Continuous Wave
dCRAB	dressed Chopped Random Basis
DDS	Direct Digital Synthesizer
DFB	Distributed Feedback
EM	Electro-Magnetic
EOM	Electro Optic Modulator
FM	Frequency Modulated
FWHM	Full Width at Half Maximum
GKSL	Gorini-Kossakowski-Sudarshan-Lindblad
HWP	Half Waveplate
ML	Machine Learning
MOT	Magneto Optical Trap
NISQ	Noisy Intermediate-Scale Quantum
OBE	Optical Bloch Equations
OC	Optimal Control
OD	Optical Density
OI	Optical Isolator
OM	Optical Molasses
PBS	Polarizing Beamsplitter
PD	Photodiode
PQCs	Parametrized Quantum Circuit

QE	Quantum Embedding
QEKs	Quantum Embedding Kernels
QML	Quantum Machine Learning
QWP	Quarter Waveplate
RWA	Rotating Wave Approximation
SI	International System of Units
SMA	Sub-Miniature version A
TA	Tapered Amplifier
UHV	Ultra High Vacuum

List of Figures

1.1	Doppler cooling	9
1.2	The force in the Optical Molasses technique	10
1.3	Breit-Rabi diagram	17
1.4	MOT scheme	19
1.5	Quadrupole and Ioffe-Pritchard traps	23
1.6	Bose-Einstein condensation	25
1.7	Evaporative cooling	26
1.8	Radio-frequency evaporative cooling	27
2.1	Magnetic guide	32
2.2	Quadrupole U-trap	33
2.3	Ioffe-Pritchard Z-trap	34
2.4	The atom-chip layout	36
2.5	Backside of the atom-chip	37
2.6	Mirror-MOT	39
2.7	Mirror MOT optical setup	40
2.8	^{87}Rb D2-line and laser frequencies	42
2.9	Laser system	43
2.10	Time-line of the BEC production program	44
2.11	Unbalanced compensation fields effects	46
2.12	BEC density profile	48
2.13	Imaging system	49
2.14	Internal states manipulation of our BEC	52
2.15	Micro-wave antenna	53
3.1	Linear classifier	59
3.2	The kernel trick	60
3.3	A string of classical data to be classified	63
3.4	Pictorial representation of quantum embedding	64
3.5	Before and after learning	65
3.6	Bloch sphere representation of a qubit	67

3.7	Rotations around \hat{x}	72
3.8	Rotations around \hat{z}	73
3.9	Ramsey sequence	75
3.10	Ramsey fringes	76
3.11	Atomic level scheme for quantum embedding	77
3.12	Control pulses sequences and embedded states results	80
3.13	Fidelities and Bloch vectors results for the atomic platform	81
3.14	Rabi frequency stability: Allan deviation	83
3.15	Detuning stability: Allan deviation	84
3.16	Quantum embedding in the rotated frame	86
3.17	Quantum circuit for the superconducting platform	87
3.18	Fidelities and Bloch vectors results for the photonic platform	89
3.19	Gram matrices results of quantum embedding	91
4.1	Pictorial representation of the realized time-reversal experiments	96
4.2	Relevant ^{87}Rb atomic energy levels	98
4.3	Illustration of an atomic population dynamics	101
4.4	Time reversal experiments	102
4.5	Control error functions	104
4.6	Tomographic reconstruction	105
4.7	Forward and backward evolution of $ +2\rangle$ and $ -2\rangle$ sub-levels	106
4.8	Testing optimal time-reversal over time	108
4.9	Tomography reconstruction of states $\rho_P^{OC}(\tau_1)$ and $\rho_P^{OC}(\tau_2)$	109
A.1	^{87}Rb D2 transition structure	116
B.1	C-SWAP quantum circuit	118

List of Tables

3.1	Embedding parameters for the atomic platform	79
3.2	Embedding parameters for the photonic platform	88
A.1	Physical properties of ^{87}Rb	116
A.2	Optical properties of ^{87}Rb D2-line transition ($5^2S_{1/2} \rightarrow 5^2P_{3/2}$) .	117
A.3	Magnetic field interaction parameters of ^{87}Rb D transition . . .	117

Bibliography

- [1] A. Galindo, and M. A. Martín-Delgado, *Information and computation: Classical and quantum aspects*. Reviews of Modern Physics, Volume 74, (2002).
- [2] M. Brooks, *Beyond quantum supremacy: the hunt for useful quantum computers*. Nature 574, 19-21 (2019).
- [3] R. P. Feynman, *Simulating Physics with Computers*. International Journal of Theoretical Physics, Vol. 21, Nos. 6/7, (1982).
- [4] R. Landauer, *The physical nature of information*. Physics Letters A 217, 188-193 (1996).
- [5] Y. Alexeev et al *Quantum Computer Systems for Scientific Discovery*. PRX Quantum 2, 017001 (2021).
- [6] H. J. Metcalf and P. Van Der Straten, *Laser Cooling and Trapping*. New York: Springer-Verlag (1999).
- [7] C. J. Foot, *Atomic Physics*. Oxford University Press (2005).
- [8] J. Clerk Maxwell, *Theory of Heat*. London, UK: Longmans, Green, and Co. (1871).
- [9] A. Ashkin, *Atomic-Beam Deflection by Resonance-Radiation Pressure*. Phys. Rev. Lett. 25, 1321 (1970).
- [10] T. Hänsch and A. Schawlow, *Cooling of gases by laser radiation*. Opt. Commun. 13, 68 (1975).
- [11] D. J. Wineland and H. Dehmelt, Bull. Am. Phys. Soc. 20, 637 (1975).
- [12] D. Wineland, R. Drullinger, and F. Walls, *Radiation pressure cooling of bound-resonant absorbers*. Phys. Rev. Lett. 40, 1639 (1978).

- [13] W. Neuhauser, M. Hohenstatt, P. Toschek, and H. Dehmelt, *Optical-Sideband Cooling of Visible Atom Cloud Confined in Parabolic Well*. Phys. Rev. Lett. **41**, 233 (1978).
- [14] S. Chu, L. Hollberg, J. E. Bjorkholm, A. Cable, and A. Ashkin, *Three-dimensional viscous confinement and cooling of atoms by resonance radiation pressure*. Phys. Rev. Lett. **55**, 48 (1985).
- [15] P. Lett, R. Watts, C. Westbrook, W. Phillips, P. Gould, and H. Metcalf, *Observation of Atoms Laser Cooled below the Doppler Limit*. Phys. Rev. Lett. **61**, 169 (1988).
- [16] D. S. Weiss, E. Riis, Y. Shevy, P. J. Ungar, and S. Chu, *Optical molasses and multilevel atoms: experiment*. J. Opt. Soc. Am. B **6**, 2072-2083 (1989).
- [17] J. Dalibard and C. Cohen-Tannoudji, *Laser cooling below the Doppler limit by polarization gradients: simple theoretical models*. J. Opt. Soc. Am. B **6**, 2023-2045 (1989).
- [18] P. J. Ungar, D. S. Weiss, E. Riis, and S. Chu, *Optical molasses and multilevel atoms: theory*. J. Opt. Soc. Am. B **6**, 2058-2071 (1989).
- [19] C. Cohen-Tannoudji and W. D. Phillips, *New Mechanisms for Laser Cooling*. Physics Today **43**, 10, 33 (1990).
- [20] S. Chu, *Manipulation of neutral particles*. Nobel lecture, Rev. Mod. Phys. **70**, 685 (1998).
- [21] S. Earnshaw, *On the nature of the molecular forces which regulate the constitution of the luminiferous ether*. Transactions of the Cambridge Philosophical Society **7**: 97-112 (1842).
- [22] A. Ashkin, *Acceleration and Trapping of Particles by Radiation Pressure*. Phys. Rev. Lett. **24**, 156 (1970).
- [23] D. E. Pritchard, E. L. Raab, V. Bagnato, C. E. Wieman, and R. N. Watts, *Light Traps Using Spontaneous Forces*. Phys. Rev. Lett. **57**, 310 (1986).
- [24] A. Ashkin, J. M. Dziedzic, J. E. Bjorkholm, and Steven Chu, *Observation of a single-beam gradient force optical trap for dielectric particles*. Opt. Lett. **11**, 288-290 (1986).
- [25] E. L. Raab, M. Prentiss, A. Cable, S. Chu, and D. E. Pritchard, *Trapping of Neutral Sodium Atoms with Radiation Pressure*. Phys. Rev. Lett. **59**, 2631 (1987).

- [26] E. Arimondo, M. Inguscio, and P. Violino, *Experimental determinations of the hyperfine structure in the alkali atoms*. Rev. Mod. Phys. **49**, 31 (1977).
- [27] G. Breit and I. I. Rabi, *Measurement of Nuclear Spin*. Phys. Rev. **38**, 2082 (1931).
- [28] E. Majorana, *Atomi orientati in un campo magnetico variabile*. Nuovo Cimento **9**, 43 (1932).
- [29] A. L. Migdall, J. V. Prodan, W. D. Phillips, T. H. Bergeman, and Ha. J. Metcalf, *First Observation of Magnetically Trapped Neutral Atoms*. Phys. Rev. Lett. **54**, 2596 (1985).
- [30] D. E. Pritchard, *Cooling neutral atoms in a magnetic trap for precision spectroscopy*. Phys. Rev. Lett. **51**, 1336-1339 (1983).
- [31] M. Haw, N. Evetts, W. Gunton, J. Van Dongen, J. L. Booth, and K. W. Madison, *Magneto-optical trap loading rate dependence on trap depth and vapor density*. J. Opt. Soc. Am. B **29**, 475-483 (2012).
- [32] M. H. Anderson, J. R. Ensher, M. R. Matthews, C. E. Wieman, and E. A. Cornell, *Observation of Bose-Einstein Condensation in a Dilute Atomic Vapor*. Science **269** (55221): 198-201 (1995).
- [33] K. B. Davis, M. -O. Mewes, M. R. Andrews, N. J. van Druten, D. S. Durfee, D. M. Kurn, and W. Ketterle, *Bose-Einstein Condensation in a Gas of Sodium Atoms*. Phys. Rev. Lett. **75**, 3969 (1995).
- [34] W. Ketterle, *When atoms behave as waves: Bose-Einstein condensation and the atom laser*. Nobel Lecture (2001).
- [35] N. Masuhara, J. M. Doyle, J. C. Sandberg, D. Kleppner, T. J. Greytak, H. F. Hess, and G. P. Kochanski, *Evaporative Cooling of Spin-Polarized Atomic Hydrogen*. Phys. Rev. Lett. **61**, 935 (1988).
- [36] C. Cohen-Tannoudji, D. Guéry-Odelin, *Advances in atomic physics: an overview*. World Scientific (2011).
- [37] M. Greiner, I. Bloch, O. Mandel, T. W. Hänsch, and T. Esslinger, *Exploring Phase Coherence in a 2D Lattice of Bose-Einstein Condensates*. Phys. Rev. Lett. **87**, 160405 (2001).
- [38] M. R. Andrews, C. G. Townsend, H.-J. Miesner, D. S. Durfee, D. M. Kurn, and W. Ketterle, *Observation of Interference Between Two Bose Condensates*. Science **275**, 637 (1997).

- [39] J. D. Weinstein and K. G. Libbrecht, *Microscopic magnetic traps for neutral atoms*. Phys. Rev. A **52**, 4004 (1995).
- [40] J. Fortagh, A. Grossmann, C. Zimmermann, and T. W. Hänsch, *Miniaturized Wire Trap for Neutral Atoms*. Phys. Rev. Lett. **81**, 5310 (1998).
- [41] V. Vuletic, T. Fischer, M. Praeger, T. W. Hänsch, and C. Zimmermann, *Microscopic Magnetic Quadrupole Trap for Neutral Atoms with Extreme Adiabatic Compression*. Phys. Rev. Lett. **80**, 1634 (1998).
- [42] J. Denschlag, D. Cassettari, and J. Schmiedmayer, *Guiding Neutral Atoms with a Wire*. Phys. Rev. Lett. **82**, 2014 (1999).
- [43] J. Reichel, W. Hänsel, and T. W. Hänsch, *Atomic Micromanipulation with Magnetic Surface Traps*. Phys. Rev. Lett. **83**, 3398 (1999).
- [44] W. Hänsel, P. Hommelhoff, T. W. Hänsch and J. Reichel, *Bose-Einstein condensation on a microelectronic chip*. Nature **413**, 498-501 (2001).
- [45] C. Henkel, S. Pötting, and M. Wilkens, *Loss and heating of particles in small and noisy traps*. Applied Physics B **69**, 379-387 (1999).
- [46] C. Henkel, P. Krüger, R. Folman, and J. Schmiedmayer *Fundamental limits for coherent manipulation on atom chips*. Applied Physics B **76**, 173-182 (2003).
- [47] P. Treutlein, *Coherent manipulation of ultracold atoms on atom chips*. Ph.D. Thesis, Ludwig-Maximilians-Universität München (2008).
- [48] Y.-J. Lin, I. Teper, C. Chin, and V. Vuletic, *Impact of the Casimir-Polder Potential and Johnson Noise on Bose-Einstein Condensate Stability Near Surfaces*. Phys. Rev. Lett. **92**, 050404 (2004).
- [49] Y.-J. Wang, D. Z. Anderson, V. M. Bright, E. A. Cornell, Q. Diot, T. Kishimoto, M. Prentiss, R. A. Saravanan, S. R. Segal, and S. Wu, *Atom Michelson Interferometer on a Chip Using a Bose-Einstein Condensate*. Phys. Rev. Lett. **94**, 090405 (2005).
- [50] T. Schumm, S. Hofferberth, L. M. Andersson, S. Wildermuth, S. Groth, I. Bar-Joseph, J. Schmiedmayer, and P. Krüger, *Matter-wave interferometry in a double well on an atom chip*. Nature Physics **1**, 57-62 (2005).
- [51] J. Reichel, *Microchip traps and Bose-Einstein condensation*. Appl. Phys. B **74**, 469 (2002).

- [52] I. Herrera, *Degenerate quantum gases production and coherent manipulation on atom chips*. Ph.D. Thesis, Universidad Autonoma de Madrid (2012).
- [53] S. Wildermuth, P. Krüger, C. Becker, M. Brajdic, S. Haupt, A. Kasper, R. Folman, and J. Schmiedmayer, *Optimized magneto-optical trap for experiments with ultracold atoms near surfaces*. Phys. Rev. A **69**, 030901(R) (2004).
- [54] S. Aigner, L. D. Pietra, Y. Japha, O. Entin-Wohlman, T. David, R. Salem, R. Folman, and J. Schmiedmayer, *Long-range order in electronic transport through disordered metal films*. Science (New York, N.Y.), **319**(5867), 1226-1229 (2008).
- [55] Y. Japha, O. Entin-Wohlman, T. David, R. Salem, S. Aigner, J. Schmiedmayer, and R. Folman, *Model for organized current patterns in disordered conductors*. Phys. Rev. B **77**, 201407(R) (2008).
- [56] W. Gerlach, and O. Stern, *Das magnetische Moment des Silberatoms*. Zeitschrift für Physik volume **9**, pages353-355 (1922).
- [57] D. A. Steck, *Rubidium 87 D Line Data*. Revision 2.2.2, 9 July 2021, available online at <http://steck.us/alkalidata>
- [58] C. Lovecchio, *Control of quantum dynamics on an atom chip*. Ph.D. Thesis, Università degli Studi di Firenze (2016).
- [59] N. F. Ramsey, *A Molecular Beam Resonance Method with Separated Oscillating Fields*. Phys. Rev. **78**, 695 (1950).
- [60] P. Rebentrost, M. Mohseni, and S. Lloyd, *Quantum Support Vector Machine for Big Data Classification*. Physical Review Letters **113**, 130503 (2014).
- [61] S. Lloyd, S. Garnerone, and P. Zanardi, *Quantum algorithms for topological and geometric analysis of data*. Nature Communications **7**, 10138 (2016).
- [62] R. S. Sutton, and A. G. Barto, *Reinforcement Learning: An Introduction*. MIT Press (2018).
- [63] A. Graves, A.-R. Mohamed, and G. Hinton, *Speech Recognition with Deep Recurrent Neural Networks* in 2013 IEEE International Conference on Acoustics, Speech and Signal Processing (IEEE), pp. 6645-6649 (2013).
- [64] N. Sebe, I. Cohen, A. Garg, and T. S. Huang, *Machine Learning in Computer Vision*, Springer Science & Business Media Vol. **29** (2005).

- [65] S. Grigorescu, B. Trasnea, T. Cocias, and G. Macesanu, *A survey of deep learning techniques for autonomous driving*. Journal of Field Robot, **37**, 362-386 (2020).
- [66] M. Chen, S. Mao, and Y. Liu, *Big Data: A Survey*. Mobile Networks and Applications **19**, pp 171-209 (2014).
- [67] F. Arute, K. Arya, R. Babbush, et al. *Quantum supremacy using a programmable superconducting processor*. Nature **574**, 505-510 (2019).
- [68] F. Rosenblatt, *The perceptron: A probabilistic model for information storage and organization in the brain*. Psychol. Rev. **65** (1958).
- [69] J. Schmidhuber, *Deep learning in neural networks: An overview*. Neural Networks **61** (2015).
- [70] T. Hastie, R. Tibshirani, and J. Friedman, *The elements of statistical learning: data mining, inference, and prediction*. Springer Science & Business Media (2009).
- [71] L. Buffoni, and F. Caruso, *New trends in quantum machine learning*. IOP Publishing, Europhysics Letters, Volume **132**, Number 6, pages 60004 (2021).
- [72] C. M. Bishop, *Pattern Recognition and Machine Learning*. Springer, New York, 1st edition 2006; corr. 2nd printing 2011 edition (2011).
- [73] I. Goodfellow, Y. Bengio, and A. Courville, *Deep Learning*. MIT Press web site: <http://www.deeplearningbook.org> (2016).
- [74] P. Vincent, H. Larochelle, Y. Bengio, and P. A. Manzagol, *Extracting and composing robust features with denoising autoencoders*. Proceedings of the 25th international conference on Machine learning, pages 1096-1103 (2008).
- [75] G. E. Hinton, P. Dayan, B. J. Frey, and R. M. Neal, *The "Wake-Sleep" Algorithm for Unsupervised Neural Networks*. Science, **268**, pp.1158-1161 (1995).
- [76] Y. Bengio, P. Lamblin, D. Popovici, and H. Larochelle. *Greedy layer-wise training of deep networks*. Proceedings of the 19th International Conference on Neural Information Processing Systems pp. 153-160 (2006).
- [77] B. E. Boser, I. M. Guyon, and V. N. Vapnik, *A Training Algorithm for Optimal Margin Classifiers*. Proceedings of the 5th Annual Workshop on Computational Learning Theory (COLT'92), Pittsburgh, 144-152 (1992).

- [78] C. Cortes, and V. Vapnik, *Support-vector networks*. Machine Learning volume **20**, pages 273-297 (**1995**).
- [79] M. Schuld, and F. Petruccione, *Supervised Learning with Quantum Computers*. Quantum Science and Technology book series, Springer International Publishing (**2018**).
- [80] P. Wittek, *Quantum Machine Learning: What Quantum Computing Means to Data Mining*. Elsevier Insights (**2014**).
- [81] S. Lloyd, M. Mohseni, and P. Rebentrost, *Quantum principal component analysis*. Nature Physics **10**, pages 631-633 (**2014**).
- [82] M. Schuld, R. Sweke, and J. J. Meyer, *Effect of data encoding on the expressive power of variational quantum-machine-learning models*. Phys. Rev. A **103**, 032430 (**2021**).
- [83] J. Preskill, *Quantum Computing in the NISQ era and beyond*. Quantum **2**, 79 (**2018**).
- [84] M. Cerezo, A. Arrasmith, R. Babbush, S. C. Benjamin, S. Endo, K. Fujii, J. R. McClean, K. Mitarai, X. Yuan, L. Cincio, and P. J. Coles, *Variational Quantum Algorithms*. Eprint:arXiv:2012.09265v2 (**2021**).
- [85] K. Bharti, A. Cervera-Lierta, T. H. Kyaw, T. Haug, S. Alperin-Lea, A. Anand, M. Degroote, H. Heimonen, J. S. Kottmann, T. Menke, W.-K. Mok, S. Sim, L.-C. Kwек, A. Aspuru-Guzik, *Noisy intermediate-scale quantum (NISQ) algorithms*. Eprint: arXiv:2101.08448v2 (**2021**).
- [86] S. Lloyd, M. Schuld, A. Ijaz, J. Izaac, and N. Killoran, *Quantum embeddings for machine learning*. Eprint: arXiv:2001.03622v2 (**2020**).
- [87] T. Hubregtzen, D. Wierichs, E. Gil-Fuster, P.-J. H. S. Derks, P. K. Faehrmann, and J. J. Meyer, *Training Quantum Embedding Kernels on Near-Term Quantum Computers*. Eprint: arXiv:2105.02276v1 (**2021**).
- [88] M. Fanizza, M. Rosati, M. Skotiniotis, J. Calsamiglia, and V. Giovannetti, *Beyond the swap test: optimal estimation of quantum state overlap*. Phys. Rev. Lett. **124**, (**2020**).
- [89] H. Buhrman, R. Cleve, J. Watrous, and R. de Wolf, *Quantum fingerprinting*. Phys. Rev. Lett. **87**, 167902 (**2001**).
- [90] L. Cincio, Y. Subaşı, A. T. Sornborger, and P. J. Coles, *Learning the quantum algorithm for state overlap*, New Journal of Physics **20**, 113022 (**2018**).

- [91] H.-Y. Huang, R. Kueng, and J. Preskill, *Predicting many properties of a quantum system from very few measurements*. Nature Physics volume **16**, pages 1050-1057 (2020).
- [92] S. T. Flammia, and Y.-K. Liu, *Direct Fidelity Estimation from Few Pauli Measurements*. Phys. Rev. Lett. **106**, 10.1103 (2011).
- [93] V. Bergholm, J. Izaac, M. Schuld, C. Gogolin, C. Blank, K. McKiernan, and N. Killoran, *PennyLane: Automatic differentiation of hybrid quantum-classical computations*. Eprint arXiv:1811.04968 (2020).
- [94] M. Reagor et al., *Demonstration of universal parametric entangling gates on a multi-qubit lattice*. Science advances **4.2**, (2018).
- [95] R. S. Smith, M. J. Curtis, and W. J. Zeng, *A Practical Quantum Instruction Set Architecture*. Eprint: arXiv:1608.03355v2 (2016).
- [96] D. Allan, *Statistics of Atomic Frequency Standards*. Proceedings of the IEEE, Vol. **54**, N. 2, pages 221-230 (1966).
- [97] Stable32 Frequency Stability Analysis Program from the IEEE UFFC web site: <http://www.stable32.com/>
- [98] A.S. Eddington, *The Nature of the Physical World*. Cambridge at the University Press, first edition 1928, reprinted 1948.
- [99] T. Berlage, *A selective undo mechanism for graphical user interfaces based on command objects*. ACM Trans. Comput.-Hum. Interact. **1 (3)**, 269-294 (1994).
- [100] K. Jakubec, M. Polák, M. Nečaský and I. Holubová, *Undo/Redo Operations in Complex Environments*. Procedia Comput. Sci. **32**, 561-570 (2014).
- [101] O. Oreshkov, and N. Cerf, *Operational formulation of time reversal in quantum theory*. Nat. Phys. **11**, 853-858 (2015).
- [102] E. Cohen, S. Dolev, and M. Rosenblit, *All-optical design for inherently energy-conserving reversible gates and circuits*. Nat. Commun. **7**, 11424 (2016).
- [103] G. B. Lesovik, I. A. Sadovskyy, M. V. Suslov, A. V. Lebedev, and V. M. Vinokur, *Arrow of time and its reversal on the IBM quantum computer*. Sci. Rep. **9**, 4396 (2019).

- [104] M. Shapiro, and P. Brumer, *Quantum control of chemical reactions*. J. Chem. Soc. Faraday Trans. **93**, 1263 (1997).
- [105] R.J. Nelson, Y. Weinstein, D. Cory, and S. Lloyd, *Experimental Demonstration of Fully Coherent Quantum Feedback*. Phys. Rev. Lett. **85**, 3045 (2000).
- [106] S. Chu, *Cold atoms and quantum control*. Nature **416**, 206–210 (2002).
- [107] I. Walmsley, and H. Rabitz, *Quantum Physics Under Control*. Phys. Today **56**, 43 (2003).
- [108] D. A. Steck, K. Jacobs, H. Mabuchi, T. Bhattacharya, and S. Habib, *Quantum Feedback Control of Atomic Motion in an Optical Cavity*. Phys. Rev. Lett. **92**, 223004 (2004).
- [109] H. Mabuchi, and N. Khaneja, *Principles and applications of control in quantum systems*. Int. J. Robust Nonlinear Control **15**, 647-667 (2005).
- [110] D. D'Alessandro, *Introduction to Quantum Control and Dynamics*. Chapman & Hall/CRC, (2007).
- [111] H. Rabitz, *Focus on Quantum Control*. New J. Phys. **11**, 105030 (2009).
- [112] H. M. Wiseman, and G. J. Milburn, *Quantum Measurement and Control*. Cambridge University Press, (2010).
- [113] C. Brif, R. Chakrabarti, and H. Rabitz. *Control of quantum phenomena: past, present and future*. New Journal of Physics **12** (7), 075008 (2010).
- [114] C. Altafini, and F. Ticozzi, *Modeling and control of quantum systems: An introduction*. IEEE Transactions on Automatic Control **57** (8), 1898-1917 (2012).
- [115] S. Hoyer, F. Caruso, S. Montangero, M. Sarovar, T. Calarco, M. B. Plenio, and K. B. Whaley, *Realistic and verifiable coherent control of excitonic states in a light-harvesting complex*. New J. Phys. **16**, (2014).
- [116] C. P. Koch, *Controlling open quantum systems: tools, achievements, and limitations*. Journal of Physics: Condensed Matter **28**, 213001 (2016).
- [117] M. Rossi, D. Mason, J. Chen, Y. Tsaturyan, and A. Schliesser, *Measurement-based quantum control of mechanical motion*. Nature **563**, 53–58 (2018).
- [118] S. Gherardini, F. Campaioli, F. Caruso, and F.C. Binder, *Stabilizing Open Quantum Batteries by Sequential Measurements*. Phys. Rev. Research **2**, 013095 (2020).

- [119] D. Girolami, *How Difficult is it to Prepare a Quantum State?* Phys. Rev. Lett. **122**, 010505 (2019).
- [120] M. M. Müller, S. Gherardini, T. Calarco, S. Montangero, and F. Caruso, *Information Theoretical Limits for Quantum Optimal Control Solutions: Error Scaling of Noisy Channels*. Eprint arXiv:2006.16113 (2020).
- [121] S. Gherardini, M. M. Müller, S. Montangero, T. Calarco, and F. Caruso, *Information flow and error scaling for fully-quantum control*. Eprint arXiv:2012.06234 (2020).
- [122] T. Caneva, T. Calarco, and S. Montangero, *Chopped random-basis quantum optimization*. Phys. Rev. A **84**, 022326 (2011).
- [123] P. Doria, T. Calarco, and S. Montangero, *Optimal Control Technique for Many-Body Quantum Dynamics*. Phys. Rev. Lett. **106**, 190501 (2011).
- [124] T. Caneva, A. Silva, R. Fazio, S. Lloyd, T. Calarco, and S. Montangero, *Complexity of controlling quantum many-body dynamics*. Phys. Rev. A **89**, 042322 (2014).
- [125] N. Rach, M. M. Müller, T. Calarco, and S. Montangero, *Dressing the chopped-random-basis optimization: A bandwidth-limited access to the trap-free landscape*. Phys. Rev. A **92** (6), 062343 (2015).
- [126] M. M. Müller, R. S. Said, F. Jelezko, T. Calarco, and S. Montangero, *One decade of quantum optimal control in the chopped random basis*. Eprint arXiv:2104.07687 (2021).
- [127] S. Rosi, A. Bernard, N. Fabbri, L. Fallani, C. Fort, M. Inguscio, T. Calarco, and S. Montangero, *Fast closed-loop optimal control of ultracold atoms in an optical lattice*. Phys. Rev. A **88**, 021601 (2013).
- [128] S. van Frank, A. Negretti, T. Berrada, R. Bucker, S. Montangero, J.-F. Schaff, T. Schumm, T. Calarco, and J. Schmiedmayer, *Interferometry with non-classical motional states of a Bose-Einstein condensate*. Nat. Comm. **5**, 4009 (2014).
- [129] C. Lovecchio, F. Schäfer, S. Cherukattil, M. Ali Khan, I. Herrera, F. S. Cataliotti, T. Calarco, S. Montangero, and F. Caruso, *Optimal preparation of quantum states on an atom-chip device*. Phys. Rev. A **93**, 010304(R) (2016).
- [130] S. van Frank, M. Bonneau, J. Schmiedmayer, S. Hild, C. Gross, M. Cheneau, I. Bloch, T. Pichler, A. Negretti, T. Calarco, and S. Montangero, *Optimal control of complex atomic quantum systems*. Sci. Rep. **6**, 34187 (2016).

- [131] A. Omran, H. Levine, A. Keesling, G. Semeghini, T. T. Wang, S. Ebadi, H. Bernien, A. S. Zibrov, H. Pichler, S. Choi, J. Cui, M. Rossignolo, P. Rembold, S. Montangero, T. Calarco, M. Endres, M. Greiner, V. Vuletić, and M. D. Lukin, *Generation and manipulation of Schrödinger cat states in Rydberg atom arrays*. *Science* **365** (6453), 570-574 (2019).
- [132] P. A. M. Dirac, *The Principles of Quantum Mechanics*. Oxford University Press, (1958).
- [133] L. M. K. Vandersypen, and I. L. Chuang, *NMR techniques for quantum control and computation*. *Rev. Mod. Phys.* **76**, 1037 (2005).
- [134] B. Kraus, W. Tittel, N. Gisin, M. Nilsson, S. Kroll, and J. I. Cirac, *Quantum memory for nonstationary light fields based on controlled reversible inhomogeneous broadening*. *Phys. Rev. A* **73**, 020302 (2006).
- [135] G. Hetet, J. J. Longdell, A. L. Alexander, P. K. Lam, and M. J. Sellars, *Electro-Optic Quantum Memory for Light Using Two-Level Atoms*. *Phys. Rev. Lett.* **100**, 023601 (2008).
- [136] T. Meunier, S. Gleyzes, P. Maioli, A. Auffeves, G. Nogues, M. Brune, J. M. Raimond, and S. Haroche, *Rabi Oscillations Revival Induced by Time Reversal: A Test of Mesoscopic Quantum Coherence*. *Phys. Rev. Lett.* **94**, 010401 (2005).
- [137] P. Schindler, T. Monz, D. Nigg, J. T. Barreiro, E. A. Martinez, M. F. Brandl, M. Chwalla, M. Hennrich, and R. Blatt, *Undoing a Quantum Measurement*. *Phys. Rev. Lett.* **110**, 070403 (2013).
- [138] B. H. Bransden, and C. J. Joachain, *Physics of Atoms and Molecules*. Pearson Education, India, (2003).
- [139] H. Breuer, and F. Petruccione, *The Theory of Open Quantum Systems*. Oxford University Press, (2003).
- [140] S. Lloyd and S. Montangero, *Information Theoretical Analysis of Quantum Optimal Control*. *Phys. Rev. Lett.* **113**, 010502 (2014).
- [141] T. Rowan, *Functional Stability Analysis of Numerical Algorithms*. Ph.D. thesis, Texas Univ., Austin, (1990).
- [142] A. Uhlmann, *The “transition probability” in the state space of a $*$ -algebra*. *Reports on Mathematical Physics*, **9** (2), 273-279 (1976).

- [143] C. Lovecchio, S. Cherukattil, B. Cilenti, I. Herrera, F. S. Cataliotti, S. Montangero, T. Calarco, and F. Caruso, *Quantum state reconstruction on atom-chips*. *New J. Phys.* **17**, 093024 (2015).
- [144] M. C. Mackey, *Time's Arrow: The Origins of Thermodynamic Behavior*. Springer, (1992).
- [145] P. A. Camati, J. P. S. Peterson, T. B. Batalhão, K. Micadei, A. M. Souza, R. S. Sarthour, I. S. Oliveira, and R. M. Serra, *Experimental Rectification of Entropy Production by Maxwell's Demon in a Quantum System*. *Phys. Rev. Lett.* **117**, 240502 (2016).
- [146] G. Manzano, J. M. Horowitz, and J. M. R. Parrondo, *Quantum Fluctuation Theorems for Arbitrary Environments: Adiabatic and Nonadiabatic Entropy Production*. *Phys. Rev. X* **8**, 031037 (2018).
- [147] S. Gherardini, M. M. Müller, A. Trombettoni, S. Ruffo, and F. Caruso, *Reconstructing quantum entropy production to probe irreversibility and correlations*. *Quantum Sci. Technol.* **3**, 035013 (2018).
- [148] M. Brunelli, L. Fusco, R. Landig, W. Wiczorek, J. Hoelscher-Obermaier, G. Landi, F. L. Semião, A. Ferraro, N. Kiesel, T. Donner, G. De Chiara, and M. Paternostro, *Experimental determination of irreversible entropy production in out-of-equilibrium mesoscopic quantum systems*. *Phys. Rev. Lett.* **121**, 160604 (2018).
- [149] T. B. Batalhão, S. Gherardini, J. P. Santos, G. T. Landi, and M. Paternostro, *Characterizing irreversibility in open quantum systems*. Book chapter in *Thermodynamics in the Quantum Regime – Fundamental Aspects and New Directions*, pp. 395-410, edited by F. Binder, L. A. Correa, C. Gogolin, J. Anders, and G. Adesso, Springer, Berlin, (2018).
- [150] H. Kwon, and M. S. Kim, *Fluctuation Theorems for a Quantum Channel*. *Phys. Rev. X* **9**, 031029 (2019).
- [151] G. T. Landi, and M. Paternostro, *Irreversible entropy production: From classical to quantum*. *Rev. Mod. Phys.* **93**, 035008 (2021).
- [152] J. Vanicek, *Dephasing representation of quantum fidelity for general pure and mixed states*. *Phys. Rev. E* **73**, 046204 (2006).
- [153] A. Goussev, R. A. Jalabert, H. M. Pastawski, and D. Wisniacki, *Loschmidt Echo*. *Scholarpedia* **7** (8), 11687 (2012).

-
- [154] A. Goussev, R. A. Jalabert, H. M. Pastawski, and D. Wisniacki, *Loschmidt echo and time reversal in complex systems*. Philos. Trans. A Math. Phys. Eng. Sci. **374** (2069), 20150383 (2016).
- [155] F. Schäfer, I. Herrera, S. Cherukattil, C. Lovecchio, F. S. Cataliotti, F. Caruso, and A. Smerzi, *Experimental realization of quantum Zeno dynamics*. Nat. Commun. **5**, 4194 (2014).
- [156] S. Gherardini, S. Gupta, F. S. Cataliotti, A. Smerzi, F. Caruso, and S. Ruffo, *Stochastic quantum Zeno by large deviation theory*. New J. Phys. **18**, 013048 (2016).
- [157] M. M. Müller, S. Gherardini, and F. Caruso, *Quantum Zeno dynamics through stochastic protocols*. Ann. Phys. **529**, 1600206 (2017).